Investigating the thermally grown oxides and attributed
effects of scales on heat transfer and interfacial friction
between the ingot and die during the open-die forging process

by

Ali VEDAEI SABEGH

MANUSCRIPT-BASED THESIS PRESENTED TO ÉCOLE DE
TECHNOLOGIE SUPÉRIEURE IN PARTIAL FULFILLMENT FOR THE
DEGREE OF DOCTOR OF PHILOSOPHY
Ph.D.

MONTREAL, 24 JUNE 2021

ÉCOLE DE TECHNOLOGIE SUPÉRIEURE
UNIVERSITÉ DU QUÉBEC

BOARD OF EXAMINERS (THESIS PH.D.)

THIS THESIS HAS BEEN EVALUATED

BY THE FOLLOWING BOARD OF EXAMINERS

Mr. Mohammad Jahazi, Thesis Supervisor
Mechanical Engineering Department, École de technologie supérieure

Mr. Ambrish Chandra, President of the Board of Examiners
Electrical Engineering Department, École de technologie supérieure

Mr. Henri Champliaud, Member of the jury
Mechanical Engineering Department, École de technologie supériure

Mr. Ali Bonakdar, Member of the jury
Mechanical Engineering Department, École de technologie supériure

Mr. Daolun Chen, External Evaluator
Mechanical and Industrial Engineering Department, Ryerson University

THIS THESIS WAS PRENSENTED AND DEFENDED

IN THE PRESENCE OF A BOARD OF EXAMINERS AND PUBLIC

<DEFENCE DATE OF THE THESIS>

AT ÉCOLE DE TECHNOLOGIE SUPÉRIEURE

ACKNOWLEDGMENT

Investigation sur le grossissement thermique des oxydes attribués aux effets d'échelles sur le transfert thermique et la friction interfaciale entre le lingot et la matrice lors du procédé de forgeage à matrice ouverte

Ali VEDAEI SABEGH

RÉSUMÉ

Le formage de métaux est recommandé pour les techniques de déformation des matériaux ayant un rapport volume/surface élevé. Les méthodes classiques de déformation des métaux continuent d'exister malgré l'émergence de nouvelles techniques de déformation. Comme l'une des plus anciennes méthodes de formage de métaux, le forgeage à matrice ouverte est une méthode classique, couramment utilisée pour déformer les lingots de grande taille. Dans cette méthode, le lingot est déformé plastiquement entre deux plaques plates, où une étape de post-forgeage telle que l'usinage sera nécessaire par la suite. La déformation durant le forgeage à matrice ouverte peut être réalisée à froid, à chaud ou entre les deux. Lors de la déformation à chaud des aciers, la formation et la croissance d'oxydes activée thermiquement sont inévitables. La surface en acier interagira avec l'environnement gazeux pour former différentes couches d'oxyde. Les couches d'oxyde formées sont une cause de perte du matériau. L'oxyde peut se détacher et pénétrer le lingot sous des charges de déformation causant des fissures et des défaillances matérielles. Les couches d'oxyde formées ont une très faible conductivité, et donc se comportent comme des isolants. Donc, le transfert de chaleur du lingot est remarquablement affecté par la présence de couches d'oxyde. Les couches d'oxyde peuvent affecter la friction interfaciale entre les matrices et le lingot. Les matrices sont coûteuses à réparer ou à remplacer. Par conséquent, l'effet des couches d'oxyde sur la friction interfaciale s'avère critique et nécessite une investigation.

Le progrès qu'avait connu Finkl Steel Co. au cours des 70 dernières années, a positionné le groupe comme étant le plus important producteur de pièces forgées à matrice ouverte au Canada, avec des installations internes utilisées pour la fonderie, le forgeage, le traitement thermique, l'usinage et l'inspection. Finkl Steel Co. fabrique les pièces forgées à matrice ouvertes pour combler les besoins des industries opérantes des domaines des moules d'injection de plastique, de l'automobile, de l'aérospatiale, du pétrole et du gaz, de la construction et de l'exploitation minière. Cependant, l'entreprise perd plus de cent kilogrammes de matériaux sous forme de déchets pour chaque lingot à cause de l'oxydation thermique. Le gradient de température au sein du lingot, est affecté par l'échelle des couches d'oxydes, ce qui impacte négativement par la suite les caractéristiques matériaux désirés. En outre, la friction interfaciale entre la matrice et le lingot est influencée par la présence d'oxyde. Les couts supplémentaires dus aux charges de déformation sont considérablement cruciaux pour l'entreprise, ainsi que ceux dus à la réparation des matrices en raison de l'usure. Cette étude a été définie dans ce contexte dans le but d'évaluer expérimentalement et numériquement l'oxydation thermique et ses effets sur le transfert de chaleur et la friction interfaciale des

lingots de grande taille. Cette étude est basée sur trois publications, qui peuvent être représentées comme suit:

Pour le premier article, l'oxydation thermique pour deux aciers à haute résistance a été étudiée. La composition chimique des deux aciers était la même, mise à part la concentration du Ni, qui était différente de presque six fois (2,92 %), afin d'étudier l'effet du Ni sur l'oxydation. Les quatre températures d'oxydation 1000, 1100, 1150, 1200 °C pour différents temps d'oxydation de 3,10, 20, 30 et 60 min ont été attribués pour évaluer l'effet du temps et de la température d'oxydation. Tant que le poids de l'échantillon augmente durant la formation des couches d'oxyde, la variation du poids peut indiquer le taux d'oxydation de l'acier. Ainsi, l'analyse thermique différentielle équipée de la thermogravimétrie (TG) a été employée. Les échantillons ont été chauffés aux températures d'oxydation désirées sous une atmosphère d'argon, où une unité fait la permutation de l'argon en l'air à cette température. L'échantillon est exposé à l'air durant le temps d'oxydation désiré. Les résultats pour les deux aciers ont démontré qu'en augmentant la température d'oxydation et le temps d'oxydation, le taux d'oxydation augmente. Toutefois, le changement du poids des deux aciers ont montré que l'acier ayant la plus grande teneur de Ni à un taux d'oxydation thermique plus faible que l'acier avec une faible teneur de Ni. L'énergie d'activation obtenue pour l'acier avec une teneur de Ni plus élevé est de 275 KJ mol^{-1} en comparaison à 238 KJ mol^{-1} pour l'acier avec une faible teneur en acier, ce qui démontre que l'ajout du Ni augmente la résistance à l'oxydation. Afin d'étudier le mécanisme sous-jacent du Ni résultant à réduire le taux d'oxydation, des analyses de diffraction des rayons X (DRX) ont été effectuées pour étudier les différentes couches d'oxydes. En plus de trois générales couches formées de wustite, magnétite et hématite, deux couches de spinelle ($FeOCr_2O_3$) et de chromite (Cr_2O_3) sont présentes. La spectroscopie par rayons X à dispersion d'énergie (SDE) a révélé une concentration du Ni sur le côté supérieur des couches d'oxyde. Aussi, une couche riche en Cr est présente à l'interface du métal-oxyde. Cette couche riche en Cr est plus épaisse pour l'acier avec la teneur de Ni la plus élevée. Toutes ces couches ont agi comme des obstacles contre la diffusion de l'oxygène dans le Fer, en supprimant ainsi l'accessibilité mutuelle des cations et des anions les uns aux autres et en diminuant par conséquent le taux de l'oxydation à des températures élevées. Par la suite, les pertes matériaux ont été réduites par l'ajout du Ni.

Dans la deuxième étude, l'évaluation de l'effet de la croissance de la couche d'oxyde sur le refroidissement des lingots de grande taille a été investigué. Les échantillons ont été chauffés à la température d'oxydation sous atmosphère d'argon, puis exposés à l'air pendant une période déterminée à l'aide d'un four a radiation. Un microscope confocal laser a été utilisé pour mesurer l'épaisseur d'oxyde formée, révélant ainsi un comportement de croissance parabolique de la couche d'oxide pour les deux aciers. Les couches d'oxyde formées pour l'acier avec une teneur élevée de Ni présentent une couche plus mince que celui avec une faible teneur en Ni. Il a été révélé aussi que la fraction d'épaisseur de la couche de wustite croit aussi avec l'élévation de la température d'oxydation, au détriment de celle de l'hématite. Toutefois, la fraction d'épaisseur de la magnétite demeure inchangée pour toutes les conditions d'essai. En plus, la fraction d'épaisseur relative aux couches est la même pour les couches d'oxyde formées sur les deux aciers. En d'autres termes, bien que les couches d'oxyde formées sont plus minces pour l'acier avec une teneur de Ni élevé, elles ont les mêmes fractions que celui

avec une faible teneur en Ni. Pour la simulation de refroidissement du lingot, les propriétés thermo-physiques des aciers ont été acquises à la fois par la méthode flash laser et le logiciel JMatPro. Les taux de refroidissement, et les valeurs de h, ont été obtenus par les équations de Holman pour être intégrés aux simulations basées sur la méthode des éléments finis. Les résultats issus du modèle éléments finis ont démontré que modèle numérique de simulation du lingot qui considère une couche d'oxyde a tendance à se refroidir plus rapidement depuis une température plus élevée que celui qui l'élimine, malgré le fait que les couches d'oxydes se comportent comme des matériaux isolants. Et ceci est dû au coefficient de rayonnement, qui est plus élevé pour la couche d'oxyde en comparaison avec la surface d'acier, facilitant ainsi l'extraction de la chaleur à travers les grandes surfaces de lingots. Cependant, dans le cas industriel, le lingot des fois peut demeurer dans le four pour plusieurs heures supplémentaires, induisant ainsi des couches d'oxyde. Dans un cas industriel, une couche d'oxyde de 7,8 millimètres a été observée. Cette couche d'oxyde a été utilisée pour la simulation du modèle éléments finis, et il a été constaté que le modèle du lingot intégrant cette couche d'oxyde a expérimenté température plus élevée de 200 K que celui sans couche d'oxyde. Ainsi, l'effet d'isolation de la couche d'oxyde est ressenti qu'après une certaine épaisseur soit atteinte, et donc avant cette épaisseur critique, la perte de chaleur est plus élevée. De plus, durant le contact avec les matrices, la couche d'oxyde la plus épaisse a empêché l'élévation de température pour les matrices jusqu'à 194 K. Les modèles d'éléments finis développés ont été vérifiés par des mesures expérimentales de la température de surface du lingot en utilisant une caméra thermique.

Dans l'article final, l'effet de la croissance d'oxydes activé thermiquement sur la friction interfaciale entre le lingot et la matrice a été évaluée. L'essai d'anneau est une méthode généralement employée pour évaluer la friction interfaciale. Avant de passer à l'essai d'anneau, des essais d'indentation ont été effectués pour étudier les propriétés mécaniques des couches d'oxyde formées sur différents aciers puis être intégrés à la simulation de l'essai d'anneau en se basant sur la méthode éléments finis. Un outil d'indentation pénètre la surface d'oxyde jusqu'à attendre le chargement prédéterminé, cette étape est suivie d'un maintien pendant un certain temps (temps de maintien), puis un déchargement. Les résultats de l'indentation ont montré que la dureté et le module de Young des couches d'oxyde sont élevés pour l'acier qui a une concentration plus élevée de Ni en comparaison à celui avec une teneur faible de Ni. Les courbes utilisées pour l'étalonnage de la friction ont été obtenues par la simulation des modèles éléments finis. Les anneaux ont été déformés à des températures élevées de 1273, 1373, 1423 et 1473 K entre deux plaques plates. La variation du diamètre interne a été enregistrée par rapport à la variation de la hauteur selon les différents coefficients de frottement utilisés. Les simulations développées ont été vérifiées par des essais d'anneau réalisés expérimentalement. Concernant les essais sur anneaux, des anneaux avec les dimensions géométriques suivantes: 18:9:6 mm ont été usinés à partir de blocs industriels. Ces anneaux ont été oxydés dans un four à radiation pendant un temps déterminé, puis déformés plastiquement. Les résultats ont montré que la couche d'oxyde peut agir comme un lubrifiant supplémentaire à des températures élevées.

XII

Investigating the thermally grown oxides and attributed effects of scales on heat transfer and interfacial friction between the ingot and die during the open-die forging process

Ali VEDAEI SABEGH

ABSTRACT

Bulk metal forming is indicated for the deformation techniques for materials with a high volume to surface ratio. The classic bulk metal deformation methods continue to survive despite the emergence of novel deformation techniques. As one of the oldest bulk metal forming methods, open-die forging is a classic method, commonly employed to deform large-size ingots. In this method, the ingot is plastically deformed between two flat platens, where a post-forging step like machining will be needed afterward. Open-die forging can be realized as cold, warm, and hot deformation. During the hot deformation of steels, it is inevitable to experience the forming of thermally grown oxides. The steel surface will react with the interactive gaseous environment to form different oxide layers. The formed oxide layers are a cause of material waste. The scale can detach and penetrate ingot by deformation loads causing cracks and failures. The formed oxide layers have very low conductivity, which makes them act as insulators. Thus, the heat transfer of ingot is remarkably affected by the presence of oxide layers. Oxide layers can affect the interfacial friction between anvils and ingot. The anvils are costly to repair or replace. Hence, the effect of oxide layers on interfacial friction is critical to be investigated.

Grown over the past 70 years, Finkl Steel Co. is the largest producer of open-die forgings in Canada, with in-house melting, forging, heat treating, machining, testing, and inspection facilities. Finkl Steel Co. employs open-die forging to serve the industries of plastic injection molds, automotive, aerospace, oil and gas, construction, and mining. However, the company has experienced over hundred kilograms of material waste for each ingot due to thermal oxidation. The ingot temperature gradient, which is affected by scale layers, has caused undesired material characteristics. Furthermore, the interfacial friction between die and ingot is influenced by the presence of oxide. The deformation loads are significantly crucial for the company, and the anvils are costly to be repaired due to wear. This study was defined in this context and had aimed to experimentally and numerically assess the thermal oxidation and its effects on heat transfer and interfacial friction of large-size ingots. This study has resulted in three publications, which can be explained as follows:

In the first article, the thermal oxidation of two high-strength steels was investigated. The chemical composition of both steels was the same, except Ni's concentration, which was almost six times (2.92 wt%), to investigate Ni's effect on oxidation. Four oxidation temperatures of 1000, 1100, 1150, 1200 °C, and oxidation times of 3,10, 20, 30, and 60 min were allocated to evaluate the effect of oxidation time and temperature. Since the sample's weight increases during the formation of oxide layers, the weight variation can indicate the steel's oxidation rate. So, differential thermal analysis equipped with thermogravimetry (TG) was employed. The samples were heated to the desired oxidation temperature under argon flow, where a unit

switches the argon to air at that temperature. The sample is exposed to air for desired oxidation time. The outcomes for both steels demonstrated that by increasing the oxidation temperature and oxidation time, the oxidation increased. However, two steels' weight changes showed that the steel with the higher amount of Ni had less thermal oxidation than steel with lower Ni. The obtained activation energy for steel with higher Ni was 275 KJ mol-1 compared to 238 KJ mol-1 for steel with lower Ni, which shows higher oxidation resistance by the addition of Ni. To investigate Ni's underlying mechanism for less oxidation, X-ray diffraction (XRD) analyses were conducted to investigate the different layers. In addition to three general layers of wustite, magnetite, and hematite, two layers of spinel ($FeOCr_2O_3$) and chromite (Cr_2O_3) were present. Energy-dispersive X-ray spectroscopy (EDS) showed the concentration of Ni on the top side of oxide layers. Also, there was a Cr rich layer at the interface of oxide-metal. This Cr rich layer was thicker for steel with higher Ni. All these layers acted as obstacles against diffusion of oxygen and Fe, suppressing the accessibility of cations and anions to each other and consequently decreasing oxidation at high temperatures. So, the material waste was less by the addition of Ni.

In the second study, the study aimed to assess the effect of oxide growth on large-size ingots' cooling. The samples were heated to oxidation temperature under argon gas and then exposed to air for a determined time employing a radiative furnace. A confocal laser microscope measured the formed oxide thickness, where a parabolic behavior was seen for both steels. The formed oxide layers on high Ni steel was thinner compared to low Ni steel. It was found out that the thickness fraction of the wustite layer increased by increasing the oxidation temperature, and that of the hematite decreased. However, the thickness fraction of magnetite stayed the same for all testing conditions. Also, the relative thickness fraction of layers was the same for formed oxide layers on both steels. In other words, although the formed oxide layers were thinner for high Ni steel, they had the same fractions of low Ni steel. For the ingot's cooling simulation, the steels' thermal properties were acquired by both the flash laser method and JMatPro software. The cooling rates, h-values, were obtained by Holman's equations for finite element simulations. The finite element results demonstrated that the ingot with an oxide layer tends to cool faster from higher temperature than the ingot without an oxide layer, despite the oxide layers' insulation effect. The is due to the higher radiation coefficient of the oxide layer compared to the steel surface, which facilitates heat loss through vast ingot surfaces. However, sometimes the ingot stays more than hours in the furnace in an industrial situation, leading to thicker oxide layers. For an industrial case, a 7.8 mm oxide layer was observed. This oxide layer was employed in finite element simulation, and it was found that the ingot with this oxide layer has 200 K more temperature compared to the ingot without oxide. So, the oxide layer's insulation effect comes after a certain thickness is attained, where before that thickness, it causes higher heat loss. Also, in contact with the anvils, the thicker oxide layer prevented a temperature rise of 194 K on anvils. The developed finite element models were verified by experimental measurement of ingot surface temperature by a thermal camera.

In the final article, the effect of thermally grown oxides on the interfacial friction between the ingot and die are evaluated. The ring test is a commonly employed method for assessing interfacial friction. Prior to the ring test, indentation tests were conducted to investigate the mechanical properties of formed oxide layers on different steels and use them for the ring test's

finite element simulation. An indentation tool is penetrated to the oxide surface up to a determined load and kept for a dwell time, and then unloaded. The indentation outcomes showed that the hardness and young modulus of formed oxide layers on steel with the higher concentration of Ni were lower than oxide formed on steel with lower Ni. Friction calibration curves were obtained by finite element simulations. The rings were deformed at high temperatures of 1273, 1373, 1423, and 1473 K between two flat platens. The variation of internal diameter was recorded concerning the variation of height for different friction coefficients. The developed simulations were verified by experimental ring tests. For ring tests, rings with geometrical dimensions of 18:9:6 mm were machined from blocks. These rings were oxidized in a radiative furnace for a determined time and then plastically deformed. The outcomes showed that the oxide layer can act as an additional lubricant at high temperatures.

TABLE OF CONTENTS

XVIII

LIST OF TABLES

LIST OF FIGURES

LIST OF ABREVIATIONS

TGO	Thermally grown oxides
TG	Thermogravimetry
TGA	Thermogravimetry analysis
Ni	Nickel
SEM	Scanning electron microscope
XRD	X-ray diffraction
O	Oxygen
Fe	Iron
C	Carbon
Al	Aluminum
Si	Silicon
Cr	Chromium
Ti	Titanium
LNi	Low Nickel
HNi	High Nickel
DTA	Differential thermal analysis
MTS	Material testing system
PID	Proportional–integral–derivative
EDS	Energy-dispersive X-ray spectroscopy
3D	Three dimensional
FE	Finite element

FEM	Finite element model
FEA	Finite element analysis
Cu	Copper
CAE	Computer-aided engineering

LIST OF SYMBOLS

$\Delta W/A$	Mass gain by unit surface (Linear rate kinetics)
$(\Delta W/A)^2$	Parabolic rate kinetics
k_p	Parabolic rate constant
k_l	Linear rate constant
t	Oxidation time
h	Oxide thickness
k	Parabolic growth rate
k_0	Parabolic oxidation kinetic constants
E_A	Activation energy
R	Gas constant
T	Absolute temperature
D	Diffusion coefficient
R_a	Rayleigh number
G_r	Grashof number
P_r	Prandtl number
g	Gravity acceleration
B	Thermal expansion coefficient
T_s	Surface temperature
T_∞	Quiescent temperature
T_f	Film temperature
Nus	Nusselt number

XXX

$\bar{h}$ Convective heat transfer coefficient

L Critical length

k Thermal conductivity of the fluid

INTRODUCTION

Traditional bulk metal forming methods continue to be employed, despite the emergence of novel technological methods (Dixit & Dixit, 2008). Open-die forging is a commonly utilized classic method for deforming large-sized ingots with a high volume to surface ratio. In this method, the ingot is plastically deformed between two flat platens under compressive stresses. The deformation can be realized as cold, warm, or hot deformation (Beddoes & Bibby, 1999; Dixit & Dixit, 2008).

In hot open-die forging, the ingot will inevitably experience the thermally grown oxide. The iron will interact with the ambiance oxygen to formed different oxide layers (Krzyzanowski, Beynon, & Farrugia, 2010). The formed oxide layers cause material waste. The formed oxide layers can also detach and indent into the ingot matrix, causing cracking and failure, sometimes scraping an ingot (Barrau, Boher, Gras, & Rezai-Aria, 2003). The oxide layers can be affected by various parameters like the oxidation temperature, oxidation time, and steel composition. The alloying elements can remarkably influence the oxidation kinetics and scale morphology (Munther & Lenard, 1999).

The large-sized ingot being deformed by open-die forging are losing the internal heat by conduction to anvils, convection, and radiation to ambient air. The oxide layer can significantly affect all the indicated heat transfer ways (Dong, He, Sun, Liu, & Hong, 2017; Jang, Lee, Kim, & Kim, 2010). Regarding the radiation to ambiance air by the vast surface area of ingots, the radiation can be different by oxide layers as the radiation coefficient is higher for the scale layer. Also, former studies have shown that the oxide layers have very low conductivity, making them act as insulators. Thus, the convection can be influenced by thermally grown oxides. The heat can be lost by conduction to anvils. However, the scale can affect the heat transfer as an intervening layer between ingot and anvils. The frictional condition is also affected by scale layers. It was found that the oxide layers can decrease friction at high temperatures (Matsumoto, Osumi, & Utsunomiya, 2014). However, scale layers can cause wear on anvils, costly to repair or replace (Barrau et al., 2003). The morphology and structure

of oxide layers can be different at different oxidation conditions. So, the friction can be different for different oxide layers.

Finkl Steel Co. is a Canadian company that employs open-die forging as a deformation method at high temperatures. The indicated points are observed and experienced during the production process. This study is defined in partnership with Fink Steel Co. to investigate both experimentally and numerically the thermally grown oxides and the attributed effects during the open-die forging process. The study is divided into three main sections. The outcomes of each section are presented as a paper and shown in the frame of a chapter.

This thesis is structured in four chapters. In the first chapter, the forging process, thermally grown oxides, and scales' effects are introduced. The challenges of the study are defined, and the objectives and literature review are given. In the second chapter, the kinetics of oxide growth is assessed for two high-strength steels. The effect of Nickel as an alloying element is investigated on thermally grown oxides. In the third chapter, the effect of thermally grown oxides on the cooling of large-size ingots is evaluated by numerical methods and verified by experimental tests. In the final chapter, the oxide layer mechanical properties are investigated by indentation tests. The outcomes are employed to evaluate the effect of oxide layers on the ingot's interfacial friction and die.

CHAPTER 1

LITERATURE REVIEW

1.1   Bulk metal forming

Metal forming processes are categorized into two different classes of bulk metal forming and sheet metal forming. Bulk metal forming processes are the forming methods on materials with a high volume to surface ratio, semi-finished initial workpiece, and a large amount of deformation. Bulk metal forming consists of classical and modified methods. Despite the emerging novel technologies (such as micro forming, nano forming, near net shape forming), the classical methods continue to be highly employed (Beddoes & Bibby, 1999; Dixit & Dixit, 2008). Hence, it is essential to develop an in-depth knowledge of classical methods, fundamentals, and the newly applied modifications to these processes. Also, the investigation of material behavior during forming processes is crucial. The highly utilized bulk metal forming processes are forging, extrusion, and rolling (Beddoes & Bibby, 1999).

In contrast to the sheet metal forming category, where the material is subjected to tensile stresses, the materials are compressed in bulk metal forming processes. So, the defects encountered in sheet metal forming, such as anisotropy or fracture, are generally avoided by tensile stresses. Considering the need to increase formability for the hard-to-deform metals, the deformation temperature increased too. Hence, a classification based on the deformation temperature can be introduced for bulk metal forming. In this regard, the hot, warm, and cold metal forming are introduced according to the melting temperature of the material, T_M. If the deformation is conducted at $<0.3\ T_M$, the deformation is cold metal forming, which will cause work hardening on the material. In case that the deformation is realized between $0.3\ T_M$ and $0.5\ T_M$, the deformation is classified as warm metal forming, with partial strain hardening. The hot metal forming is for deformation between $0.7 T_M$ and $0.8 T_M$, which causes almost no work hardening, but instead dynamic recovery or recrystallization (Beddoes & Bibby, 1999; Dixit & Dixit, 2008).

1.2   Forging

Probably forging is one of the oldest metal forming methods. It is defined as the plastic deformation of metal by pressing or hammering the material between two flat or countered platens. This process can be realized as cold, warm, or hot. Forging is mainly categorized as closed-die forging and open-die forging (Altan, Ngaile, & Shen, 2005; Dixit & Dixit, 2008).

1.2.1   Closed die forging

It is a process in which the metal has a restriction against the lateral flow. The metal is being deformed between two die halves, which carry the impression of the final shape. For this reason, impression forging is another name for this method. In this process, the hammering or pressing causes the material to fill the die cavity. The dies are not entirely closed, letting the excess material squeeze out and make the flash. The flash is designed to control the back-pressure of material flow and provide an appropriate cavity filling. However, the design of a precise gap for flash is critical, as it causes significant material waste (up to 20% of forged parts). The flash can be cleaned by a trimming die or even manually. Figure1.1 shows the closed die forging process before and after deformation (Altan et al., 2005; Dixit & Dixit, 2008).
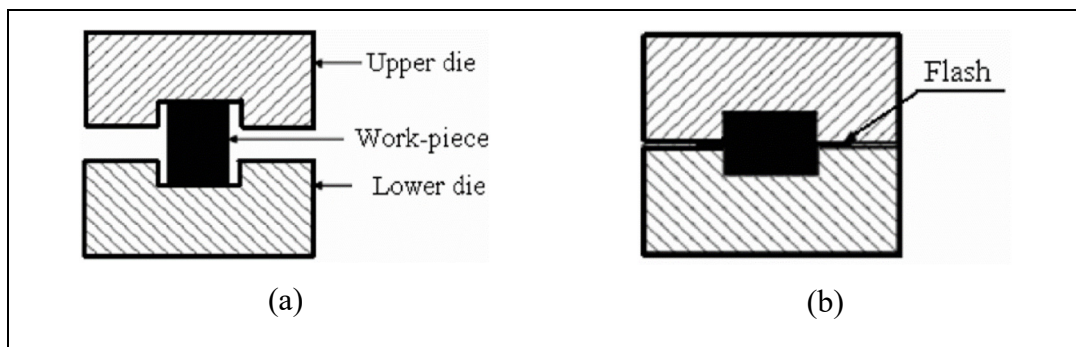
Figure 1.1 The closed-die forging process:
a) before deformation and b) after deformation
Taken from Dixit (2008, p. 4)

Considering the steps to produce a part by closed-die forming, the load-displacement curve of a typical workpiece can be recognized in three phases of (Beddoes & Bibby, 1999; Dixit & Dixit, 2008):

1) Upsetting: correlates to the lateral and vertical flow of material.
2) Cavity filling: the filling of the die cavity and making the flash.
3) End-stage: the cavity is filled, and the pressure inside of the die increases rapidly.

It should be noted that there is flash-less closed-die forging, in which the flash is not produced. However, the design and manufacturing of these dies are difficult and costly. Coining/hobbing and nosing are also two other types of closed-die forging method. Figure 1.2 illustrates the load-stroke behavior for the closed-die forging process (Nee, 2015).
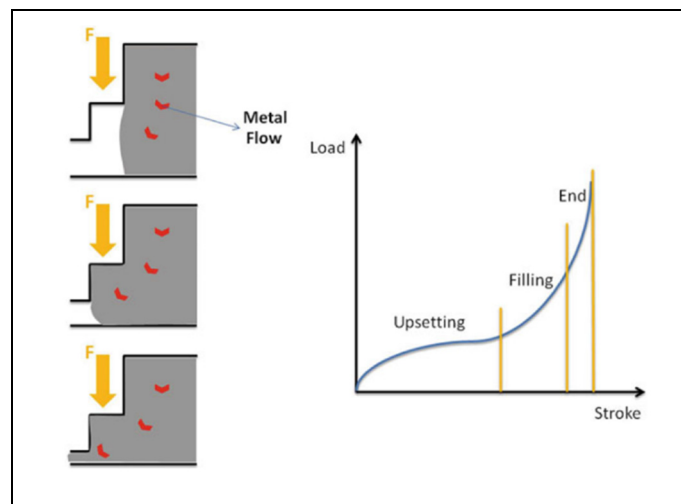
Figure 1.2 The load-stroke for different stages
of closed-die forging
Taken from Nee (2015, p. 182)

1.2.2 Open-die forging

This method is conducted on flat or simple shape dies. It is generally used as a final forming step, where a post-forging stage like machining is needed to attain the desired geometry. The material is placed on a stationary lower die, and the upper die movement deforms it. The

material does not have any lateral constraint to flow. A simple example of open-die forging is the upsetting of a cylinder, as shown in Figure 1.3.
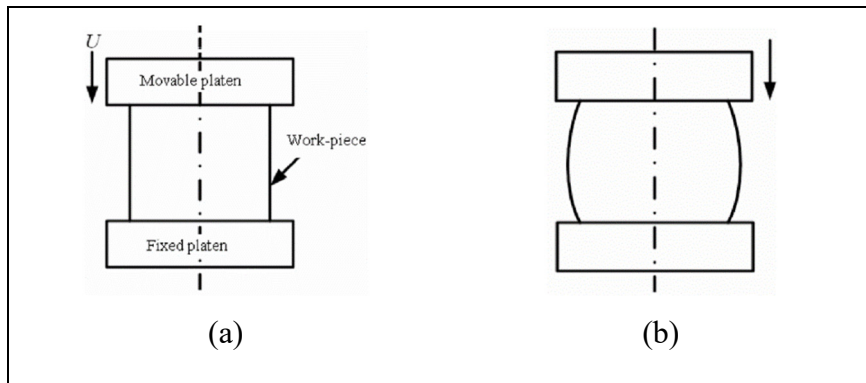
Figure 1.3 The closed-die forging process: a) before deformation
, and b) after deformation
Taken from Dixit (2008, p. 3)

Due to the friction between the material and anvils, the ingot experiences a constraint against the lateral flow at the interface, but the middle area flows freely. This issue can lead to the bulging/barreling effect, which is inhomogeneous deformation of the ingot. The amount of bulging can be an indirect indication of friction between material and anvils. Also, in case that the ratio of height-to-diameter of the ingot is greater than 2.5, lateral buckling can occur (see Figure 1.4) (Nee, 2015).

Figure 1.4 The deformation in the upsetting step of open-die forging:
a) barreling and b) buckling
Taken from Nee (2015, p. 181)

In case of high friction at the interface of anvils and ingot, the material at the end surfaces of the ingot will be restrained, known as the dead metal zone in microstructure, as shown in Figure 1.5 (Dixit & Dixit, 2008; Nee, 2015).
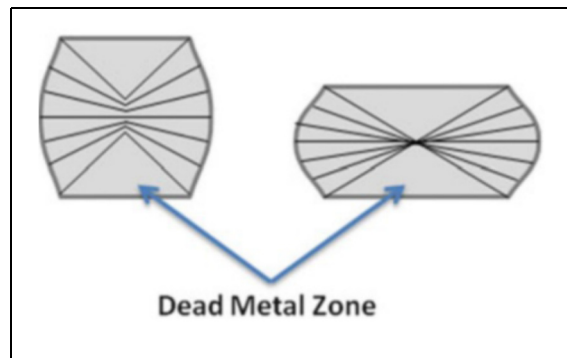
Figure 1.5 Dead metal zone near the anvils
for open-die forging
Taken from Nee (2015, p. 182)

Five steps are taken to accomplish the open die forging of a large size ingot with desired characteristics and geometry as follows:

1) Preform: this step is conducted to bring the initial ingot to a square cross-section, as shown in Figure 1.6).
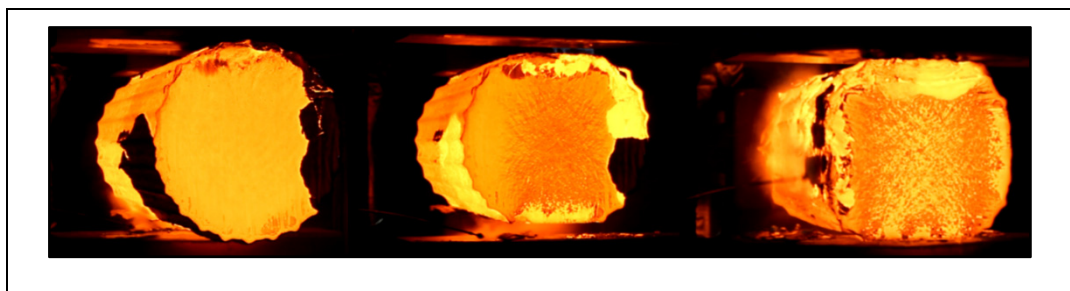
Figure 1.6 Preform of the ingot to make the square
cross-section from a cylindrical ingot

2) Upsetting: The ingot is deformed under compressive stress between two flat anvils to decrease height. As the volume of the material stays the same during deformation, the

ingot's width will increase. In this study, the upsetting decreases 0.9 m height of ingot with a deformation rate of 7.5 mm/s in 2 min (see Figure 1.7).
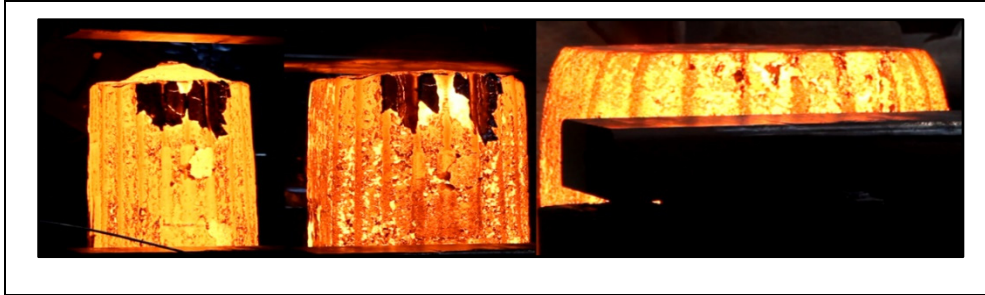
Figure 1.7 Decreasing the height and increasing
the ingot width in the upsetting stage

3) Free from Mannesmann effect (FM forging): In the metal forming process, forming a cavity along the longitudinal axis of a bar subjected to radial compression is known as the Mannesmann effect (Ghiotti, Fanini, Bruschi, & Bariani, 2009). The aim of the FM forging process is to prevent the generation of tensile stress in the core of the ingot. The conducted FM processes on the length and width are called FM-L and FM-C, respectively. As shown in Figure 1.8., this stage makes a deformation of 0.35 m with a deformation rate of 8.5 mm/s during the 37.5 seconds.

Figure 1.8 The FM phase in open die forging of large-sized ingots

4) Cogging: As given in Figure 1.9. flat or slightly curved anvils are employed to decrease the thickness of the ingot and increase its length. In fact, in cogging, the forging is

conducted on a large area compared to the size of anvils, where the part is being forged on a series of continuous deformations. In each step, the ingot is moved along its longitudinal direction for the next deformation by dies. The distance between each step of cogging that the ingot is moved, is known as the bite, about 45% to 75% of die width. More reductions can be realized by decreasing the bite length. The cogging step is for small deformations, which needs less deformation loads. As the ingot is cooled down from 1250 °C of the furnace to about 800 °C at this phase, a furnace reheat can be needed to avoid the deformation defects and failures. The ingot is compressed about 0.18 m in width, 0.28 in length, with a deformation rate of 24.5 mm/s for 30 min.
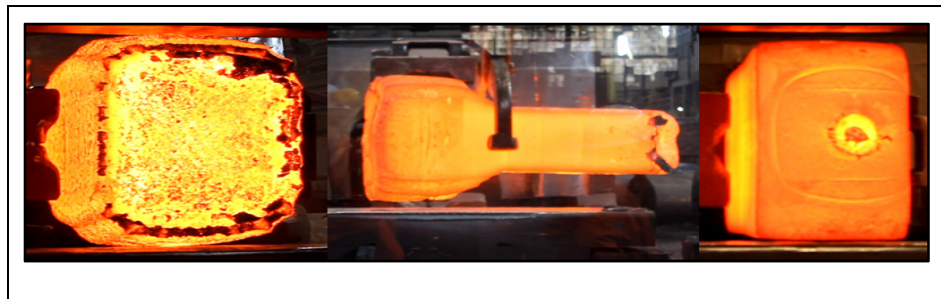
Figure 1.9 Deformation of the ingot in cogging step

5) Finishing: As shown in Figure 1.10, this step is similar to the cogging stage and brings the ingot to the desired shape. During this phase, the ingot can be compressed for 0.37 and 0.5 m in width and length, for 35 min, and with a deformation rate of 24.5 mm/s.

Figure 1.10 bringing the ingot to the desired geometry by finishing step

1.3   Iron-oxygen binary system

It is inevitable for most steels to endure thermal oxidation during heat treatment or forming operations at high temperatures (Krzyzanowski, Beynon, & Farrugia, 2010). At high temperatures (temperature above 700 °C), the Fe^{2+} and Fe^{3+} cations diffuse outwards, reaching the surface, where the oxygen anions O_2^- diffuse inward to create the oxide layers. The oxidation of iron in the air at high temperature produces different compounds depending on the oxidation temperature. Figure 1.11 shows the binary phase diagram of iron-oxygen. Below 570 °C, the scale consists of two layers of magnetite (Fe_3O_4) and hematite (Fe_2O_3), with magnetite close to the base metal. At a temperature above 570 °C, wustite (FeO) is formed as the first layer closest to the base metal, followed by magnetite and hematite (Birks, Meier, & Pettit, 2006; Talbot & Talbot, 2018).
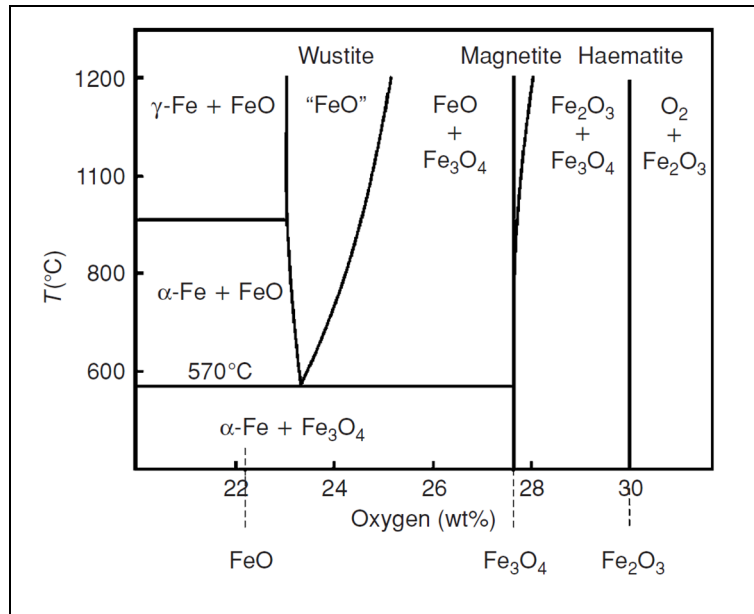
Figure 1.11 The iron-oxygen phase diagram
Taken from Birks et al. (2006, p. 83)

Wustite is a semiconductor phase with a wide range of stoichiometry from $Fe_{0.95}O$ to $Fe_{0.88}O$ at 1273 K (Birks et al., 2006). Magnetite is an inverse spinel. This phase comprises the divalent

ions, Fe^{2+}, taking place at octahedral sites. Also, half of the trivalent ions, Fe^{3+}, occupy the tetrahedral sites. Since the defects can occur on both sites, the diffusion can happen on both tetrahedral and octahedral sites. Except for the high temperatures, this phase exists for a slight range of stoichiometry. At the outermost of oxide, hematite exists. This layer can be seen in two forms of α-Fe_2O_3 and γ -Fe_2O_3, with rhombohedral and cubic structures, respectively. As the hematite is found to be oxidized as α-Fe_2O_3 at a temperature above 400 °C, only this structure is considered studies of thermally grown oxides at high temperatures. In this structure, oxygen exists in closed-pack hexagonal arrangements (Birks et al., 2006; Talbot & Talbot, 2018).

Considering the addressed oxide layers, the oxidation mechanisms can be given as shown in Figure 1.12. At the wustite interface with iron, the iron ionized and migrates through FeO by vacancies as Equation. 1.1. On the wustite interface with magnetite, magnetite is reduced by the electrons and the iron ions, as reported in Equation. 1.2 (Birks et al., 2006).

$$Fe = Fe^{2+} + 2e^- \tag{1.1}$$
$$Fe^{2+} + 2e^- + Fe_3O_4 = 4FeO \tag{1.2}$$

Magnetite is formed at the magnetite-hematite interface by passing the rest of iron ions through the existing magnetite, based on Equation. 1.3 (Birks et al., 2006).

$$Fe^{n+} + ne^- + 4Fe_2O_3 = 3Fe_3O_4 \tag{1.3}$$

The coefficient 'n' can be 2 or 3 for the Fe^2 and Fe^{3+}, respectively. The last layer of hematite is formed according to Equation. 1.4, at the interface of hematite with the gas (Birks et al., 2006).

$$2Fe^{3+} + 6e^- + \frac{3}{2}O_2 = Fe_2O_3 \tag{1.4}$$
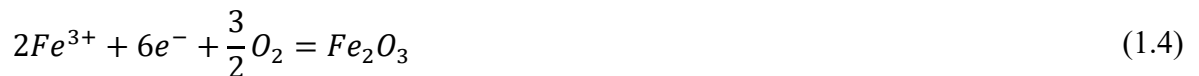
The summary of the stated reactions is shown in Figure 1.12.
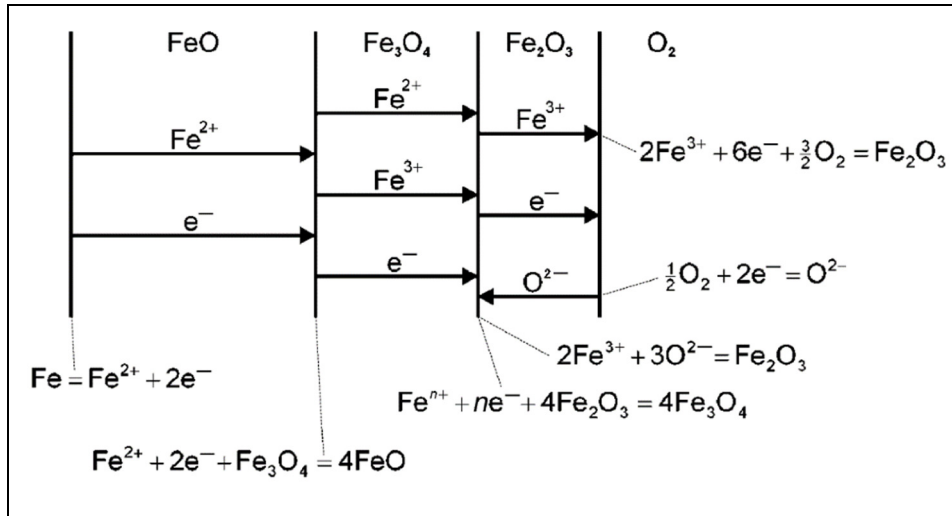
Figure 1.12 Formation of oxide layers at the
temperature above 570 °C
Taken from Birks et al. (2006, p. 84)

1.4   Decarburization (Fick's law)

The oxidation of carbon can be realized at the conditions causing iron oxidation. Decarburization of metal can be expressed as the oxidation at the surface of dissolved carbon in the metal lattice. It should be noted that iron and carbon are oxidized simultaneously during the heat treatment process. The oxidation of carbon forms gaseous products of CO and CO2. For an oxide layer, if these products can escape either due to porous oxide or by high equilibrium pressure of carbon oxides, considerable decarburization could take place. The consumed carbon due to decarburization must be replaced from inside by diffusion, which leads to the three steps for decarburization. First, the oxygen must be transported to the metal surface by surrounding gas. Then, the carbon will be exchanged at the interface of metal with gas. Finally, the carbon is diffused within the metal (Committee, 1991; Mehrer, 2007; Totten, 2006).

The rate of decarburization is governed by the diffusion of the carbon in metal. At a temperature below 910 °C, the steel surface is covered with a ferrite layer. The low solubility

of carbon in ferrite makes this layer a barrier for carbon diffusion. In contrast, above 910 °C, the decarburization is severe, as the material stays austenitic. Figure 1.13 illustrates the decarburization model of fully austenitic steel. It is assumed that the carbon content at the interface of metal with oxide is at the equilibrium with the oxygen potential of oxide at the interface of wustite with the base metal. As given in Figure 1.13, for utilizing this model, the distances are considered from the original surface of the metal to the instantaneous new oxide-metal interface at the time t and the distance of x=X. In other words, X thickness of base metal is consumed due to oxidation at time t. By solving the Fick's second law for certain boundary conditions, the distribution of carbon in metal and depth of decarburization can be acquired as follows (Birks et al., 2006; Committee, 1991; Totten, 2006):

$$\frac{\partial C}{\partial t} = D\frac{\partial^2 C}{\partial x^2} \ for \ x > X \tag{1.5}$$

$$C = C_0, x > 0; \ t = 0 \tag{1.6}$$

$$C = C_s, x = X; \ t > 0 \tag{1.7}$$

Equations 1.6 and 1.7 indicate the initial uniform concentration of carbon in the base metal and the constant carbon concentration at the interface of oxide-metal, respectively. The carbon concentration in metal for x>X and as a function of time can be obtained as follows (Mehrer, 2007; Totten, 2006):

$$\frac{C_0 - C}{C_0 - C_s} = \frac{erfc(\frac{x}{2\sqrt{Dt}})}{erfc(\frac{k_c}{2D})^{\frac{1}{2}}} \tag{1.8}$$

where C_0 is the initial concentration of carbon in the metal, C_s is the carbon concentration at the oxide-metal interface, D is the self-diffusion coefficient of carbon, t is the time, erfc is the error function, and the k_c is the corrosion constant of metal. The kc can be determined for specific steel in a certain atmosphere as follows (Totten, 2006):

14

$$k_c = 0.571 \exp\left(\frac{-43238}{RT}\right)\frac{cm^2}{s} \tag{1.9}$$

Since the variation of the diffusion coefficient of carbon in austenite was omitted in Equation. 1.5. So, the diffusion coefficient of zero-carbon should be utilized that can be acquired as follows (Totten, 2006):

$$D_{(C=0)} = 0.246 \exp\left(\frac{-34900}{RT}\right)\frac{cm^2}{s} \tag{1.10}$$

1.5 Effects of alloying elements on the oxidation

Thermally grown oxides are unavoidable for the majority of steels during the heat treatment or deformation processes. The oxide layers are formed at high temperatures by the interaction of steel with a reactive gaseous atmosphere (Birks et al., 2006). Along with the remarkable material waste due to oxidation, surface integrity and quality can be deteriorated by the creation of oxide layers. This issue can influence the workpiece's lifespan and forming tools (Utsunomiya, Doi, Hara, Sakai, & Yanagi, 2009). The characteristics of oxide layers are entirely different from base metal, causing a remarkable influence on the friction between die and ingot (Barrau, Boher, Gras, & Rezai-Aria, 2003). Also, the ingot's heat transfer condition is affected by the presence of oxide layers (Jang, Lee, Kim, & Kim, 2010).

During hot deformation, the oxide layers detach from the material and indent into an ingot by deformation loads, causing cracks or even scrapping the ingot. The separated oxide layers can also indent anvils, causing premature tool wear and decreasing the tool's service time (Barrau et al., 2003). The oxidation can be affected by slight changes in the material's initial composition or process parameters (Hu, Zhang, Chen, Fang, & Jiang, 2013; Yuan, Wang, Zhu, & Wang, 2013). So, it is crucial to provide a better understanding of the oxidation kinetics and underlying mechanism.

During the thermal oxidation of steel, the Fe cations (Fe^{2+} and Fe^{3+}) diffuse outward to establish the equilibrium at the metal-gas interface with oxygen. The diffusion of Fe cations and oxygen anions (O_2^-) are the affecting oxidation parameters (Suarez, Houbaert, Eynde, & Colás, 2009). Notwithstanding that the diffusion of Fe is faster in steel than the oxygen, the Fe diffusion is considered as the main affecting parameter on thermal oxidation of steels (Vijh, 1974; Wakasa & Yamaki, 1988). The oxidation starts with discrete nuclei at different sites. These sites grow laterally to reach and join each other. The oxidation progresses by mass diffusion of ions in the normal direction to the oxidation surface (Munther & Lenard, 1999). As oxidation is a diffusion phenomenon, time and temperature are two decisive factors for the oxidation of steels (H Abuluwefa, Guthrie, & Ajersch, 1996; Munther & Lenard, 1999).

The oxidation growth demonstrates a parabolic growth rate as follows (Birks et al., 2006; R. Chen & Yeun, 2003; Suárez, Houbaert, Eynde, & Colás, 2008):

$$h = \sqrt{k.t} \tag{1.11}$$

where h is the oxide thickness (cm), k is parabolic growth rate (cm^2s^{-1}), and t is time (s). At the initial steps of oxidation, the material surface is free from the diffusion barriers, and the oxidation proceeds fast. After some time, the formed oxide layers act as obstacles against diffusion as the Fe and O ions must pass through them, which slows down the oxidation process.

Concerning the Equation. 1.11, Xian-jun et al. (Hu et al., 2013) assessed the oxidation of high carbon steel. The results indicated the parabolic growth rate at the temperature above 1073 K. The results also showed a higher oxidation rate at a temperature higher than 1173 K, particularly in the initial 20 s (initial faster oxidation). Birosca et al. (Birosca, West, & Higginson, 2005) investigated low carbon steel oxidation in air at 923 to 1373 K. Figure 1.13 shows the outcomes, the parabolic growth of oxidation, which increases by increasing the oxidation temperature.
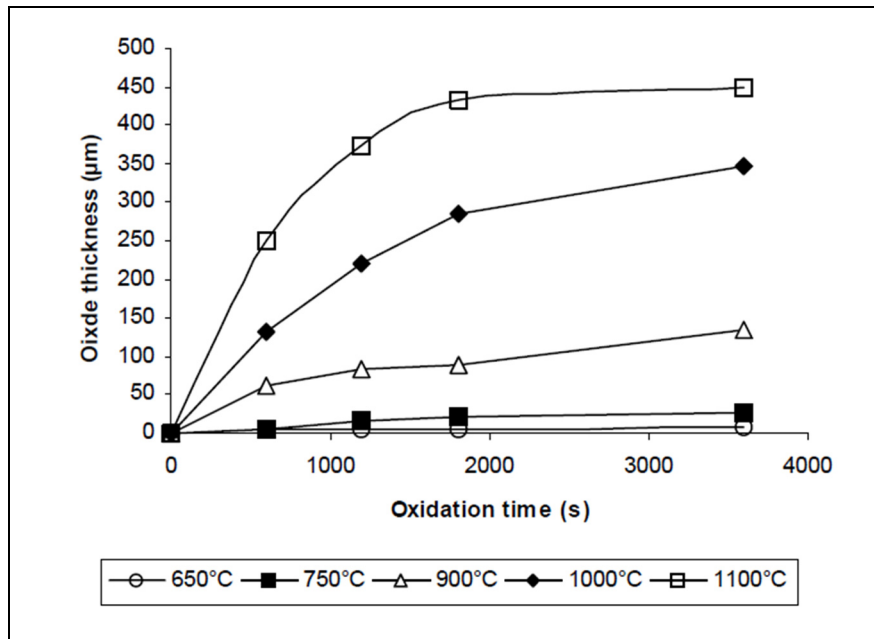
Figure 1.13 Oxidation of low carbon steel and the
parabolic growth kinetics (Birosca et al., 2005)
Taken from Birosca et al. (2005, p. 3)

A linear short time growth trend was observed in some studies, which shifted to parabolic growth after a short time. In this regard, Chen et al. (R. Y. Chen & Yuen, 2008) evaluated the short-time oxidation of low-carbon, low-silicon steel in the air at 1123 to 1453 K. As illustrated in Figure 1.14 the oxidation kinetics has a linear growth that is substituted for parabolic behavior after a short time.
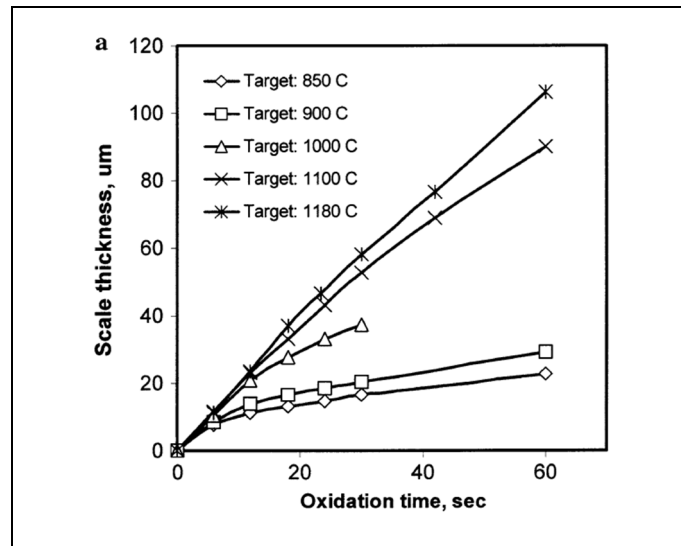
Figure 1.14 Oxidation behavior of low-carbon,
low-silicon steel
Taken from Chen and Yuen (2008, p. 45)

Cao et al. (Cao, Liu, Sun, & Liu, 2014) observed the same behavior for low carbon steel oxidation at a temperature range of 773 to1173 K. Regarding the oxidizing atmosphere; the reactive gases can significantly influence the oxidation behavior.
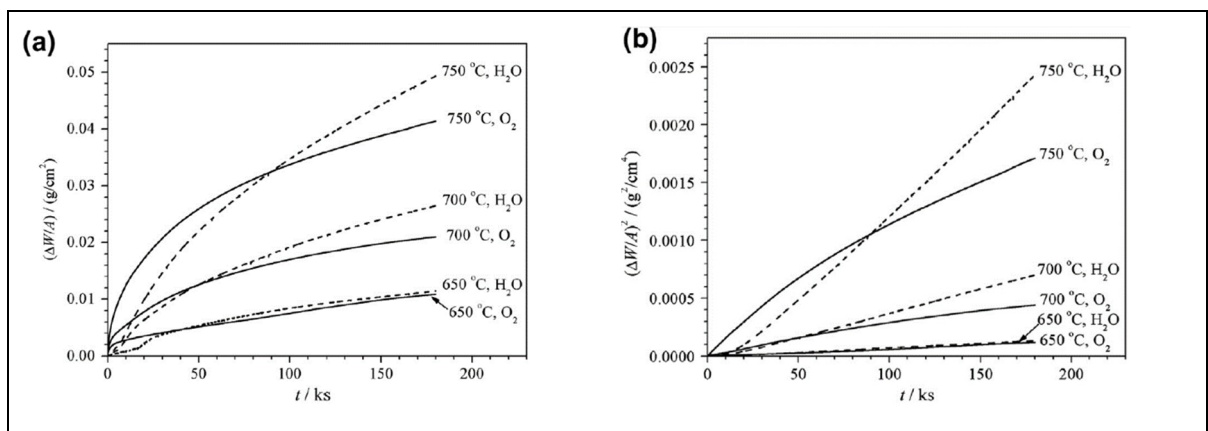
Figure 1.15 a) Oxidation kinetics of iron in oxygen and steam and
b) parabolic plot of oxidation behavior
Taken from Yuan et al. (2013, p. 310)

Chen and Yuen (R. Chen & Yeun, 2003) investigated the effect of different oxidation atmospheres of air and oxygen on pure iron's growth kinetics. The outcomes showed parabolic oxidation of iron at the temperature range of 973 to 1373 K. In contrast, Yuan et al. (Yuan, Wang, et al., 2013) obtained parabolic kinetics for the oxidation of iron in oxygen and linear-parabolic behavior in steam. Figure 1.15 gives iron oxidation outcomes in two atmospheres of oxygen and steam at 923 to 1023 K.

The SUS 430 steel demonstrates the parabolic growth rate when oxidized in humid air at the temperature range of 1273 to 1423, according to the study of Cheng et al. (Cheng et al., 2015). Along with the oxidizing atmosphere and temperature, the material's initial composition is another critical element that can remarkably affect the oxidation process. Higginson et al. (Higginson, Jepson, & West, 2006) compared the oxidation of low alloy steel with stainless steel. The results showed that stainless steel had a slower oxidation rate due to the formation of passive layers. These passive layers had crystallographic structures of corundum or spinel, which acted as barriers against diffusion. So, the alloying element can influence the oxidation. Carbon is one of the most affecting oxidation elements, showing both accelerating and decelerating effects (Kao & Wan, 1988; C. Wang & Duh, 1988). Fe-C oxidized faster than iron, based on the study of Boggs and Kachik (Boggs & Kachik, 1969) at 723 K. In contrast, Caplan et al. (Caplan, Sproule, Hussey, & Graham, 1979) reported that the oxidation rate of Fe-0.5 wt %C and Fe- 1.0 wt %C alloys was slower compared to iron at 973 K. Former studies indicated remarkable effects of alloying elements such as Si, Al, and Cr on the kinetics of oxidation. The effect of Si on the oxidation of low alloy steel was investigated by Mouayd et al. (Mouayd, Koltsov, Sutter, & Tribollet, 2014), where the Si showed to make resistance to oxidation below 1450 K. This resistance was not effective above the 1450 K, as illustrated in Figure 1.16.
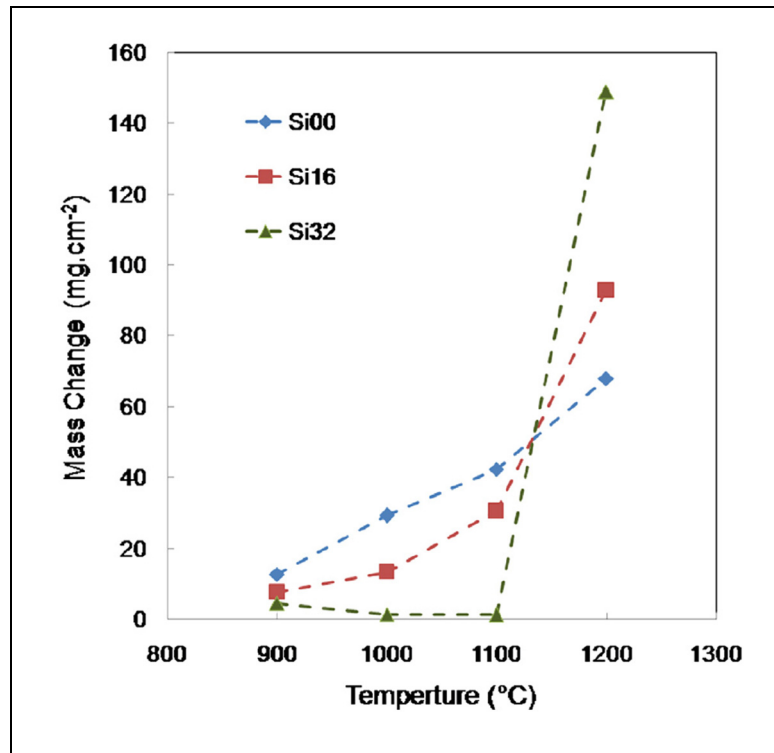
Figure 1.16 The effect of Si on oxidation of low alloy steel
Taken from Mouayd et al. (2014, p. 999)

According to Rahmel et al. (Rahmel, Schütze, & Quadakkers, 1995) and Kao and Wan's (Kao & Wan, 1988) studies, the addition of Al can decrease the oxidation rate by forming the α-Al2O3 layer, which acts as a diffusion barrier. The resistance to oxidation by the addition of Al as an alloying element was observed by Krzyzanowski and Beynon (Krzyzanowski & Beynon, 2006), and Von Fraunhofer and Pickup (Von Fraunhofer & Pickup, 1970) too, but contributed to the increase of wustite formation temperature. Takeda et al. (Takeda et al., 2010) investigated Cr and Si's effect on the thermally grown oxides. The outcomes showed that $FeOCr_2O_4$ and Fe_2SiO_4 layers were formed at the oxide's interface with metal, decreasing the oxidation rate. Figure 1.17 shows the formed spinel layer.
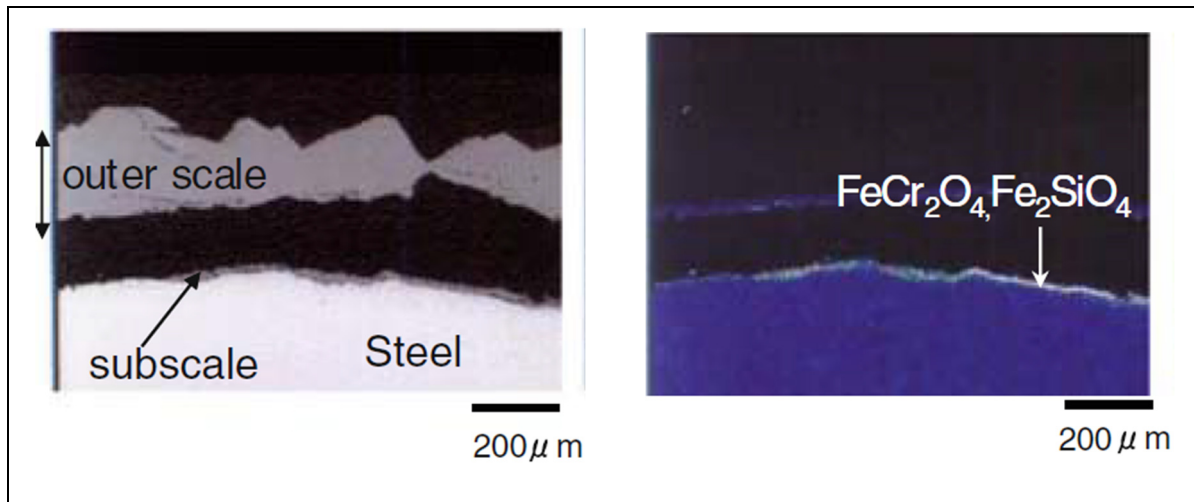
Figure 1.17 The formed spinel layers at the interface of oxide-metal by adding Cr and Si
Taken from Takeda et al. (2010, p. 8)

The comparison between the above studies regarding the effect of Cr, Si, and Al on the kinetics of oxidation reveals that at the temperature range of 773 to 973 K, Cr was less effective than the other two elements (I. Kim, Cho, & Kim, 2000; Krzyzanowski et al., 2010). The study of Yin et al. (L. Yin, Balaji, & Sridhar, 2010) showed that Ni decreased the oxidation rate of Fe-Cu-Ni alloys at the oxidation temperature of 1423 K. The resistance to thermal oxidation was explained by the lower activity of Fe liquid Cu-phase, which comes from the enrichment of Ni at the liquid-Cu/γFe interface. Regarding the effect of Ni on oxidation, Webler et al. (B. A. Webler & Sridhar, 2007) scrutinized the oxidation of iron by adding 0.3 Cu and 0.3 Cu + 0.1 Ni. As given in Figure 1.18, by increasing the Cu + Ni, the oxidation can decrease to half. The formation of a Cu-rich liquid layer at the wustite-metal interface was the diffusion barrier for this case (see Figure 1.18).
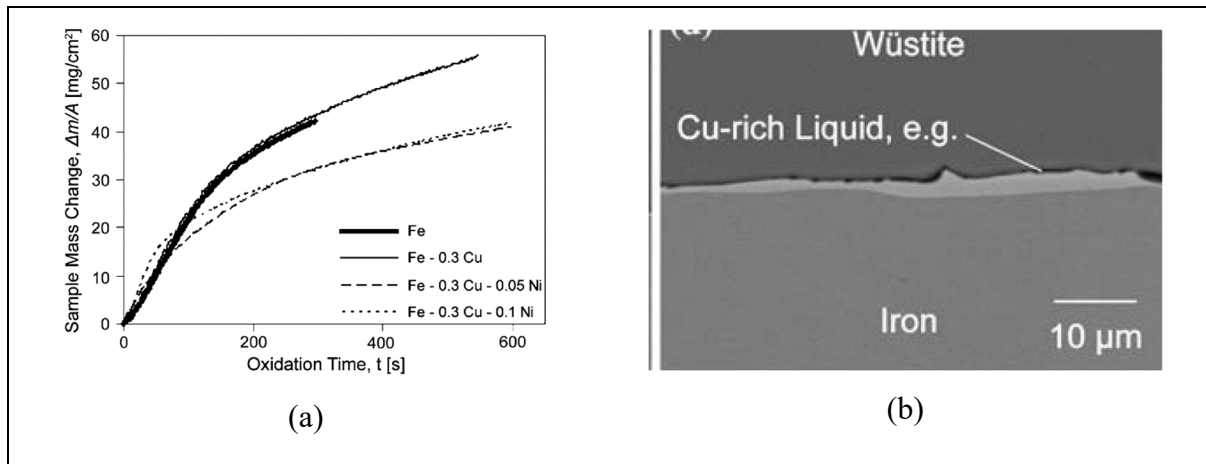
Figure 1.18 The effect of Ni on the oxidation kinetics of iron, and b) the Cu-rich
liquid layer at the wustite-iron interface
Taken from Webler and Sridhar (2008, p. 728)

Asai et al. (Asai, Soshiroda, & Miyahara, 1997) showed that Ni's addition will increase the length of the interface between the oxide and the metal, providing more bonding between them. Hence, the oxide removability will decrease. Figure 1.19 illustrates the length increase in the metal-oxide increase by the addition of Ni.

Figure 1.19 The effect of Ni on the length of
the metal-oxide interface
Taken from Asai et al. (1997, p. 276)

It should also be noted that the effects of alloying elements on the oxidation can change by temperature variation. In this regard, Chen and Yuen. (R. Chen & Yuen, 2005b) assessed copper-containing steels' oxidation at the 1253 to 1493 K by adding the Cu and Ni as alloying elements. The alloying elements had three different effects according to oxidation temperature. As illustrated in Figure 1.20, in 1253, the addition of Cu and Ni decreased the oxidation rate. In contrast, at 1393 K, the addition of Cu increased the oxidation rate. The alloying element demonstrated no remarkable effect on oxidation at 1493 K.
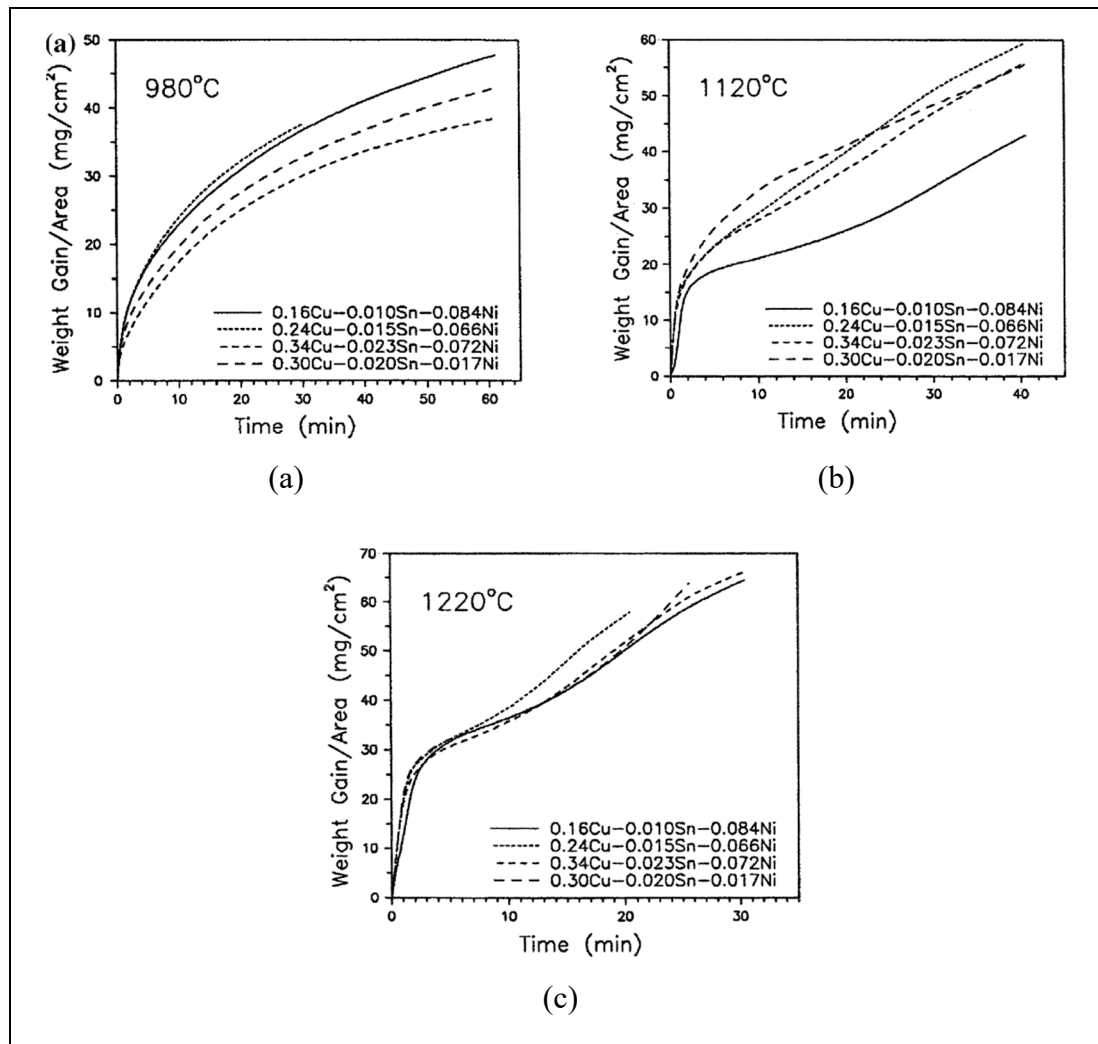
Figure 1.20 Effect of Cu and Ni on the oxidation of copper-containing steels
Taken from Chen and Yuen (2005, p. 149)

The oxidation of steel requires a certain amount of energy to be realized, known as activation energy. In chemistry, activation energy is the minimum required amount of energy given to atoms to activate them for a condition that they can go through a chemical reaction or physical transportation (Bhadeshia & Honeycombe, 2017; Pihtili, 2013). The activation energy is incorporated intimately with the kinetics of reactions. The activation energy of a reaction can be obtained by the Arrhenius equation as follows (Suarez et al., 2009; Young, 2008; Yuan, Wu, Wang, Zhu, & Wang, 2013):

$$k = A \exp(-\frac{E_a}{RT}) \qquad (1.12)$$

where R is the gas constant (8.314 J.mol^{-1}.K^{-1}), T is the temperature (K), A is the Arrhenius pre-exponential factor (g^2.cm^{-4}.s^{-1}), and E$_a$ is the activation energy (J.mol^{-1}). The logarithmic form of Equation. 1.12 is as follows (Pihtili, 2013):

$$\ln k = \ln A - \frac{E_a}{RT} \qquad (1.13)$$

The given Equation. 1.13 can be treated as the equation of a straight line (y=mx+c). Hence, the plot of ln (k) against $\frac{1}{RT}$ will be a straight line, with the gradient of E$_a$. So, the slope of the line equals the activation energy.

The activation energy of a reaction can also be affected by different alloying elements, oxidation temperature, and oxidation time. Young (Young, 2008) evaluated Co's oxidation in the air at the temperature range of 1073 to 1223 K and 1223 to 1423 K. The corresponding activation energies were 230 and 120 KJ.mol^{-1}, respectively. The same study reported the activation energy of 243 KJ.mol^{-1} for the oxidation of Cr at 1253 to 1473 K. Munther and Lenard (Munther & Lenard, 1999) determined 120 KJ.mol^{-1} for the activation energy of wustite in the oxidation of AISI 1018 steel at the temperature range of 1173 to 1473 K, as illustrated in Figure 1.21. Concerning Cr and Si's effect, Jha et al. (Jha, Haworth, & Argent, 2001) investigated the oxidation of Fe-19.2% Cr and Fe-4% Si at a temperature range of 1073

to 1273 K, where 178 and 201 KJ.mol^{-1} acquired for the activation energy of steels, respectively.
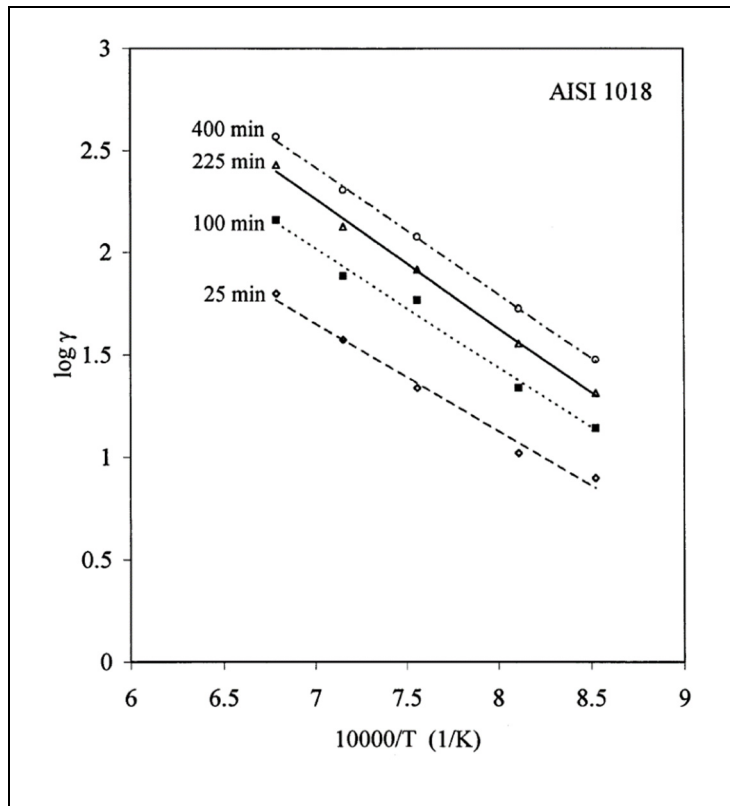
Figure 1.21 Calculation of activation energy for wustite
in the oxidation of AISI 1018 steel at the temperature
range of 1173 to 1473 K
Taken from Munther and Lenard (1999, p. 108)

Liu et al. (Liu, Tang, Wu, & Wang, 2013) obtained two activation energies for the oxidation of micro-alloyed steel, depending on the temperature. For oxidation below 1273 K, the activation energy was 339 806 J.mol^{-1}, which decreased to 105 633 J.mol^{-1} higher than this temperature (see Figure 1.22).
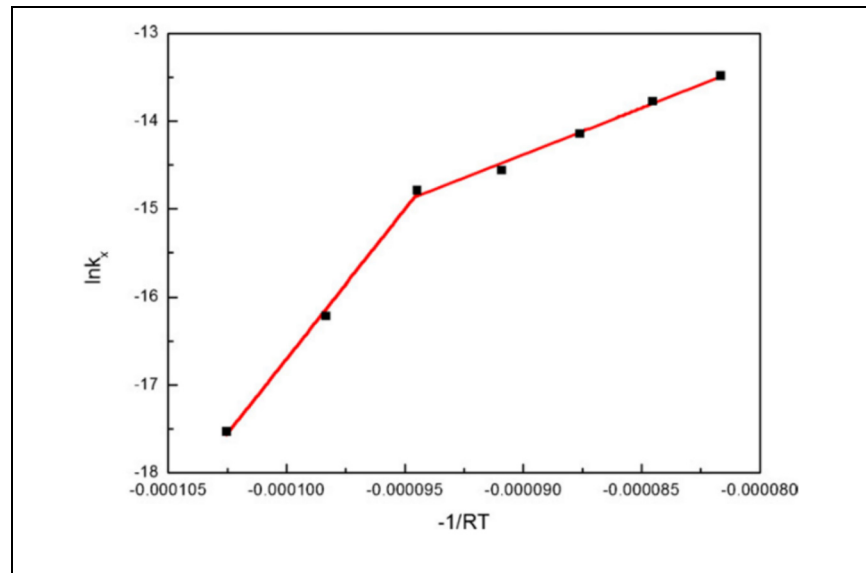
Figure 1.22 Determination of activation energy for micro-alloyed
steel, oxidized at the temperature range of 1173 to 1473 K
Taken from Liu et al. (2013, p. 1069)

The oxide layer of pure iron is formed of three layers: wustite (FeO), magnetite (Fe_3O_4), and hematite (Fe_2O_3). It is reported that the fraction of these layers is generally 0.95:0.40:0.10 (Suarez et al., 2009; Zambrano, Coronado, & Rodríguez, 2015).
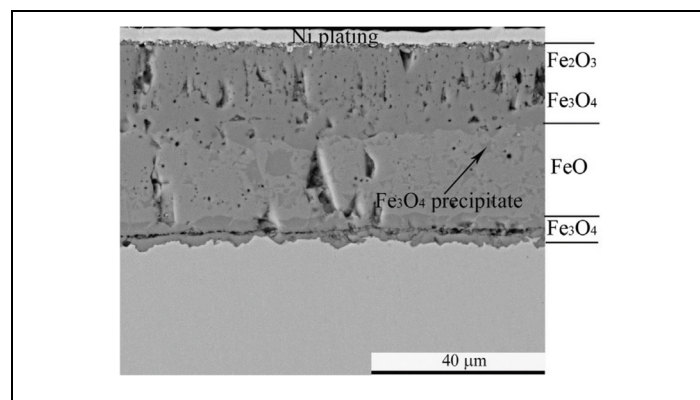
Figure 1.23 Different oxide layers of pure iron,
oxidized in oxygen for 10 h at 923 K
Taken from Yuan et al. (2013, p. 312)

Wustite is the closest layer to the base metal. The growth of wustite is highly dependent on the diffusion of Fe. Magnetite is located as the intermediate layer. At the outermost, hematite is located as the hardest layer, which its growth depends on the diffusion of oxygen (R. Chen & Yuen, 2000; Suarez et al., 2009; Zambrano et al., 2015). These layers can be affected by material composition, oxidation temperature, oxidation time, and oxidation atmosphere. Figure 1.23 shows the different oxide layers for the oxidation of pure iron in oxygen for 10 h at 923 K.

Furthermore, the fraction of these layers can vary depending on the alloying elements, oxidation atmosphere, oxidation temperature, and oxidation time. Liu et al. (Liu et al., 2013) assessed the oxidation of micro-alloy steel, oxidized at 1173-1473 K for 1800 s. The results indicated the increase in thickness fraction of wustite by increasing the oxidation temperature and time. The fraction of the magnetite layer decreased, while the hematite layer did not experience a remarkable change (see Figure 1.24).
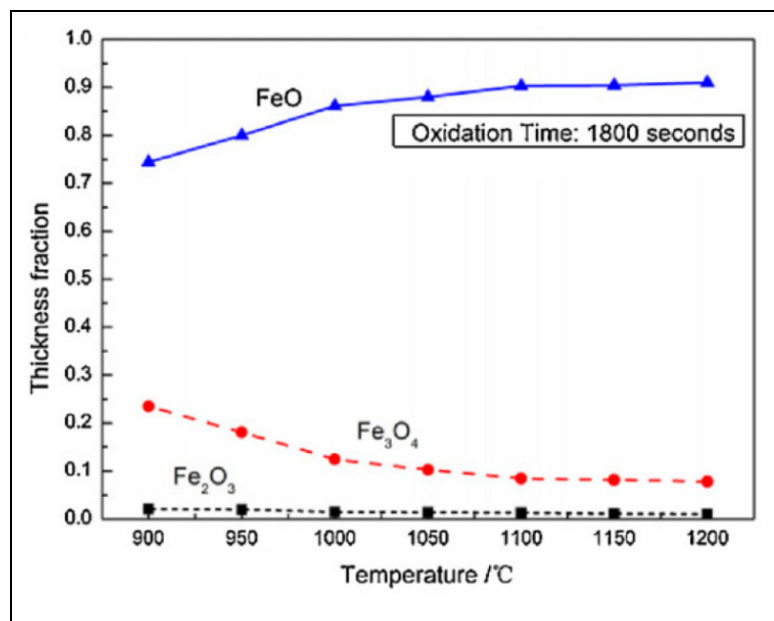
Figure 1.24 The variation of thickness fraction of oxide layers
for micro-alloyed steel oxidized at 1173-1473 K for 1800 s
Taken from Liu et al. (2013, p. 1074)

Chen and Yuen (R. Y. Chen & Yuen, 2009) investigated the oxidation of low-carbon steels in 1173 in an oxidizing atmosphere of $17H_2O-N_2$. They acquired a magnetite layer (no hematite layer) beside the inner wustite layer. Yun et al. (Yun, Ha, Kang, & Wang, 2013) evaluated low-carbon steel oxidation at a temperature range of 773-973 K in a moist atmosphere employing XRD analysis. As shown in Fig. 1.25, wustite was not detected at the sample oxidized at 773 K, whereas wustite had the highest thickness fraction for sample oxidized at 973 K.
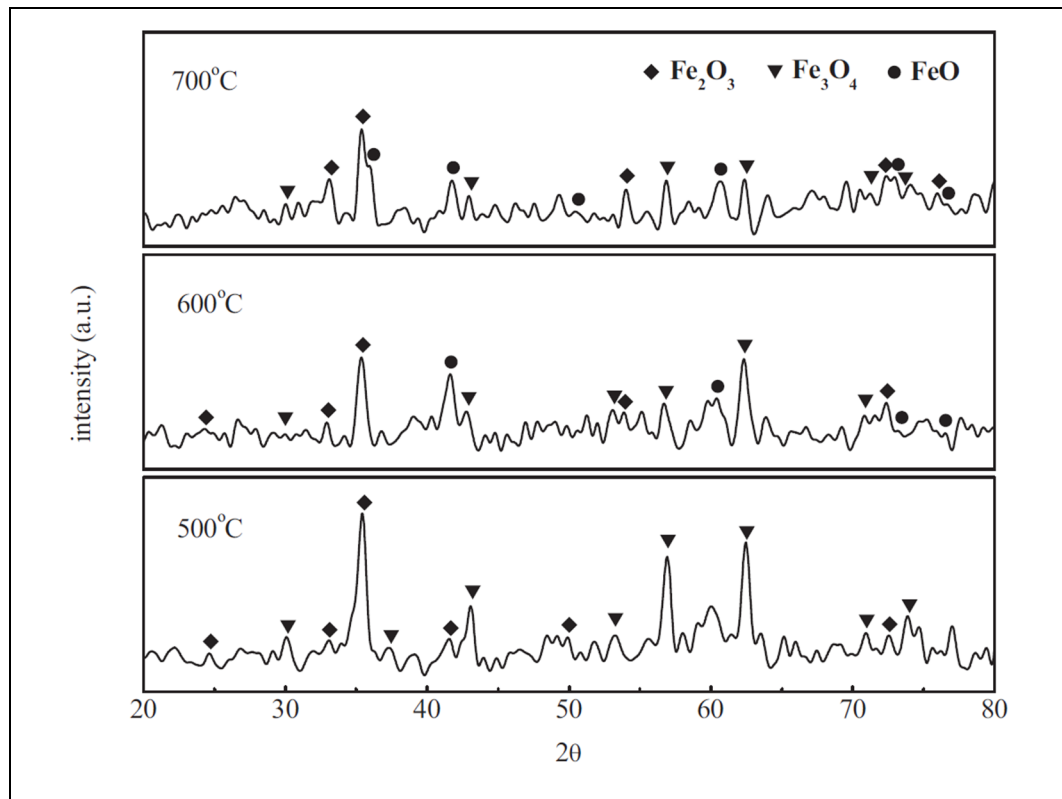
Figure 1.25 XRD patterns of samples oxidized in the
moist ambiance at different temperatures
Taken from Yun et al. (2013, p. 1256)

The oxidation of low-carbon steel in the different atmosphere and temperatures (1073 to 1423 K) was investigated by Abuluwefa et al. (H Abuluwefa et al., 1996). The outcomes revealed a

single wustite layer after oxidation for 1 hour in carbon dioxide and water vapor. The samples
oxidized for the same duration in oxygen had all three layers (see Figure 1.26).
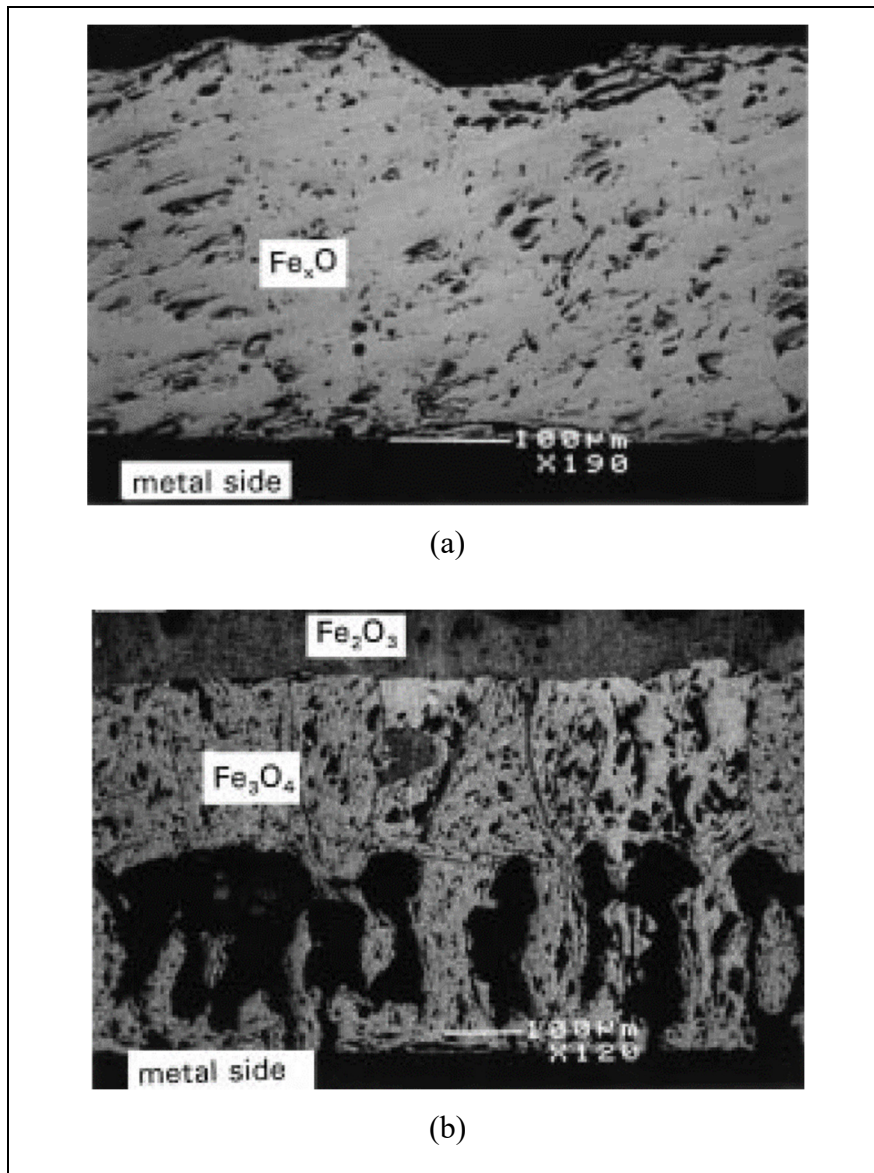
Figure 1.26 Microstructure of oxide layers for low-carbon oxidation
for 1 hour at oxidation temperature of 1423 K in the atmosphere of:
a) carbon dioxide, and b) oxygen
Taken from Abuluwefa et al. (1997, p. 1639)

As indicated, the alloying elements can remarkably influence the oxidation kinetics and oxide
layers. Although some former studies assessed the effects of alloying elements on oxidation,

the underlying mechanism for alloying elements' influence is not profoundly investigated. Hence, this study initially aims to assess the oxidation kinetics by oxidation time and temperature. Then, the effect of Ni is investigated on oxidation and oxide morphology.

1.6   Heat transfer of large-sized ingots

Prior to the open-die forging operations, the large-sized ingots are heated in gas-fired furnaces to bring them to the desired temperature. The ingots are transferred employing ceiling supported workstation cranes to forging anvils (see Figure 1.27).

Figure 1.27 Heating large-sized ingots in gas-fired furnaces and transfer
to forging by cranes

The ingots lose the heat during the transfer from furnace to forging and on the forging anvils through convection, radiation, and conduction. The ingot's heat transfer will decrease the ingot's temperature, causing a temperature gradient from the surface to the core. This issue can lead to undesired mechanical characteristics and possible cracks, which in some cases will bring the ingot to scrap. The ingot's temperature drop will also increase the deformation loads; sometimes, it would not be possible to accomplish the deformation process. Hence, the ingot should be brought back to the furnace and heated up again to the desired temperature, which is time and cost consuming.

1.6.1 Heat transfer by convection

The heat transfer by convection occurs through two mechanisms. In the first mechanism, the energy is transferred by random molecular motion (diffusion). In the second mechanism, the heat is transferred by the bulk motion of fluids. The large number of molecules that are moving in the presence of temperature difference accomplish the heat transfer. In other words, the convection is realized by the contact of a fluid in motion with a bounding surface at different temperatures. The convection heat transfer is classified based on the motion of the fluid. If an external source forces the fluid motion, such as a fan or pump, the convection is called forced convection.

In contrast, the free (or natural) convection is when the buoyancy forces make the fluid motion. These forces are attributed to the variation in fluid density caused by the changes in fluid temperature. The air will increase in temperature by contacting the hot surfaces, which causes a decrease in air density. This lighter air (compared to the surrounding atmosphere) will ascend vertically by buoyancy forces, and the cooler ambient air will replace it. In some heat transfer cases, a mixture of forced and natural convection can be observed (Bejan & Kraus, 2003; Bergman, Incropera, DeWitt, & Lavine, 2011).

Regardless of the nature of convection, the heat transfer by convection can be described by Newton's law of cooling as follows (Bejan & Kraus, 2003; Bergman et al., 2011):

$$q'' = h(T_s - T_\infty) \tag{1.14}$$

where q'' is the convective heat flux (W/m^2), T_s is the surface temperature (K), T_∞ is the fluid temperature, and h is the convective heat transfer coefficient (W/m^2.K). The h coefficient is dependent on the boundary conditions, the geometry of the surface, nature of fluid motion (free or forced), and fluid thermodynamic and transport properties, which should be obtained for each specific heat transfer condition. In the current study, the ingot is in contact with the free air and cools down by natural convection during the transfer from the furnace to the forging

press and deformation. The h values should be acquired based on the temperature variation on different ingot surfaces to assess the large-sized hot ingot's cooling. The calculation of the h value will be discussed throughout this thesis.

1.6.2   Heat transfer by conduction

Conduction is interpreted as the transfer of energy from more energetic particles to less energetic particles of a substance by the interaction between them. For gas with a gradient of temperature, the temperature at any given point is associated with gas molecules' energy at that point's proximity. When the adjacent molecules collide, a transfer of energy will occur from higher energetic molecules to lower ones. The situation is much the same for the liquids, characterized by the closer molecule distance and stronger molecule interactions. The energy transfer by molecular interaction is attributed to the atomic activity as the lattice vibrations for solids. If the heat transfer by conduction varies by time, the heat transfer process is transient, whereas a constant heat transfer is called steady-state. The heat transfer by conduction for an isotropic material without internal heat generation sources is as follows (Faghri, Zhang, & Howell, 2010):

$$\rho c \frac{\partial T}{\partial t} = \frac{\partial}{\partial x}\left[k \frac{\partial T}{\partial x}\right] + \frac{\partial}{\partial y}\left[k \frac{\partial T}{\partial y}\right] + \frac{\partial}{\partial z}\left[k \frac{\partial T}{\partial z}\right] \tag{1.15}$$

where ρ, c, and k are density (kg/m3), specific heat capacity (J/Kg. K), and Conductive heat transfer coefficient (W/m.K), respectively. The indicated parameters can vary by temperature, which can remarkably affect the outcomes. Hence, such variations should be considered for the numerical simulations. There is a conduction heat transfer between the ingot and the thermally grown oxides for the current study. Furthermore, during the forging, conduction heat transfer occurs between the ingot and forge anvils by the contact between them. This conduction is also affected by the presence of oxide layers.

1.6.3   Heat transfer by radiation

The thermal radiation is the emitted energy from matter (solid, liquid, or gas) at a non-zero temperature. The emitted energy can be related to the modifications in the constituent atoms or molecules' electron configurations. The radiated energy is emitted by electromagnetic waves (or photons). In other words, the convection and conduction heat transfer modes need matter to realize the heat transfer, but radiation does not. Indeed, radiation is the most efficient heat transfer mode under vacuum. The emitted energy from a surface by radiation originates from the thermal energy of matter bounded by the surface. The intensity of emitted energy by radiation from a surface depends on the surface quality (surface roughness) and temperature. In general, the heat exchange by radiation can be expressed as follows (Bergman et al., 2011; Howell, Menguc, & Siegel, 2010):

$$q'' = \epsilon\sigma(T_s^4 - T_{sur}^4) \tag{1.14}$$

where ε is a radiative property, between 0 and 1, σ is the Stefan–Boltzmann constant ($\sigma=5.67\times10^{-8}$ W/m^2.K^4), T_s is the temperature of the surface, and T_{sur} is the temperature of the surrounding environment. Equation 1.14 provides how efficiently a surface emits energy relative to a blackbody as the ε equals 1 for a blackbody. In this study, the ingot loses the temperature by radiation from all surfaces to ambient, and the radiation is remarkably affected by the growth of oxide layers. The heat transfer by radiation will be assessed thoroughly in this thesis.

1.6.4   Effect of thermally grown oxides on heat transfer of large-size ingots

Heat transfer is an inevitable outcome of contact between substances at different temperatures. However, the heat flow can be reduced or suppressed by thermal insulation. Thermal insulation reduces heat transfer by conduction or convection between the contacting materials at a different temperature or radiation influence range. Thermal insulation is realized by employing low thermally conductive materials to attain even lower thermal conductivity (Bahadori, 2014).

As stated before, the thermally grown oxides are inevitable in the hot deformation of the majority of steels. Also, the above studies reported low thermal conductivity for iron oxides. Torres and Colás (Torres & Colás, 2000) indicated the thermal conductivity of 3.2, 1.5, and 1.2 W/m.K for oxides layers of wustite, magnetite, and hematite, respectively. These values are far below the general thermal conductivity range of 25.3 to 93 W/m.K for low carbon steels (Bergman et al., 2011). Thus, considering that each oxide layer can demonstrate different characteristics, as discussed before, and the low conductivity of oxide layers, which can make them categorized as thermal insulators, the effect of oxide layers should be considered in heat transfer of large-size hot ingots.

Despite the many publications on the experimental or modeling evaluation of steels' heat transfer during hot deformations (like Bai et al. (Bai et al., 2012), Chang et al. (Y. Chang, Li, et al., 2016), Dubey and Srinivasan (Dubey & Srinivasan, 2013), Morgado et al. (Morgado, Coelho, & Talukdar, 2015)), the effect of the oxide layer on heat transfer was not assessed comprehensively.

Dubey et al. (Dubey, Agarwal, & Srinivasan, 2012) considered the oxide growth in their simulation of heating of a steel billet. The results were close to the real industrial situation due to the oxide growth. Jang et al. (Jang et al., 2010) considered the influence of oxide layer growth on high carbon steel heating at 1473 k in a reheating furnace. Their results showed that the oxide layer decreased the heating rate of slabs because of its low conductivity, which increased the heating time. Figure 1.28 compares the steel slab's temperature profiles with and without oxide on top and bottom surfaces.
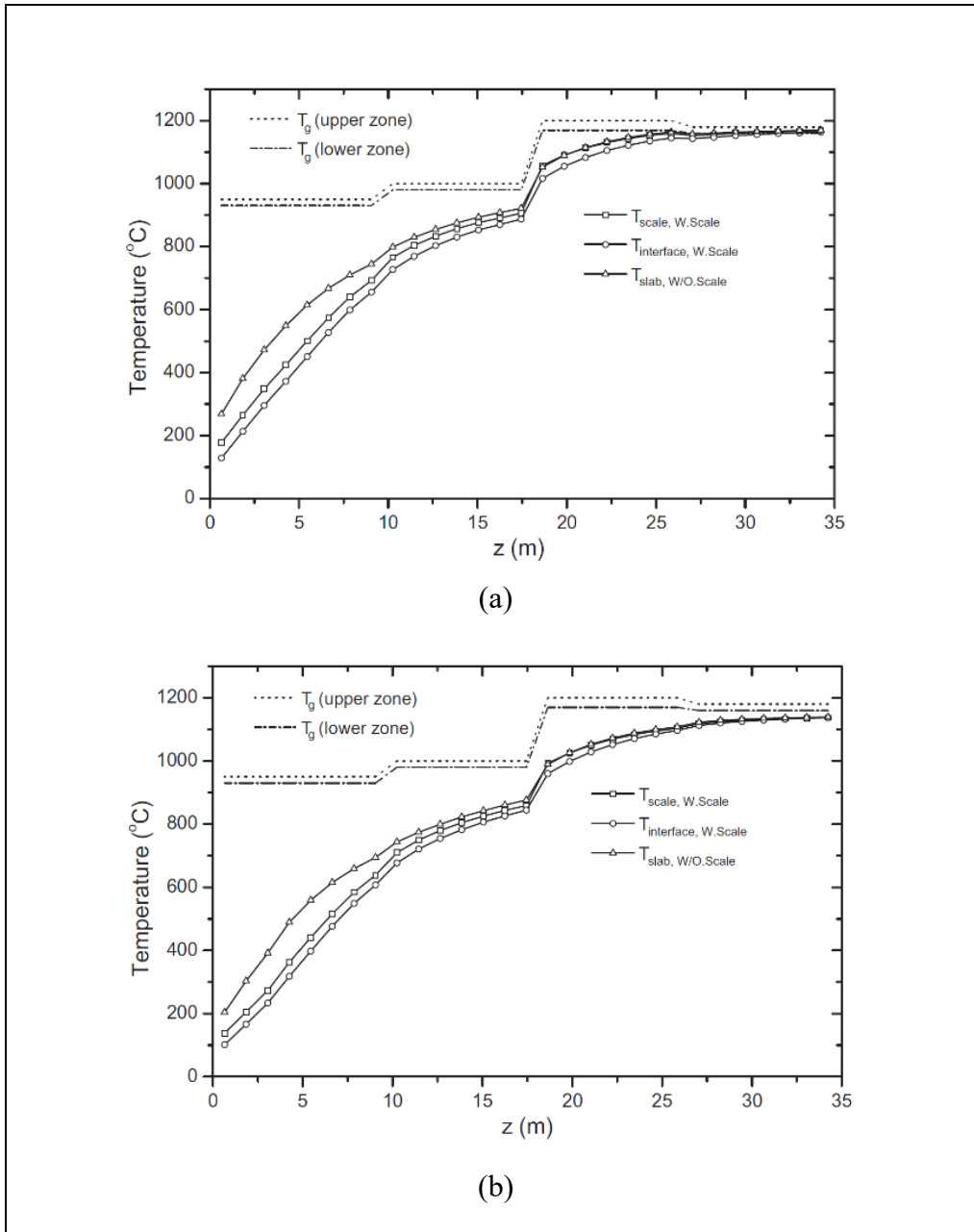
Figure 1.28 Temperature of steel slab in reheating furnace with and without
oxide layers on the slab surfaces of: a)top, and b)bottom
Taken from Jang et al. (2010, p. 4331)

Dong et al. (Dong, He, Sun, Liu, & Hong, 2017) assessed the temperature field of the slab
during heating, considering the oxide layer effect using the finite difference method. Their
results demonstrated that the oxide layer could significantly influence the slab's temperature

gradient in different zones of the furnace. Figure 1.29 gives the slab's temperature during heating with and without the oxide layer for the preheating zone and second heating zone of the furnace.
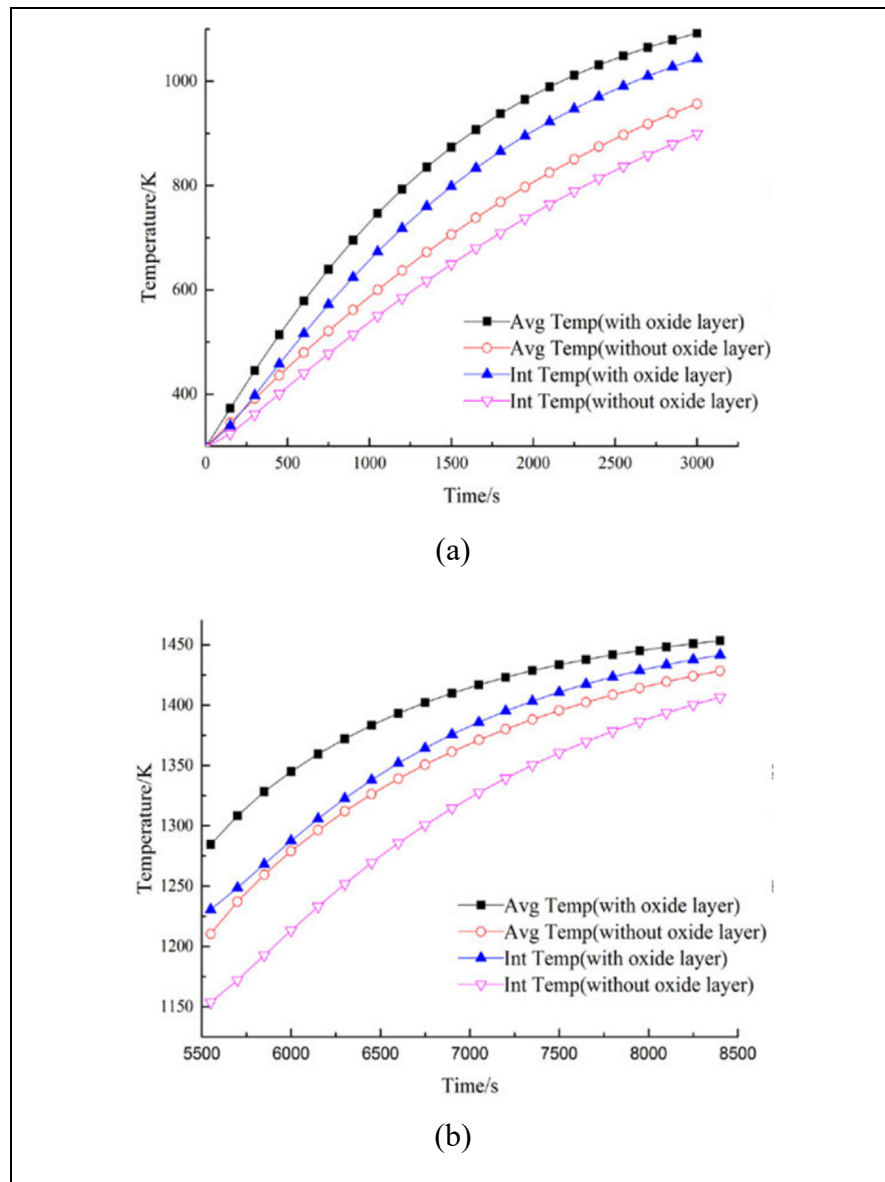
Figure 1.29 Slab temperature with and without the oxide layer
during the heating process in the furnace:
a) preheating zone, and b) second heating zone
Taken from Dong et al. (2017, p. 157)

Kim (M. Kim, 2013) evaluated the heating of a large-sized high carbon steel slab at 1473 K with an oxide layer. The outcomes indicated that the oxide layer suppresses the heat transfer from the furnace to the slab due to the low oxide layer conductivity. As illustrated in Figure 1.30, the average temperature of the slab was 100 °C lower compared to the slab without scale in some regions.
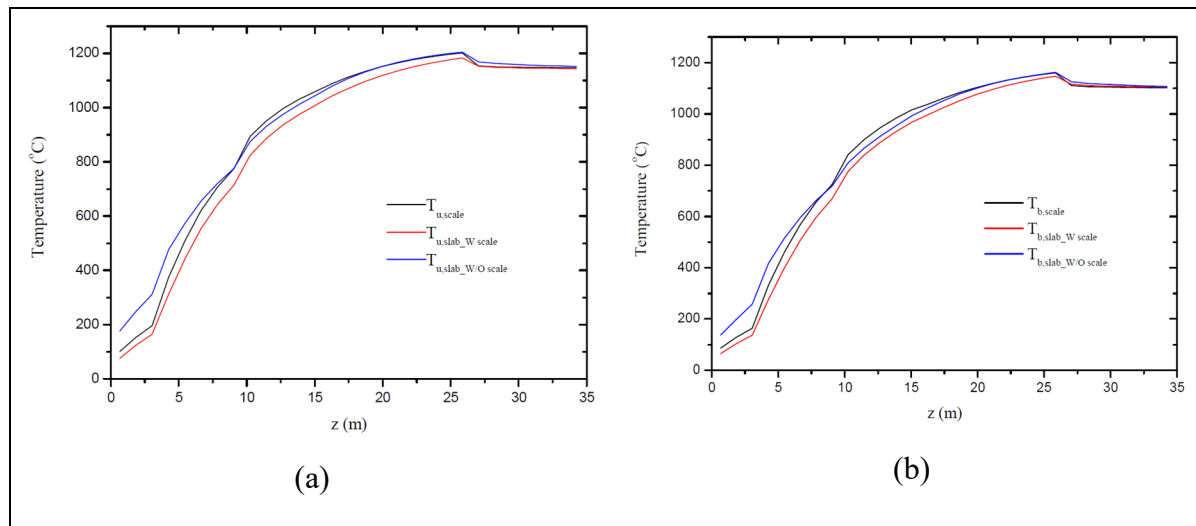
Figure 1.30 Temperature profiles of the slab with and without oxide layer
during heating on the surfaces of: a) top, and b) bottom
Taken fromKim (2013, p. 1340)

Wang et al. (X. Wang, Wang, & Li, 2018) evaluated the heating of dynamic slabs in walking-beam reheating furnaces with an oxide layer. The results showed different heating contours for slabs with and without oxide layers.
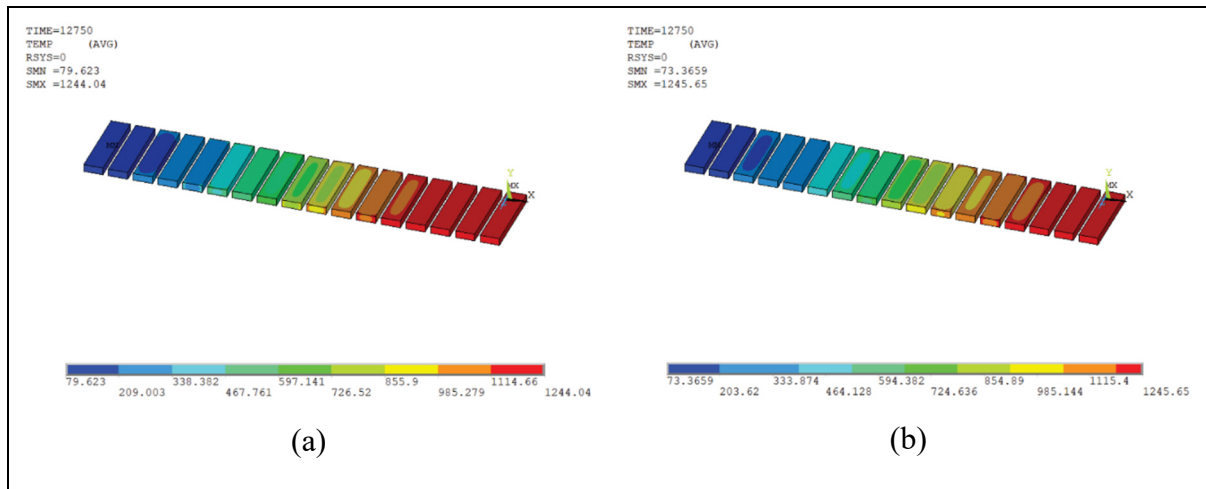
Figure 1.31 Temperature filed contours for heating of slabs:
a) without oxide, and b) with 2 mm of oxide
Taken from Wang et al. (2018, p. 2052)

Their results showed that the slab's soaking time increased for 1000 s by 2 mm of oxide layers compared to a slab without oxide. Jaklič et al. (Jaklič, Glogovac, Kolenko, Zupančič, & Težak, 2002) investigated the temperature decrease of billet in transportation from the furnace to the rolling mill. A three-dimensional finite-difference model was developed and verified, utilizing a thermal camera. The results showed a remarkable difference in the billet's temperature with and without the oxide layer (see Figure 1.32).

As addressed by these former studies, the oxide layers can remarkably affect an ingot's heat transfer. This issue can cause undesired material characteristics and distortion. Thus, in the second part of this study, the effect of oxide layers on heat transfer will be evaluated.
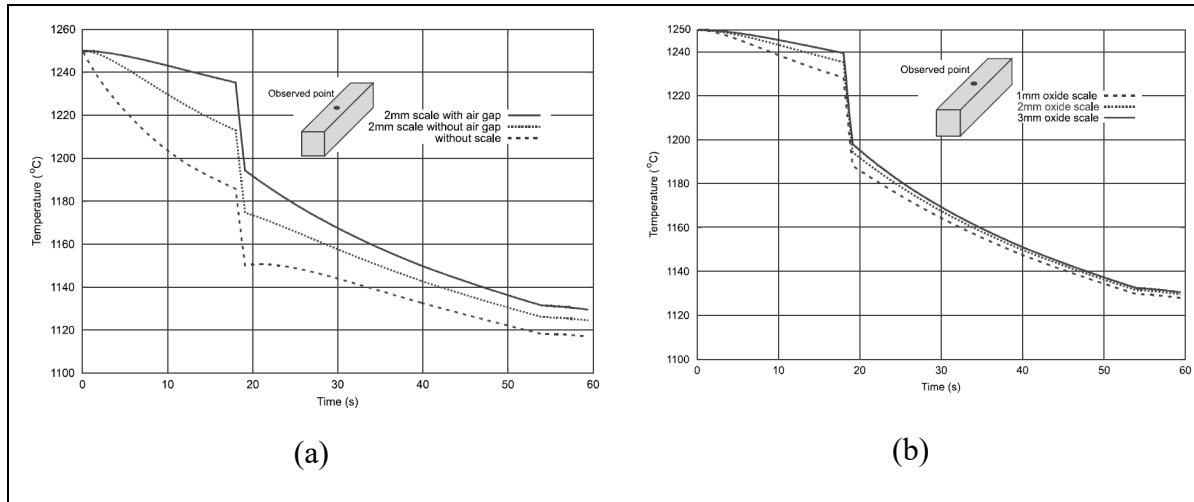
Figure 1.32 Comparison of billet temperature for: a) billet with and without oxide,
and b) billet temperature for different oxide thickness
Taken from Jaklič et al. (2002, p. 882)

1.7   Mechanical characterization of oxide layers by indentation

The different oxide layers can demonstrate different mechanical characteristics. As each layer's hardness is different, the frictional conditions can be affected by oxide in the contact interface. Indentation tests were widely utilized to evaluate the characteristics of thin coatings and films. In this regard, micro-indentation and nano-indentation tests were employed to assess the formed scales and different conditions. A hard diamond tip is forced into a sample, and a graph is illustrated by recording the force to the penetration value top sloid, known as the load-depth curve (see Figure 1. 33). As given, the indenter is applied to the surface of a solid to a specific load, which stays at the peak load for a predetermined time, followed by the unloading (Nalwa, 2001; Sharpe, 2008).

A commonly used tool is the Vickers tip. This method is followed by Brinell test basics, but a diamond pyramid replaces the steel ball with 136° of the angle between pyramid surfaces and the tip radius of less than 200 nm.
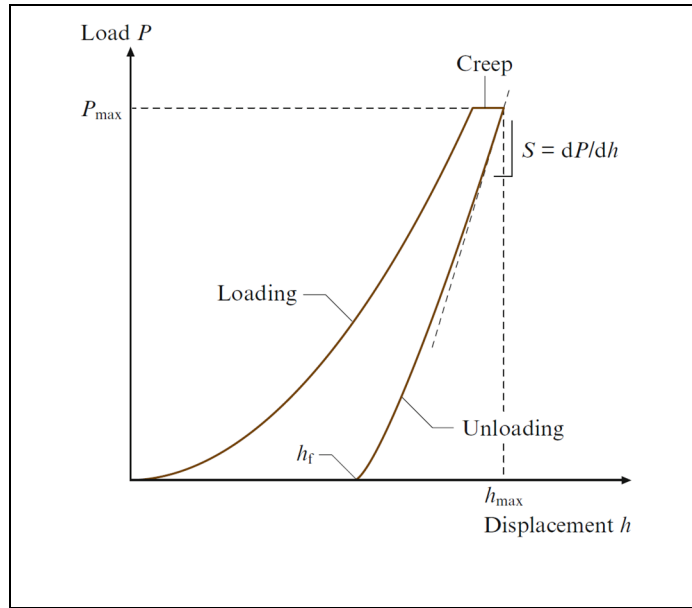
Figure 1.33 Schematic of the load-depth curve
for indentation
Taken from Sharpe (2008, p. 392)

The Vickers hardness can be acquired as follows (Sharpe, 2008):

$$DPH = \frac{2P \sin\left(\frac{136°}{2}\right)}{d^2} \tag{1.16}$$

where DPH is the diamond pyramid hardness, P is the applied load (mN), and d is the average of two diagonals of pyramid imprint on the surface (µm). This test is typically conducted for loads of less than 1000 g, which is known as the micro-indentation. The typical Vickers indentation schematic is illustrated in Figure 1.34.

In Figure 1.34, P_{max} is the maximum load, h_{max} is the maximum penetration depth, and h_f is the final depth, which are the necessary parameters to describe the indentation process. As As reported by Doerner and Nix (Doerner & Nix, 1986) and further developed by Oliver and Pharr (Warren Carl Oliver & Pharr, 1992), the load-depth curve's unloading part is used to determine the tested sample's elastic modulus and hardness. During the nano-indentation, both elastic and

plastic deformations occur. However, the unloading part is purely defined as the elastic response of the system.
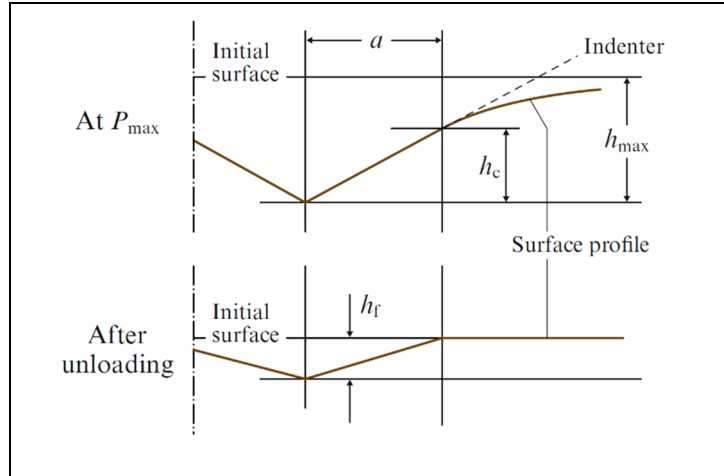
Figure 1.34 The schematic of solid surface
in contact with the indenter
Taken from Sharpe (2008, p. 393)

Hence, the slope of the unloading part of the load-depth curve can be obtained as follows (Sharpe, 2008):

$$\frac{dP}{dh} = \beta \frac{2}{\sqrt{\pi}} E^* \sqrt{A} \tag{1.17}$$

where A is the projected contact area, and β is the correction coefficient to consider the possible variations caused by plastic deformation. Different values have been reported for β, which is still debatable. For instance, Lawrence (Lawrence, Adams, Bahr, & Moody, 2013) reported that β equals 1.034. Olivier and Pharr (Warren C Oliver & Pharr, 2004), and Fischer-Cripp (Fischer-Cripps, 2011) obtained 1.1 for β. Recent studies suggest that 1.034 or 1.05 will lead to reasonable accuracy to obtain elastic modulus. Also, the contact depth h_c can be acquired as follows (Sharpe, 2008):

$$h_c = h_f - \varepsilon \frac{P_{max}}{dp/dh} \tag{1.18}$$

where ε is a constant equal to 0.75 for pyramid indenters. Furthermore, the reduced elastic modulus E^* for two contacting solids cab be defined as follows (Bhushan, 2000; Sharpe, 2008):

$$\frac{1}{E^*} = \frac{1 - v_i^2}{E_i} + \frac{1 - v_s^2}{E_s} \tag{1.19}$$

Where E and ν are the elastic modulus and Poisson ratio, respectively. The i and s indices are referring to indenter and sample, respectively. For the conventional diamond indenter, E_i and v_i equal to 1141 GPa and 0.07, respectively.

Indentation tests are widely utilized to evaluate the characteristics of thin coatings and films. In this regard, micro-indentation and nano-indentation tests were employed to assess the formed scales and different conditions. Employing the micro-hardness test, Takeda et al. (Takeda, Onishi, Nakakubo, & Fujimoto, 2009) assessed the hardness of formed oxide layers at room temperature. For the formed oxide layers on the iron, the hardness of wustite, magnetite, and hematite was measured by Vickers to be 3.5, 4, and 6.7 HV, respectively. These values equaled 1.67, 1.64, and 3.27 HV for sintered oxides. In a similar testing method by micro-hardness, Barrau et al. (Barrau, Boher, Vergne, Rezai-Aria, & Gras, 2002) indicated for wustite, magnetite, and hematite to have hardness values of 270– 300, 420–500, and 1030 HV, respectively. Luong and Heijkoop (Luong & Heijkoop, 1981) reported 460, 540, and 1050 for scale layers at room temperature. In a similar study Spuzic et al. (Spuzic, Strafford, Subramanian, & Savage, 1994) indicated values of 300, 450, and 1050 HV for three oxide layers of wustite, hematite, and magnetite. Amano et al. (Amano et al., 2006) investigated the characteristics of oxide layers formed on the Fe-Si alloys at room temperature. The samples of oxide were prepared under oxygen flow at 1273 K, as shown in Figure 1.35.
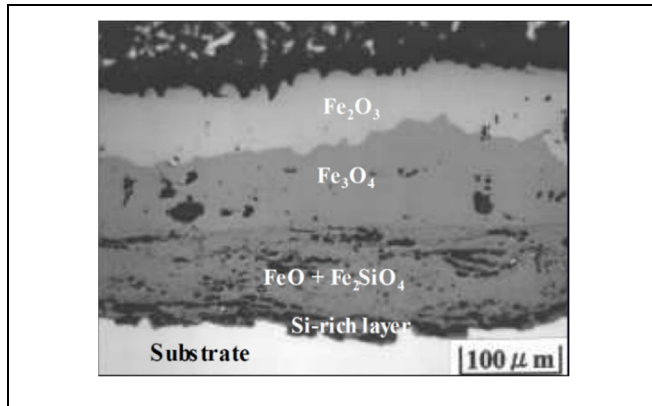
Figure 1.35 Formed oxide layers on
Fe-Si alloy at 1273 K under oxygen flow
Taken from Amano et al. (2006, p. 471)

The hardness values of 356, 407, and 683 HV was acquired for wustite, magnetite, and hematite, respectively. Magnetite was reported by Hutchings and Shipway (Hutchings & Shipway, 2017) to demonstrate a hardness of 370–600 HV. Zambrano et al. (Zambrano et al., 2015) investigated the hardness of formed oxide layers on low carbon steel at 1473 K in the air by micro-hardness. Figure 1.36 shows the formed oxide layers at 1473 K for 4 hours.
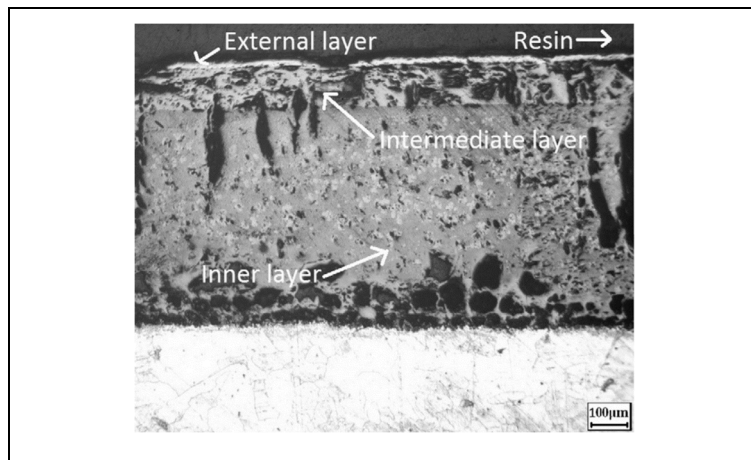
Figure 1.36 Formed oxide layer on low carbon steel
at 1473 K for 4 hours
Taken from Zambrano et al. (2015, p. 157)

The outcomes showed hardness of 317.7±24.1, 465.2±32.3, and 975.5±62.7 HV for wustite, magnetite, and hematite, respectively. Saeki et al. (Saeki, Ohno, Sakai, Niya, & Sato, 2011) compressed α-Fe$_2$O$_3$ powder using cold isostatic pressing and sintered it at 1373 K to produce hematite samples. The hematite's Young modulus was measured to be 220 GPa at room temperature, utilizing the sine waves at 400 – 1000-Hz. Zamri et al. (Zamri, Kosasih, Tieu, Zhu, & Zhu, 2012) investigated the outer hematite layer formed on the high-speed steel hot rolling work rolls. Figure 1.37 shows the conducted nano-indentation on the scale at room temperature.
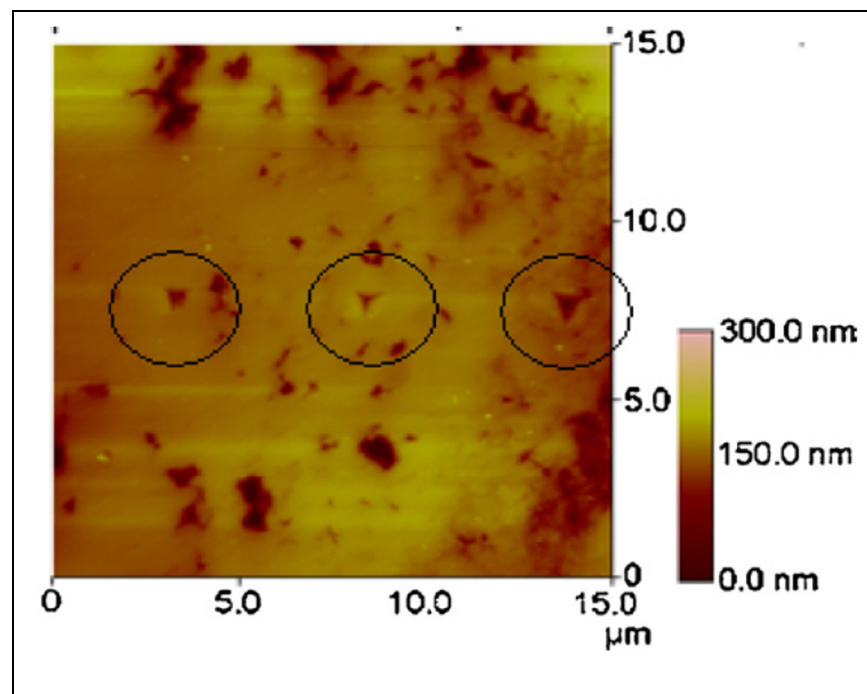
Figure 1.37 Conducted nano-indentation on the hematite layer formed
on the high-speed steel hot rolling work rolls
Taken from Zamri et al. (2012, p. 2598)

The hardness of hematite was 24.4-27.9 GPa, while 250-260 GPa was obtained for elastic modulus. Chicot et al. (Chicot et al., 2011) evaluated the characteristics of magnetite and hematite employing nano-indentation. The outcomes were hardness of 6.3 and 8.2 GPa and young modulus of 175 and 359 GPa for magnetite and hematite. The similar study by Seo and

Chiba (Seo & Chiba, 2001) determined 5-8 GPa of hardness and 174 GPa of elastic modulus for magnetite, utilizing nano-indentation at room temperature. As illustrated in Figure 1.38, Zambrano et al. (Zambrano et al., 2015) employed nano-indentation to assess the different oxide layers at room temperature. The oxide layers were formed at 1473 K on low carbon steel.
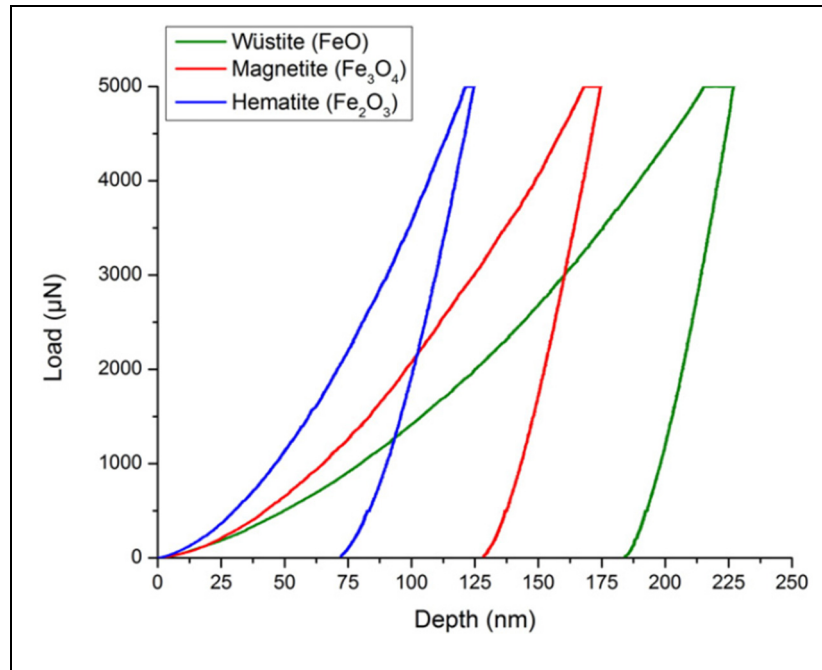
Figure 1.38 Nano-indentation on different oxide layers of
low carbon steel formed at 1473 K
Taken from Zambrano et al. (2015, p. 159)

The results showed hardness of 5.5±1.1, 6.5±0.9, and 12±2.5 GPa for wustite, magnetite, and hematite.

The above studies clearly reveal discrepancies regarding the characteristics of different oxide layers. So, in the following part of this study, scale layers' characteristics are assessed employing micro-indentation and nano-indentation tests. Furthermore, the outcomes will be used in the following parts to evaluate the effect of oxide layers on the interfacial friction between anvils and ingot.

1.8   Effect of thermally grown oxides on interfacial friction between die and ingot

The ring compression test is a widely employed method for the quantitative assessment of friction. In this test, a ring is plastically deformed between two flat platens up to a predetermined height. The geometry of the ring can be an indication of friction (Zareh-Desari & Davoodi, 2016). In case of low friction between dies and specimen, the ring's material will flow outward, resulting in the increase of the internal and external diameters of the ring. In case of high friction, the ring's material will flow inward, decreasing the internal diameter of the ring (Zareh-Desari & Davoodi, 2016). A schematic of this method is shown in Figure 1.39.
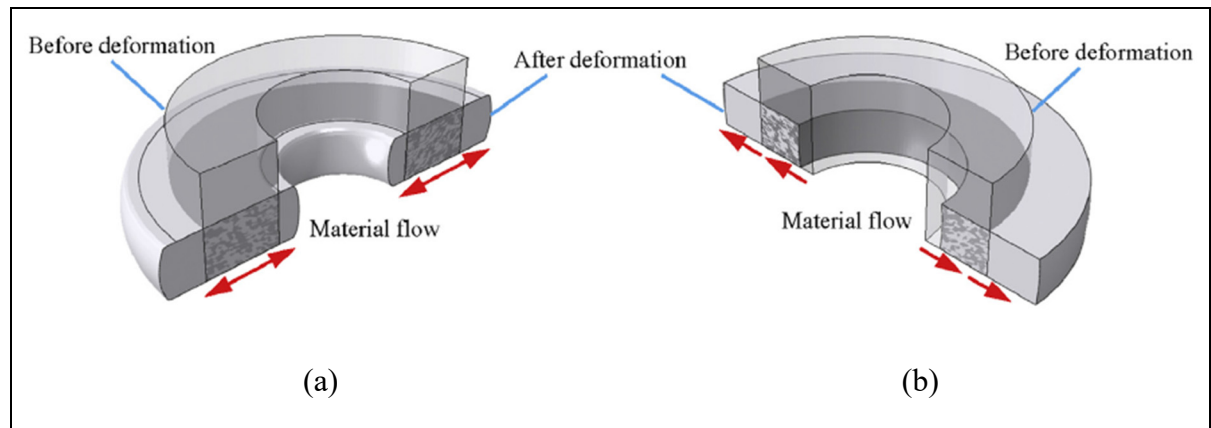
Figure 1.39 Material flow in the ring test: a) high friction, and b) low friction
Taken from Zareh-Desari and Davoodi (2016, p. 1202)

Rajesh and SivaPrakash (Rajesh & SivaPrakash, 2013) investigated the interfacial friction of aluminum during deformation at room temperature utilizing different lubrications of zinc stearate, molybdenum disulphide (MoS_2), and graphite powder. As given in Figure 1.40, the variations of internal diameter were illustrated by changes in the ring's height for different friction coefficients. These curves are known as friction calibration curves. Figure 1.40 shows the calibration curve of aluminum for deformation at room temperature employing Zinc stearate lubricant.
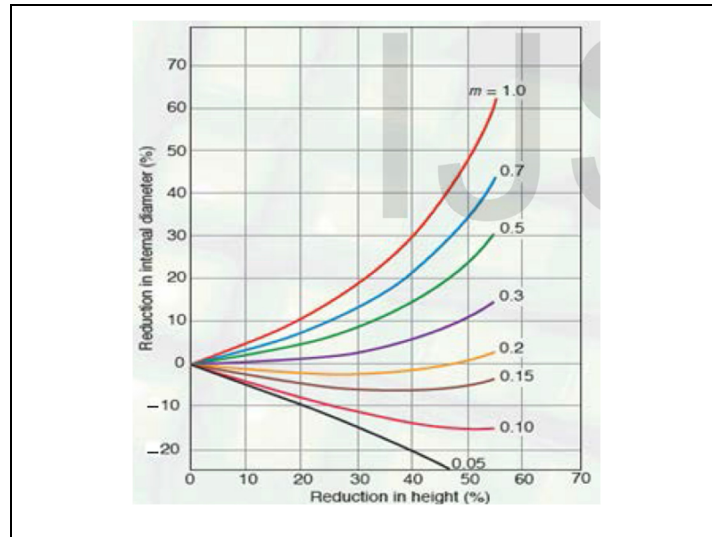
Figure 1.40 calibration curve of aluminum for
deformation at room temperature employing
Zinc stearate lubricant
Taken from Rajesh and SivaPrakash (2013, p. 1165)

This study's outcomes acquired the minimum friction coefficient of m=0.14 for Zinc stearate and Molybdenum disulphide; and the highest friction of 0.52 for dry deformation (see Figure 1.41).
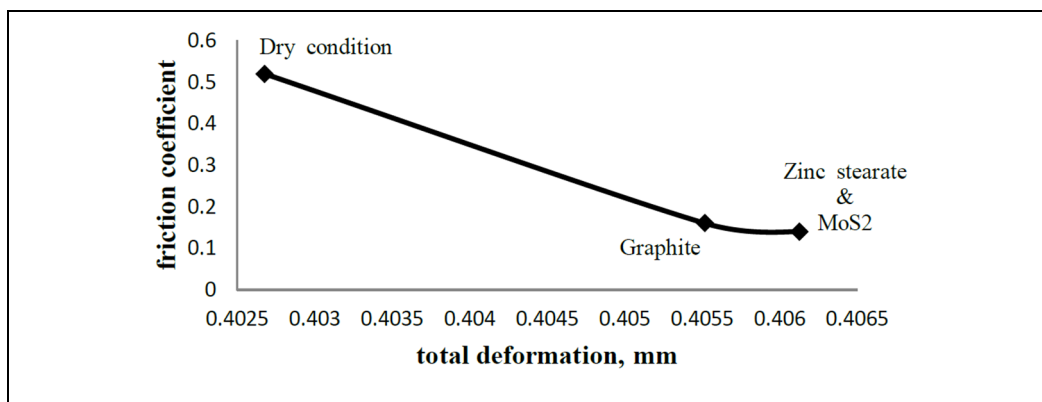
Figure 1.41 Obtained friction coefficients for different lubricants employed
for deformation of aluminum
Taken from Rajesh and SivaPrakash (2013, p. 1169)

The interfacial friction of 316 L stainless steel during deformation in the temperature range of 1173 to 1473 K was evaluated by Ashimabha et al. (Ashimabha, Parthasarathi, Arvinth, Utpal, & Jeevanantham, 2018) employing ring test. The results showed that for dry deformation, the friction increased by increasing the temperature. However, at 1473 K, due to the thermal softening, the friction decreased. Shahriari et al. (Shahriari, Sadeghi, Ebrahimi, & Kim, 2011) assessed the interfacial friction of nimonic 115 superalloy at deformation temperatures of 1373 and 1448 K with different lubricants of graphite powder, glass powder, and mica sheets. The rings with dimension ratio of 11:6:6 mm for outer diameter, inner diameter, and height were utilized for this study. As illustrated in Figure 1.42, the lowest friction was acquired by mica lubricant.
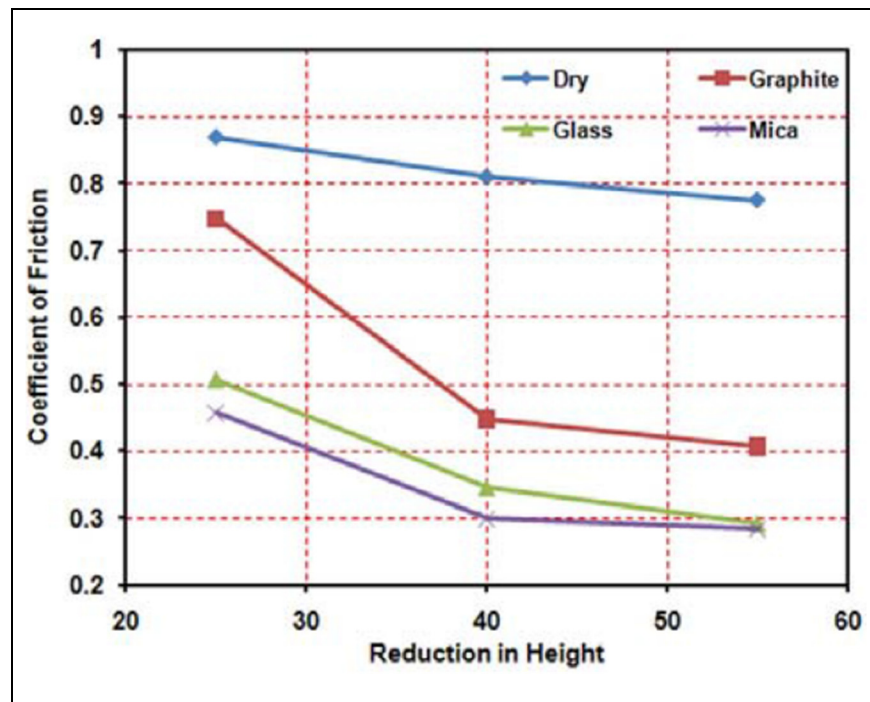
Figure 1.42 The obtained friction coefficient for
deformation of nimonic 115 superalloy at 1448 K
for different lubricants
Taken from Shahriari (2011, p. 381)

Zhu et al. (Zhu et al., 2011) investigated Ti-6Al-4V titanium alloy's interfacial friction with a ring dimension ratio of 4:2:1 at 1213 K for dry and glass lubricant. The deformed rings are shown in Figure 1.43. The dry deformation friction was 0.59 compared to the 0.35 friction by glass lubricant.

Figure 1.43 Deformed rings at 30% and 50% deformation for:
a) glass lubricant, and b) dry friction
Taken from Zhu et al. (2011, p. 2076)

A common issue in lubrication is the escape of lubricant from the contact interface. Oyachi et al. (Oyachi, Utsunomiya, Sakai, Yoshikawa, & Tanaka, 2012) provided samples with pores on the surface to trap the lubricant during deformation to overcome this issue. So, the carbon steel samples were oxidized and then reduced to iron in an H_2 atmosphere. The rings were deformed, employing dry and lubricated by machine oil and grease, at room temperature. The outcomes demonstrated that the technique was practical for low-speed compression to decrease the friction by pores. However, the pores did not decrease the friction remarkably on high-speed compression compared to the smooth surface. The oxide layer's effect on the interfacial friction

of hot forging of carbon steel was investigated by Behrens et al. (Behrens et al., 2018). This study showed that the oxide layers could act as additional lubrication at high temperature, decreasing the interfacial friction. The oxide layer's effect on the interfacial friction during hot deformation of chrome steel was investigated by Matsumoto et al. (Matsumoto, Osumi, & Utsunomiya, 2014). The rings were oxidized at 1073 to 1423 K in the air. The acquired friction calibration curves are illustrated in Figure 1. 44, where the oxide layer demonstrated to decrease the friction. However, this study considered only a single wustite layer, instead of the generally observed three layers, and the oxide material was not used in the finite element modeling.
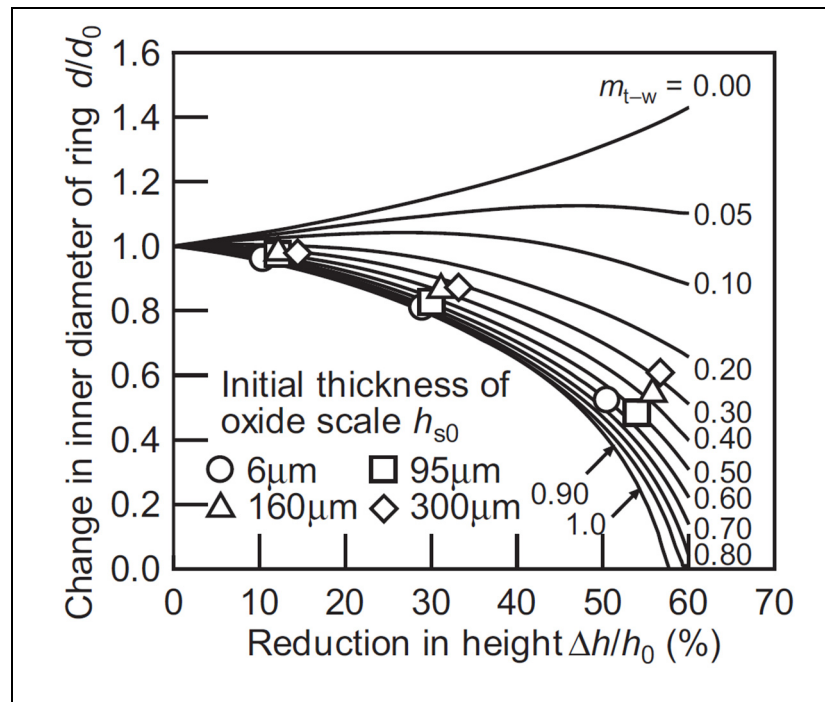
Figure 1.44 The developed friction calibration curve for
hot deformation of chrome steel with the oxide layer
Taken from Matsumoto et al. (2014, p. 654)

Furthermore, Matsumoto et al. (Matsumoto, Harada, & Utsunomiya, 2014) conducted the ring test on chrome steel rings oxidized in steam. It was found out that the friction was lower for

rings with oxide layers formed at steam. This phenomenon was due to the higher porosity of oxide layers formed at steam, as is shown in Figure 1.45.
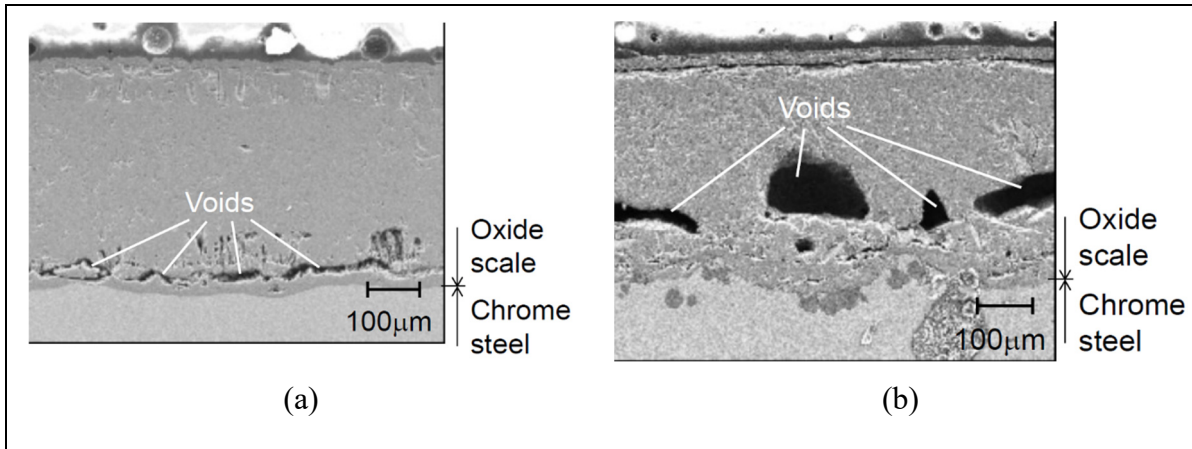
Figure 1.45 oxidized chrome steel rings at: a) air, and b) steam
Taken from Matsumoto et al. (2014, p. 196)

Considering the indicated former studies, the oxide layer can remarkably affect the interfacial friction between ingot and anvils. However, this effect was not comprehensively investigated as the oxide layer was considered a single wustite layer, the material behavior of oxide was not considered suitably, and the oxide morphology was omitted. Hence, as the final aim of the present thesis is the oxide layer effect is assessed on the interfacial friction, employing ring test and nano-indentation tests.

1.9 Thesis objectives and challenges

The discussed literature showed the open-die forging method's employment, as an important industrially used deformation method. For the industrial partner of this study, Finkl Steel Co., before open-die forging, the ingots are heated to 1533 K. The majority of steels experience thermal oxidation during hot deformation, which causes significant material waste. The oxidation rate can be affected by different parameters of oxidation temperature, oxidation time,

oxidation ambiance, and chemical composition. Furthermore, the mechanisms that the alloying elements can affect the oxidation kinetics is still an open question.

During and after forging, the ingot loses heat by convection and radiation to air, along with conduction to anvils. Considering the large-size ingots, the heat transfer during cooling is a complex issue. The temperature gradient can cause undesired material properties. The plasticity of ingot and deformation loads are affected by the temperature of the ingot. The fast heat loss of ingot may delay or result in failing of the forging operation, where a reheat will be needed, which is costly and time consuming for production. The contact between a hot ingot and a cold anvil can cause a thermal shock to die materials. Considering the indicated former studies, these heat transfer conditions can remarkably be affected by oxide layers' formation.

The interfacial friction between ingot and anvils during forging is of crucial importance. The interfacial friction directly influences the forming. The deformation loads can be affected by this interfacial friction. The bulging and undesired geometries are the outcomes of friction. The friction can cause wear on anvils too. Since the hardness of different oxide layers is different from the hardness of steel, the friction and wear will be significantly affected by scales' formation. The damage by wear and friction to forge anvils will be costly to repair or replace. According to the indicated issues and the challenges observed for the industrial partner, this thesis is defined to attain the following objectives:

1) Obtaining the kinetics of oxidation and material waste for two high-strength steels and evaluating the effect of oxidation time and oxidation temperature on the oxidation rate. As the ingots are heated in the furnace before the open-die forging process, the outcomes can be practical for the industrial partner to anticipate the material waste and ameliorate the loss. Furthermore, investigating the effect of Ni as an alloying element on thermal oxidation and the mechanism in which the Ni affects the oxidation. The results can clarify the effect of initial composition on the kinetics of oxidation.

2) Acquiring the oxide thickness for different oxidation time and temperature. Then, developing a finite element model to evaluate the cooling of a large-size ingot and investigating the effect of thermally grown oxide layers on the cooling and temperature gradient of the ingot. The outcomes can reveal the temperature evolution during cooling and prevent undesired material properties. The developed model should be verified through experimental evaluation in a real industrial situation. The thermal properties of steel and oxide are essential to be determined accurately. Also, the oxide layers tend to grow during the cooling too. So, that will be challenging to consider the oxide growth too.

3) Developing a finite element model of ring test to assess the interfacial friction between the ingot and die during open-die forging. The variation in the internal diameter of rings is an indication of friction. The formation of oxide layers and their effect on friction should be comprehensively evaluated. Identifying different oxide layers and the mechanical properties of each layer is crucial for developing the finite element model. The outcomes of this objective can help the industrial partner to predict the frictional conditions and avoid die wear.

CHAPTER 2

INFLUENCE OF NICKEL ON HIGH TEMPERATURE OXIDATION AND CHARACTERISTICS OF OXIDE LAYERS IN TWO HIGH STRENGTH STEELS

Ali Vedaei-Sabegh[1], Mohammad Jahazi[1], Jean-Benoît Morin[2]

[1] École de Technologie Supérieure, Department of Mechanical Engineering, 1100 Notre-Dame Street West, Montreal, QC, H3C 1K3, Canada.
[2] Finkl Steel Inc., 100 McCarthy, Saint-Joseph-de-Sorel, QC, J3R 3M8, Canada

Abstract

The oxidation behaviors of two high strength medium carbon steels with different Ni concentrations were investigated by means of differential thermal analysis equipped with thermogravimetry. Four different oxidation temperatures, and five oxidation times were tested. A parabolic behavior was observed for the oxide growth in both alloys; however, the relative increases in the oxidation rate from one temperature to another were not similar for both alloys and the oxidation kinetics of the Ni rich steel were significantly lower than those of the low Ni alloy. On the basis of the thermogravimetry results, the activation energy for the oxidation of the two alloys were determined. The influence of Ni content on the microstructure and characteristics of the different oxide layers was studied using a combination of laser confocal microscopy, electron microscopy and X-ray diffraction (XRD) analysis. The results revealed a clear influence of Ni on the nature and relative presence of different oxide layers. The results are interpreted in terms of the influence of Ni on the diffusion of oxygen through the oxide layer.

Keywords: High temperature oxidation, Oxidation kinetics, XRD analysis, EDS analysis

2.1   Introduction

High temperature oxidation during heat treatment or forming operations is an inevitable phenomenon for the majority of steels. Thermally grown oxides on substrates cause material waste and surface damage that could significantly affect surface quality and integrity, resulting in reduced service properties of the component (Utsunomiya et al., 2009). During hot forming operations, such as forging of large size ingots, thermally grown oxides detach and can indent the material and cause large size cracks which could even result in scrapping of the part. The oxide layer also causes premature tool wear by affecting the friction and heat transfer between the forged ingot and the die. However, the significance of the above defects varies with minor variations in the alloy composition or process parameters. Hence it is important to quantify the influence of changes in chemical composition as well as process parameters on the kinetics of oxide growth and develop a better understanding of the underlying mechanisms (Utsunomiya et al., 2009; Yu et al., 2015).

Oxidation in carbon steels initiates by discrete nuclei, which expand laterally to join adjacent oxides. When these nuclei reach each other, the oxidation proceeds by mass transfer of ions in a direction normal to the surface (Munther & Lenard, 1999). The growth of scale depends on diffusion of cations (Fe^{2+} and Fe^{3+}) or anions (O_2^-). In this regard, during the oxidation process, the Fe cations diffuse outward through the oxide and reach to its top surface, where in contact with the air, the chemical equilibrium is established at the interfaces of gas-oxide and oxide-metal. Diffusion of Fe cations in steel oxide is faster compared to that of oxygen (Suarez et al., 2009; Vijh, 1974; Wakasa & Yamaki, 1988). Hence, the diffusivity of Fe in oxide and concentration of vacancies determines the kinetics of oxide growth. Temperature and time are two determinative factors that could increase the diffusivity of Fe and consequently the growth rate of oxide layers (H Abuluwefa et al., 1996; Munther & Lenard, 1999; Vijh, 1974).

Generally, the oxide crust of pure iron comprises of three layers: Wustite (FeO), the closest layer to the base metal, an intermediate layer, magnetite (Fe_3O_4), followed by hematite (Fe_2O_3) layer at the outermost. In general, the thickness ratios of these layers are reported to be 95:4:1

for wustite, magnetite and hematite, respectively (Suarez et al., 2009; Zambrano et al., 2015). Considering the phase ratio of wustite to other layers, it could be concluded that Fe has higher diffusivity in the wustite (Suarez et al., 2009; Zambrano et al., 2015), whose composition has been described as $Fe_{1-x}O$, where X could be in the range of 0.04 to 0.17. Wustite is known to have low hardness and acts as lubricant at high temperature. In contrast, magnetite shows higher hardness, whereas hematite causes severe wear on contacting surfaces by its high hardness. These characteristics could vary with respect to chemical composition of the base metal, oxidizing atmosphere, pressure, temperature and time (R. Chen & Yuen, 2000; Zambrano et al., 2015). Chen and Yuen (R. Chen & Yeun, 2003) reported that, the growth rate of oxide layer during isothermal heat treatment of a mild steel and pure iron, showed a parabolic behaviour with respect to the oxidation time for temperature range of 700 to 1100 °C in different atmospheres including oxygen and air. Liu et al. (Liu et al., 2013) reported that increasing oxidation temperature and time increased the thickness fraction of wustite and decreased that of magnetite, but had negligible effect on hematite for micro-alloyed steel in temperature range of 900 to 1200 °C in mixture gases of ($80\%N_2$–$15\%CO_2$–$5\%O_2$) to simulate the reheat furnace. It has been reported that for pure iron, the initial oxidation rate in short times is determined by the chemical reactions between oxygen atoms at the surface of the metal and adsorbed oxidizing species (H Abuluwefa et al., 1996). On the other hand, the diffusion of ionic species, such as oxygen, throughout the oxide layers is the rate controlling factor for the above phases (H Abuluwefa et al., 1996; Cao et al., 2014).

While it has been reported that the growth rate of hematite depends on oxygen diffusion due to the abundance of oxygen close to the surface, that of wustite and magnetite mainly depends on the diffusion of cations, since they are closer to the base metal (Basabe & Szpunar, 2006; Cao et al., 2014). However, the growth mechanism for each of these three layers is still not well documented (Baud, Ferrier, & Manenc, 1978; Cao et al., 2014). As each layer demonstrates specific characteristics and tribological behaviours, their distinctive evaluation is essential.

Considering the oxidation kinetics, oxidation atmosphere and chemical composition of the alloy could remarkably affect the oxidation process: Abuluwefa et al. (H Abuluwefa et al., 1996; HT Abuluwefa, Guthrie, & Ajersch, 1997) reported that the oxidation of a low carbon steel in carbon dioxide and water vapour, in temperature range of 800 to 1150 °C, comprised of a single wustite layer; whereas all three layers were present when oxidized in a pure oxygen atmosphere. Yun et al. (Yun et al., 2013) showed that for oxidation of a low carbon steel at 500 °C, wustite was not detected, whereas wustite was dominant layer for oxidation at 700 °C. Also, Yun et al. (Yun et al., 2013) acquired higher oxygen rate for oxygen containing water vapor compared to those in dry gases. Carbon is the most important alloying element influencing the oxidation kinetics (Kumari, Vaidyan, & Sathyanarayana, 1991). It could have an accelerating effect on the oxidation rate or reducing it (R. Chen & Yeun, 2003; C. Wang & Duh, 1988), depending on the oxidation conditions (Kao & Wan, 1988). Krzyzanowski et al. (Krzyzanowski & Beynon, 2006) and Von Fraunhofer et al. (Von Fraunhofer & Pickup, 1970) reported that aluminium (Al) can increase the wustite formation temperature and therefore, increase the oxidation resistance of steel. Rahmel et al. (Rahmel et al., 1995) and C. H. kao (Kao & Wan, 1988) reported that the formation of a α-Al_2O_3 during the oxidation process provides the high-temperature oxidation resistance (Kao & Wan, 1988). Webler et al. (B. A. Webler & Sridhar, 2007) and Asai et al. (Asai et al., 1997) showed that Si can decrease oxidation and also roughen the oxide-metal interface. Li et al. (Z. F. Li, Cao, He, Liu, & Wang, 2016) demonstrated that for oxidation of low carbon steel at 1050 °C in dry and wet air, adding the Cr element will significantly decrease the oxidation rate by forming Cr_2O_3 and $FeCr_2O_4$ layers. Krzyzanowski et al. (Krzyzanowski & Beynon, 2006) and Kim et al. (I. Kim et al., 2000) also found that the contribution of Cr to oxidation resistance of the steel was less than Si or Al at temperature of 500 and 700 °C. Furthermore, Takeda et al. (Takeda et al., 2010) reported the formation of $FeOCr_2O_4$ at the interface of oxide-metal for oxidation of three commercial steels, and found that it reduces the scale removability. Asai et al. (Asai et al., 1997) reported that the addition of nickel (Ni) also reduced the scale removability. Laukka et al. (Laukka, Heikkinen, & Fabritius, 2019) found that above 1225 °C in an O_2 atmosphere, oxide growth increased in presence of boron (B), but reduced by Titanium (Ti) addition.

The activation energy of oxidation can also be affected by alloying elements, oxidation temperature or time. Regarding the activation energy of elements and the contributed effects of elements on activation energy of steels, Young (Young, 2008) reported values in the order of 230 and 120 KJ.mol^{-1} for oxidation of Co in air at temperature between 800-950 °C and 950-1150 °C, respectively. In the temperature range of 980-1200 °C, an activation energy of 243 KJ.mol^{-1} was reported for oxidation of Cr in air by Young (Young, 2008). While the activation energy of wustite in oxidation of AISI 1018 steel was reported as 120 KJ.mol^{-1} by Munther and Lenard (Munther & Lenard, 1999), Jha et al. (Jha et al., 2001) reported 178 KJ.mol^{-1} for Fe-19.2%Cr steel oxidized at 1000 °C and related it to the effect of Cr. The same authors calculated an activation energy value of 201 KJ.mol^{-1} for Fe-4%Si steel in the oxidation temperature range of 800 to 1000 °C and discussed the significant effect of Si.

In the above studies the specific effect of an element has been investigated; however, the influence of the alloying elements on the characteristics of the different steel oxide layers and the kinetics of oxide growth is still an open question (Mrowec & Grzesik, 2004). In the present study, the influence of time and temperature on the kinetics of oxide growth of two medium carbon low alloy steels with differences in Ni content was investigated. The nature, crystallography, microstructural features and evolution of the different oxide layers were characterized as a function of process variables and the role of Ni in this evolution is quantified. The results are discussed in terms of the interactions of Ni with other elements and their diffusion through the oxide layer and a mechanism is proposed that accounts for the influence of Ni on oxidation kinetics and microstructure evolution of oxide layers.

2.2   Materials and methods

The chemical composition of studied steels is given in Table 2.1, and identified as low nickel (LNi) and high nickel (HNi). The Ni content in the HNi is almost 6 times higher compared to the LNi one. Both materials were provided by Finkl steels Sorel, Quebec, Canada. Also, the chemical composition of provided samples were measured again using the Thermo Scientific ARL™ 4460 mass spectrometer for verification.

Table 2.1 Chemical composition of employed steels in current study (wt%)

	C	Mn	Si	Ni	Cr	Mo	Cu
LNi	0.35	0.99	0.41	0.5	1.86	0.53	0.16
HNi	0.35	0.99	0.41	2.92	1.86	0.53	0.16

Oxidation samples were prepared from the cast blocks. For thermogravimetric analysis (TGA) on a PerkinElmer TG/DTA 6300, samples with 4 mm of diameter and 7 mm of length were prepared using a precision cutter. Oxidation temperatures of 1000, 1100, 1150 and 1200 °C were chosen, based on the actual working temperatures in industry, to assess the mass gain of samples during 3, 10, 20, 30 and 60 min of exposure time. Samples were placed in the TG/DTA facility on an alumina pan and were heated to the oxidation temperature under 50 ml.min^{-1} flow of argon to prevent any oxidation before reaching the desired temperature. The samples were heated with the heating rates of 15, 14.37, 13.75 and 12.5 °C.min^{-1} for oxidation temperatures of 1200, 1150, 1100 and 1000 °C, respectively. The different heating rate made the samples reach to the oxidation process at the same heating time to switch the gas from argon to air. At the oxidation temperature, the flowing gas, with the same flow rate of 50 ml.min^{-1}, was switched from argon to air by a gas control unit to provide an oxidative environment (Fig. 1.1). As the chamber is filled with the gas, the sample is in full contact with argon or air. The gas control unit makes the appropriate flow rate of gas to switch it from argon to air in a short time and prevent inaccuracy. The recorded mass gain during this stage, for different oxidation time intervals and temperature, was then utilized for oxidation analysis of the two steels.
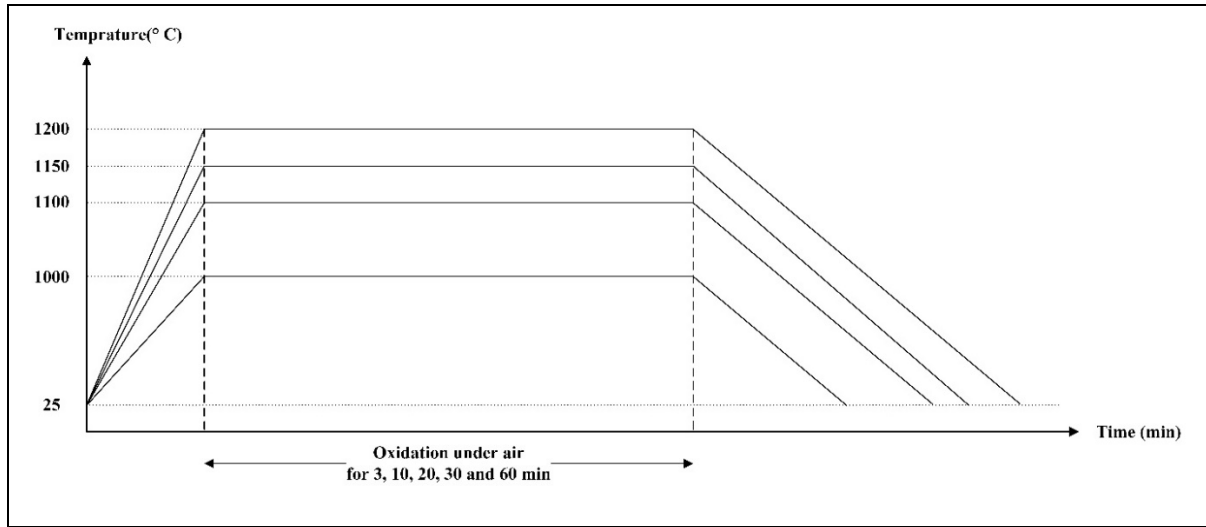
Figure 2.1 Heating cycle for thermogravimetric analysis

In order to accurately compare the severity of oxidation under different conditions, mass gain by unit surface, $\Delta W/A$, was used. Similar approaches have already been used by other authors (Pujilaksono, Jonsson, Halvarsson, Svensson, & Johansson, 2010; H. Yin, Chan, Yuen, & Young, 2012; Yuan, Wu, et al., 2013). In the above ratio, ΔW represents the mass gain (g) and A is the surface of sample (cm^2).

Since the TGA/DTA samples were too small for XRD evaluations and SEM microscopy, another set of samples in the form of rectangular cubes of $10 \times 10 \times 20$ mm were prepared and subjected to the same oxidation temperature and time conditions. The oxidation tests were carried out using a material testing system machine (MTS) equipped with a radiative furnace, ChamberIR E4 elliptical chamber heater, as shown in Fig. 2.2. This chamber has four elliptical polished aluminium reflectors that focus the supplied infrared energy in the heater centre axis. Samples were heated to the oxidation temperature under argon protection, followed by switching the gas flow to air for desired oxidation time. After the oxidation test, the samples were cooled down to room temperature while reintroducing the protective argon gas in order to avoid possible oxidation during cooling. The furnace temperature was controlled through a PID controller which provided temperature variations of ± 3 °C. Temperature measurements were made employing K-type thermocouples. In addition to the furnace thermocouple, two

others were placed on opposite faces of the samples to validate that the heating and cooling profiles were identical all around the sample. Prior to oxidation tests, samples were grounded using 320 mesh SiC papers to produce similar surface roughness. All the samples were ultrasonically cleaned for 15 min in distilled water and ethanol and kept in a vacuum chamber before conducting oxidation tests.

Figure 2.2 MTS machine with an installed radiative furnace

To evaluate the oxide phases by XRD, the oxide layers were removed from the samples and powdered in a mortar. The powdered oxides were analysed employing a PANalytical X-ray diffractometer with Cobalt K_α radiation, scanned angles from 20° to 100°, step size of 0.033°, generator voltage of 45 kV and a tube current of 40 A. In order to avoid any peak overlap from the powder holder, a blank test was conducted, which showed no peak superimposition with the oxide ones. Microstructural investigations were conducted using a LEXT OLS4100 laser confocal microscope and a Hitachi SU-8230 Field Emission-STEM equipped with a X-flash EDS quad detector. Special care was taken to protect and conserve the integrity of the oxide layer during sample preparation for microscopic examinations. Specifically, a special cold mounting copper-based powder was used to provide high conductivity and minimum manipulation. For this purpose, the oxide layers were preserved in the copper cold mount and then cross sectioned by a diamond blade for microscopic imaging. The mounted samples were

grounded to 800 mesh on SiC papers and were polished on a Buehler vibrometer polisher for 6 hours in a 0.05 μm colloidal silica suspension to provide smooth surface finish.

2.3   Results and discussion

2.3.1   Effect of Ni on the kinetics of oxide growth

Fig. 2.3 illustrates the squared mass gain per unit surface for LNi (Fig. 2.3 a-d) and HNi (Fig. 2.3 e-h) steels. The results indicate that the weight gain of both steels increased with the oxidation temperature or oxidation time. In all cases, for all testing temperatures, oxidation for 3 min is remarkably less than other oxidation times. The remarkable lower results for this oxidation time could be contributed to the relation of oxidation to square root of time, where there was not sufficient time for diffusion of oxygen.

(a)   (b)
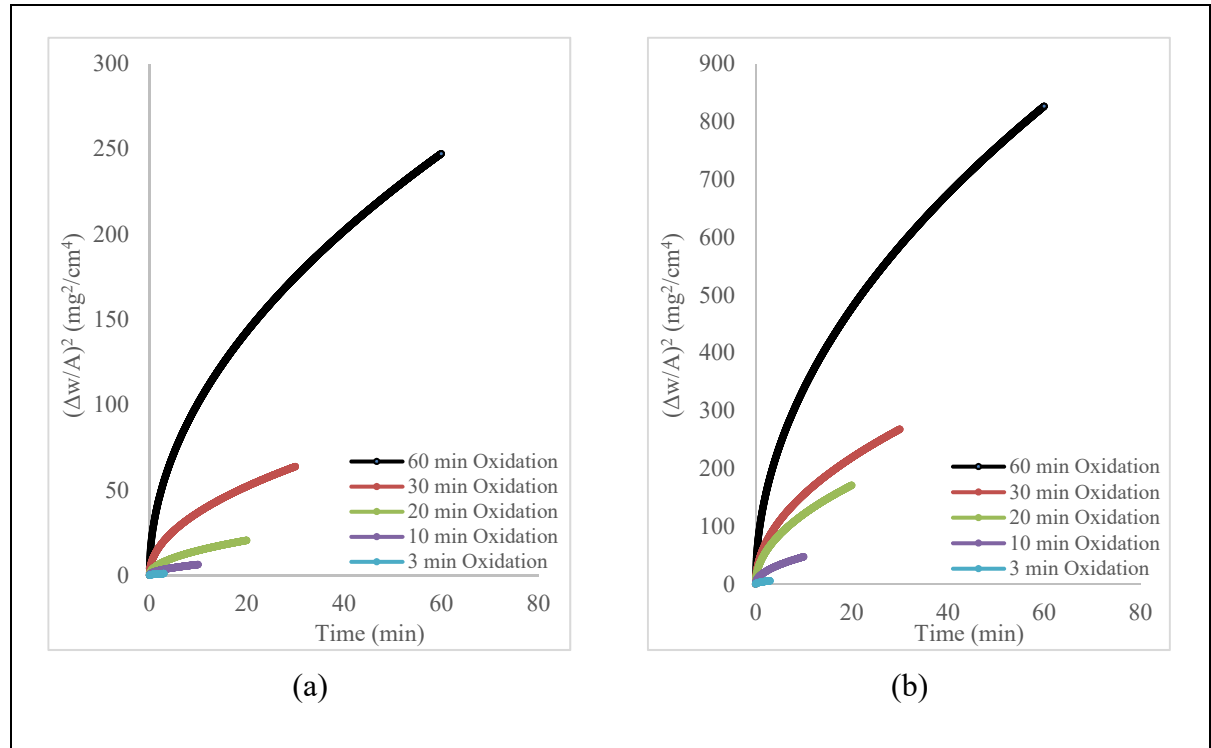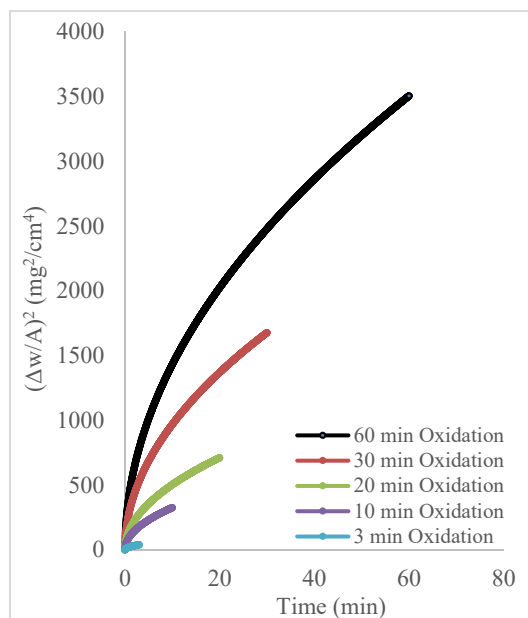
(c)
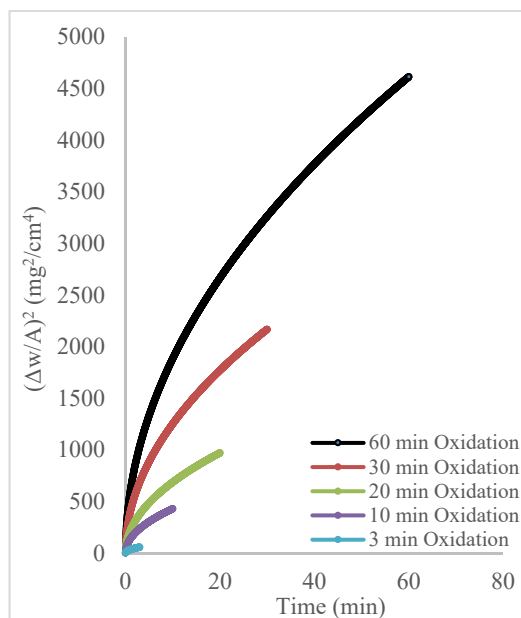
(d)
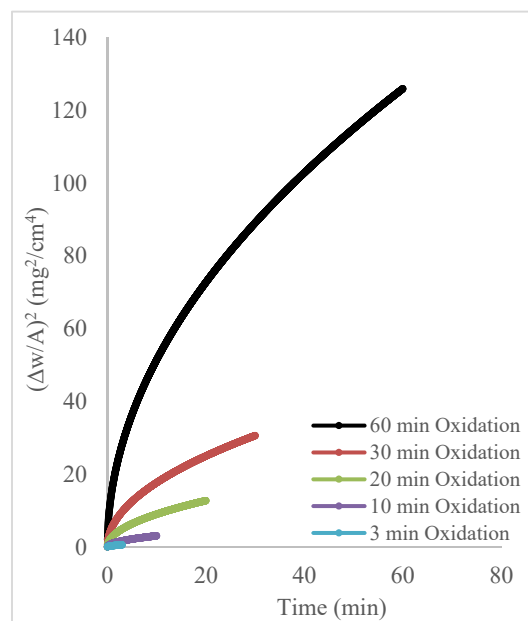
(e)
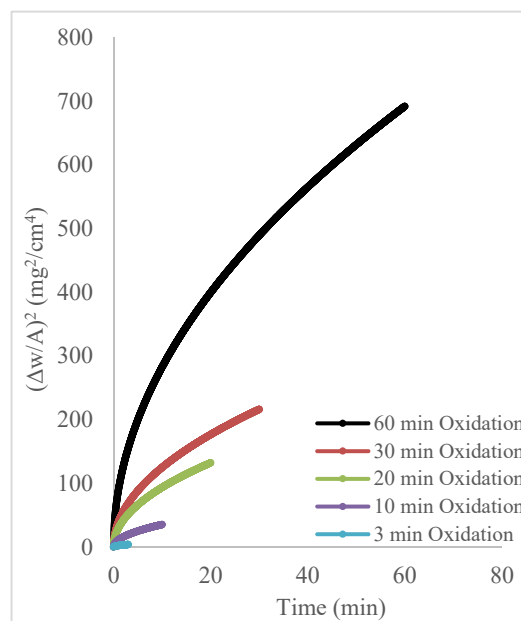
(f)
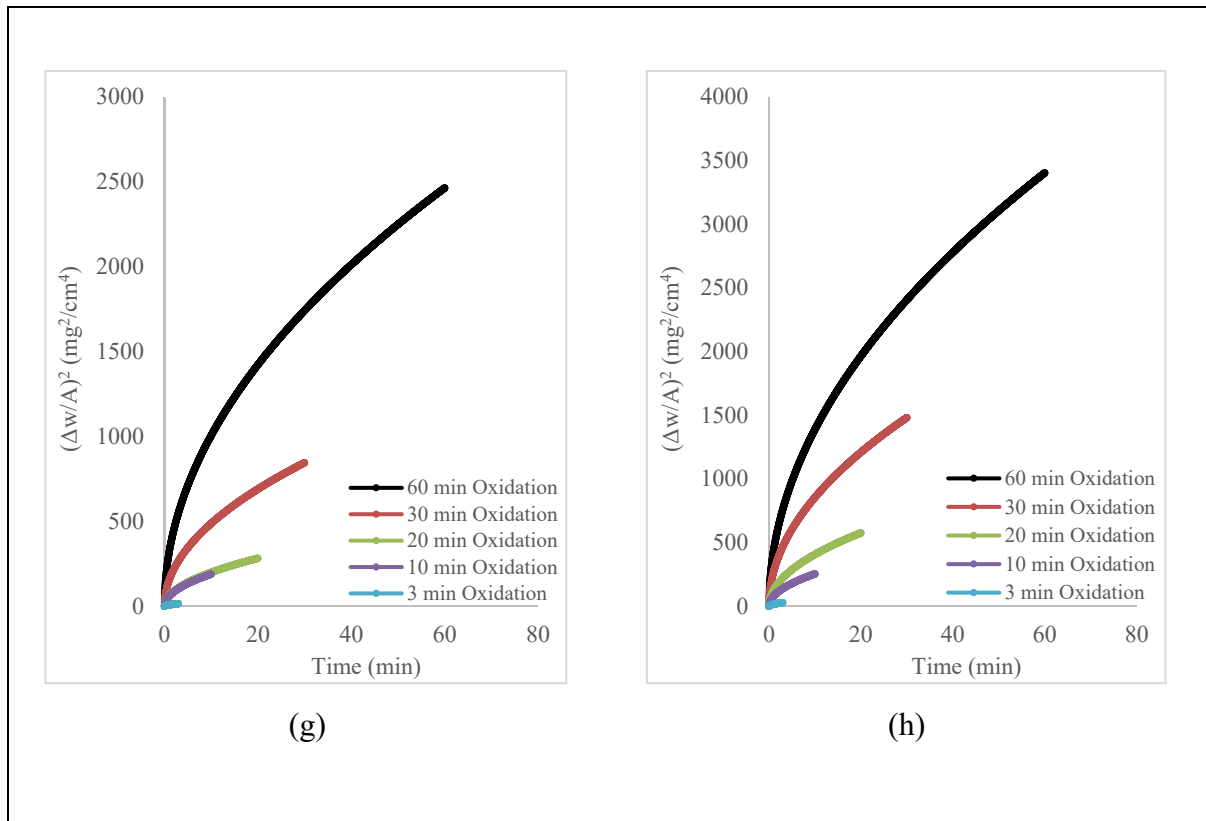
Figure 2.3 Squared mass gain per unit surface for oxidation of LNi at: a) 1000 °C, b) 1100 °C, c) 1150 °C and d) 1200 °C; and HNi at: e) 1000 °C, f) 1100 °C, g) 1150 °C and h) 1200 °C

For each oxidation temperature, by increasing the oxidation time, the oxidation rate decreases. For instance, by increasing the oxidation time from 10 to 30 min, the squared weight gain per unit surface at 1100 °C increased from 47.3 to 267.2 (mg2.cm-4). For the same oxidation temperature, by increasing the oxidation time from 30 to 60 min, the squared weight gain per unit surface increased to 825.9 (mg2.cm-4), about triple. This phenomenon becomes more significant as the temperature increased to 1150 and 1200 °C. For example, at 1200 °C, the squared weight gain per unit surface increased about 416% in the oxidation time interval of 10 to 30 min, whereas it only increased by about 115% in the 30 to 60 min interval. The decreasing tendency of the oxidation rate with time was observed for all studied oxidation temperatures.

The kinetics of oxide growth at the surface of pure iron was studied by Yuan et al. (Yuan, Wu, et al., 2013) who assessed two approaches for analysing mass gain by unit surface for oxidation in oxygen and steam atmospheres, as follows:

$$\left(\frac{\Delta W}{A}\right)^2 = k_p.t \qquad\qquad \text{Parabolic rate kinetics} \qquad\qquad (2.1)$$

$$\left(\frac{\Delta W}{A}\right) = k_l.t \qquad\qquad \text{Linear rate kinetics} \qquad\qquad (2.2)$$

where $\Delta W/A$ is the mass gain per unit area (g.cm^{-2}), t oxidation time (s), k_p the parabolic rate constant (g^2.cm^{-4}.s^{-1}) and k_l is the linear rate constant (g.cm^{-2}.s^{-1}). The authors found that oxidation of iron in oxygen follows the parabolic kinetics behaviour. The results obtained in the present work are also in agreement with those of Yuan et al. (Yuan, Wu, et al., 2013), in terms of parabolic oxidation rate pattern.

The observed behaviour could be related to the fact that solid-state diffusion is the rate controlling factor in the oxidation process. In the initial stages of oxidation, the steel surface is free from oxide layers and therefore the oxide growth would be significantly faster compared to later oxidation times. However, as the oxidation proceeds, the newly formed oxide layers act as barriers to oxygen diffusion and in order to continue the oxidation, oxygen should pass through the oxide layer to reach Fe (instead of direct contact with Fe), which will slow down the oxidation (Bradley, Barr, & Youtsey, 1979; Nagl & Evans, 1993). Thus, the increase in the oxide layer thickness after the initial stage will depend on the ease of diffusion for oxygen and Fe through the oxide layers. It is interesting to note that the results for oxidation time intervals of 10 and 20 min are close, whereas oxidation for 60 min results in significantly thicker oxide layer than other oxidation times.

The faster oxidation rate in the initial stages is in accordance with parabolic growth rate of oxide thickness (Birks et al., 2006; R. Chen & Yeun, 2003; Suárez et al., 2008):

$$h = \sqrt{k.t} \qquad\qquad\qquad (2.3)$$

In the equation above, h, k, and t are oxide thickness (cm), parabolic growth rate (cm²s⁻¹), and time (s), respectively. Fig. 2.3 shows that the oxidation of HNi steel is significantly lower than LNi, under similar conditions. The only different alloying element between the two steels, Ni, is the element which could be the reason for the observed behaviour. On the basis of the results presented in Fig. 2.3 and equation 2.4, the activation energy (EA), was determined for the two steels from the slope of the curve (ln k_p/k_0-1/RT) as reported in Fig. 2.4 (Suarez et al., 2009; Young, 2008):

$$k_p = k_0 exp\left(-\frac{E_A}{RT}\right)$$

(2.4)

k_p, k_0 are parabolic oxidation kinetic constants (g².cm⁻⁴.s⁻¹), E_A is the activation energy for the oxidation (J.mol⁻¹), R is the gas constant (8.314 J.mol⁻¹.K⁻¹) and T is the absolute temperature (K). The activation energies for LNi and HNi steels are 238 and 275 kJ.mol⁻¹, respectively. The higher activation energy value for the HNi steel is indicative of its higher resistance to thermal oxidation.
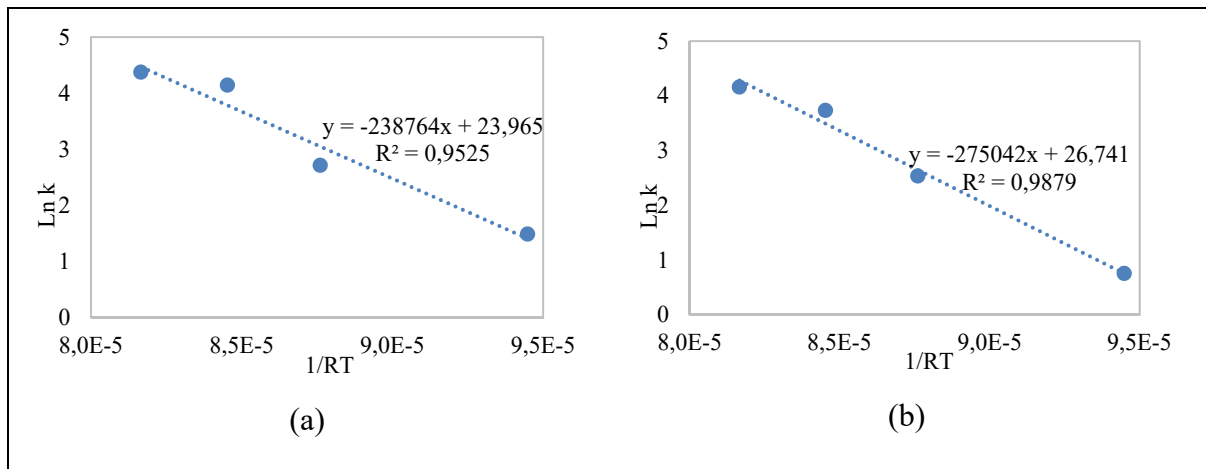
Figure 2.4 Activation energies for oxidation of: a) LNi and b) HNi steels

A comparison between the activation energies obtained in this present study and those reported in the literature (Table 2.2) shows good agreement with some studies, while significant

differences are observed with others. This difference could be attributed to complexity of oxidation by different alloying elements, different oxidation temperature and oxidation environment (R. Chen & Yeun, 2003; R. Chen & Yuen, 2005a).

For example, Chen and Yuen reported activation energy value of about 157 kJ.mol^{-1} for oxidation of iron in temperature range 700–1250 °C (R. Chen & Yeun, 2003). Liu et al. (Liu et al., 2013) obtained an activation energy of 105 KJ.mol^{-1} for a micro-alloyed steel oxidized at 1200 °C, while Munther and Lenard (Munther & Lenard, 1999) using AISI 1018 steel, which has higher C, but lower amounts of Ni, Mn, Si, Cr and Mo, reported an activation energy value of 120 KJ.mol^{-1} at the same temperature.

Table 2.2 Chemical composition of employed steels in former studies
for activation energy of oxidation (wt%)

	Activation energy (KJ.mol^{-1})	C	Ni	Mn	Si	Cr	Mo
Yuan et al. (Yuan, Wu, et al., 2013)	205	0.011	0.018	0.035	0.028	0.01	0.005
Abuluwefa et al. (H Abuluwefa et al., 1996)	127±7	0.04	0.03	0.2	0.02	0.04	0.01
Liu et al. (Liu et al., 2013)	105	0.04	0.02	1.56	0.23	0.02	0.17
Munther and Lenard *(Munther & Lenard, 1999)*	124	0.18	-	0.71	0.21	-	-
Madern et al. (Madern, Monnier, Baddour-Hadjean, Steckmeyer, & Joubert, 2018)	280	0.4	33.5	1.5	1.6	5	-
Present Study (LNi)	238	0.35	0.5	0.99	0.41	1.86	0.53
Present Study (HNi)	275	0.35	2.92	0.99	0.41	1.86	0.53

For oxidation of Ni in air, Young (Young, 2008) reported the activation energies of 120 and 240 KJ.mol^{-1} at temperature ranges of 600-1100 °C and 1100-1400 °C, respectively.

The above results show a clear influence of Ni on the kinetics of oxidation and its activation energy; however, the impact of a higher Ni content on the characteristics of the oxide layers is still not well documented. Hence, in the following section the characteristics of oxide layers will be studied.

2.3.2   Effect of Ni on the characteristics of oxide layers

Fig. 2.5 provides an illustrative example of the three oxide sub-layers obtained from LNi and HNi steel samples oxidized at 1000 °C for 60 min (images obtained using the LEXT OLS4100 laser confocal microscope).

(d)
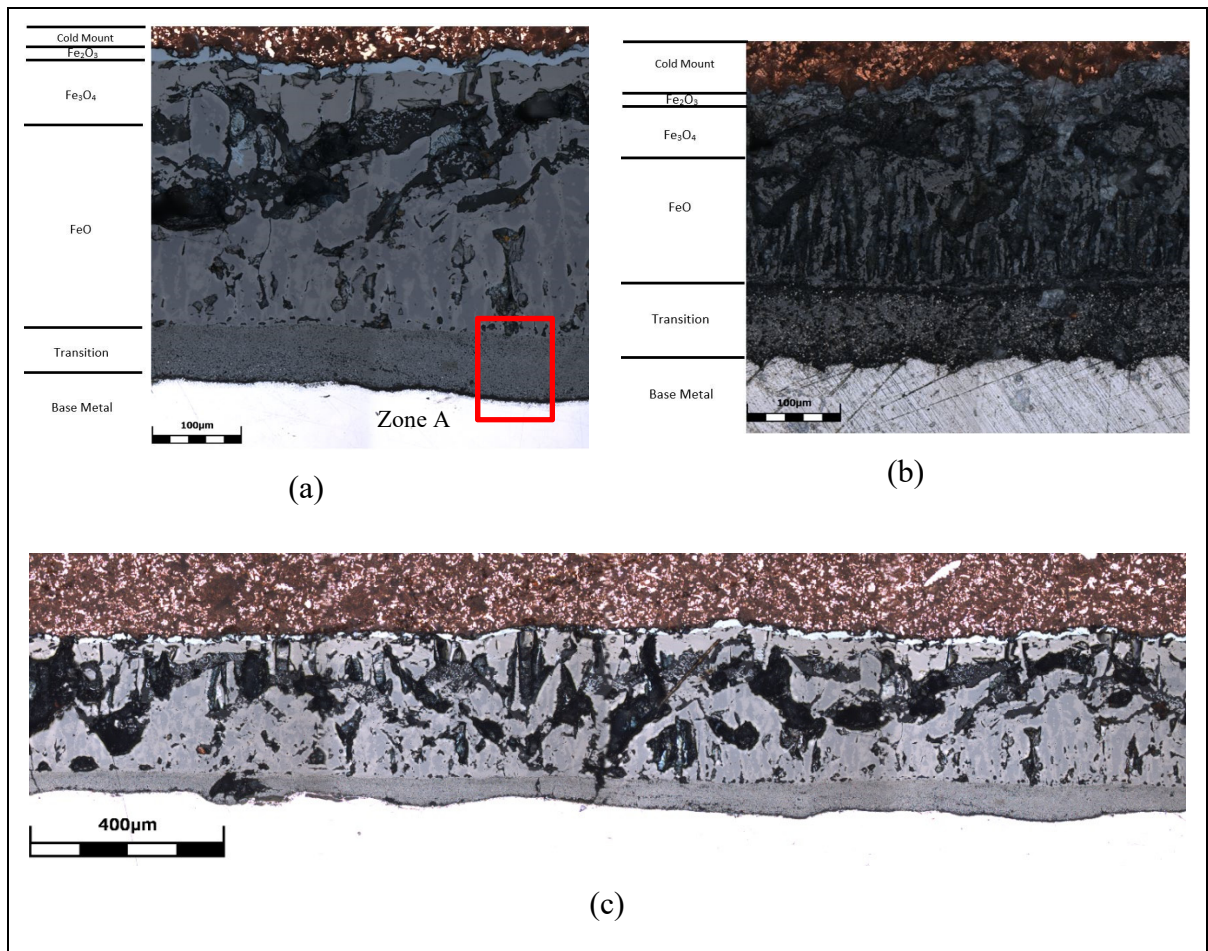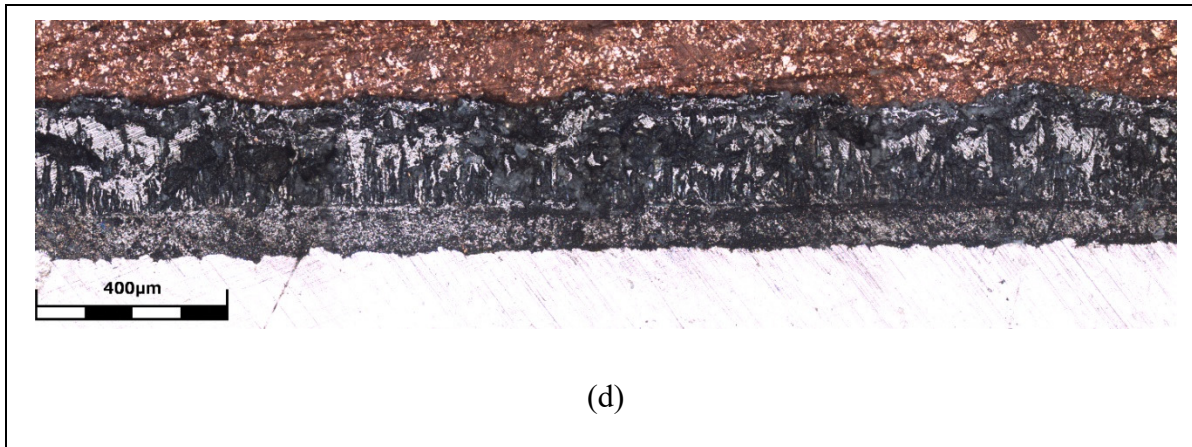
Figure 2.5 LEXT laser confocal image from oxide layers of sample oxidized at 1000 °C for 60 min: a) LNi, b) HNi, c) Stitched image of LNi and d) Stitched image of HNi

As shown in Fig. 2.5, the overall thickness of the oxide layer in the LNi steel was in average 14.7% higher than the one in the HNi steel under similar testing conditions. Specifically, the thickness of the wustite on LNi was 160.2 μm, while in the HNi it was 139.6 μm. Similarly, the thicknesses of the magnetite were 85.6 and 74.6 μm and those of hematite are 30.4 and 26.5 μm for LNi and HNi steels, respectively. In both steels, the fractions of wustite, magnetite and hematite to overall oxide thickness, are 58%, 31% and 11%, respectively. Hence, despite the reduction of oxidation by higher amounts of Ni, in relative terms the overall fraction of each layer to oxide thickness remained consistent. However, in absolute terms, the lower thickness of oxide layer in the HNi has resulted in lower, material loss due to oxidation and less die wear because of lower amount of hematite. This is in accordance with the study of Barrau et al. (Barrau et al., 2003) on friction and wear tools for forging.

While the cross section of the oxide for LNi steel is porous and rough, that of the HNi is smoother and continuous with few visible porosities as shown in Fig. 2.5. Furthermore, compared to LNi samples, the oxide - metal interface is rougher in the case of HNi steel, which leads to longer interface. Finally, it must be noted that a thicker transition layer was observed in the HNi steel, which makes additional bond between oxide and metal (see Fig. 2.5). The above phenomena are expected to decrease the scale removability for HNi and therefore if not

properly removed from the surface, oxide could penetrate during forging into the base metal and cause cracking and material waste.

(a)

(b)
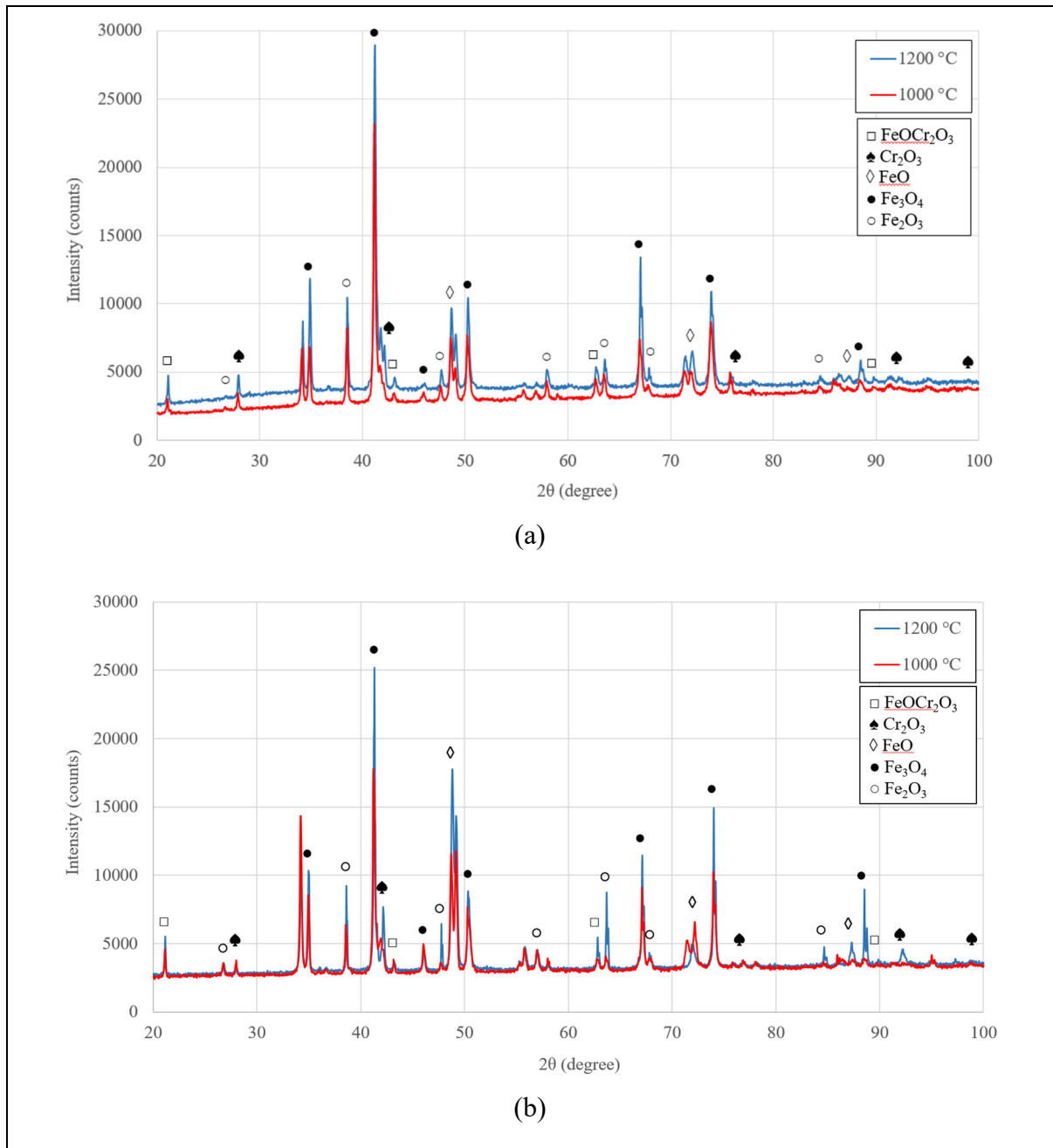
Figure 2.6 XRD analysis of LNi steel oxide powder for
oxidation time intervals of: a) 10 and b) 60 min

As reported by former studies, the oxide layers are affected by both oxidation time and temperature (Falk-Windisch, Svensson, & Froitzheim, 2015; Suarez et al., 2009; Zambrano et al., 2015). Hence, to quantify such influence in the present study, XRD analyses were conducted. To this end, two temperatures of 1000 and 1200 °C and oxidation times of 10 and 60 min were selected with the view to produce the maximum and minimum oxidation effects. The separated and powdered oxide layers were analysed and the results are provided in Figs. 2.6 and 2.7, for LNi and HNi steels, respectively.

As shown, while the three oxide layers could be identified, at a certain oxidation time for LNi, by increasing the oxidation temperature, the amount of magnetite would increase in opposition to that of hematite. Considering that hematite has a rougher surface compared to magnetite, a higher amount of it would cause the sample look darker (Liu et al., 2013). In contrast, for HNi samples, where more magnetite is present in the oxide layer, the surface of sample looks brighter and with smoother surface, as shown in Fig. 2.8. It is also interesting to note that, in addition to the representative peaks of wustite, magnetite, and hematite, the presence of spinel and chromite phases were detected in both steels that are in accordance with former studies (Falk-Windisch et al., 2015). The effects of spinel and chromite phases will be discussed in detail afterwards.

Regarding the oxidized samples at 1200 °C in Fig. 2.8, some swollen lumps could be seen. These lumps, known as blisters, are due to a combination of generated stresses during scale formation and accumulation of CO and CO2 gas at the steel - oxide interface according to following reactions (L. Chen et al., 2018; Nagl & Evans, 1993):

$$FeO + C = Fe + CO \qquad\qquad (2.5)$$

$$2FeO + C = 2Fe + CO_2 \qquad\qquad (2.6)$$
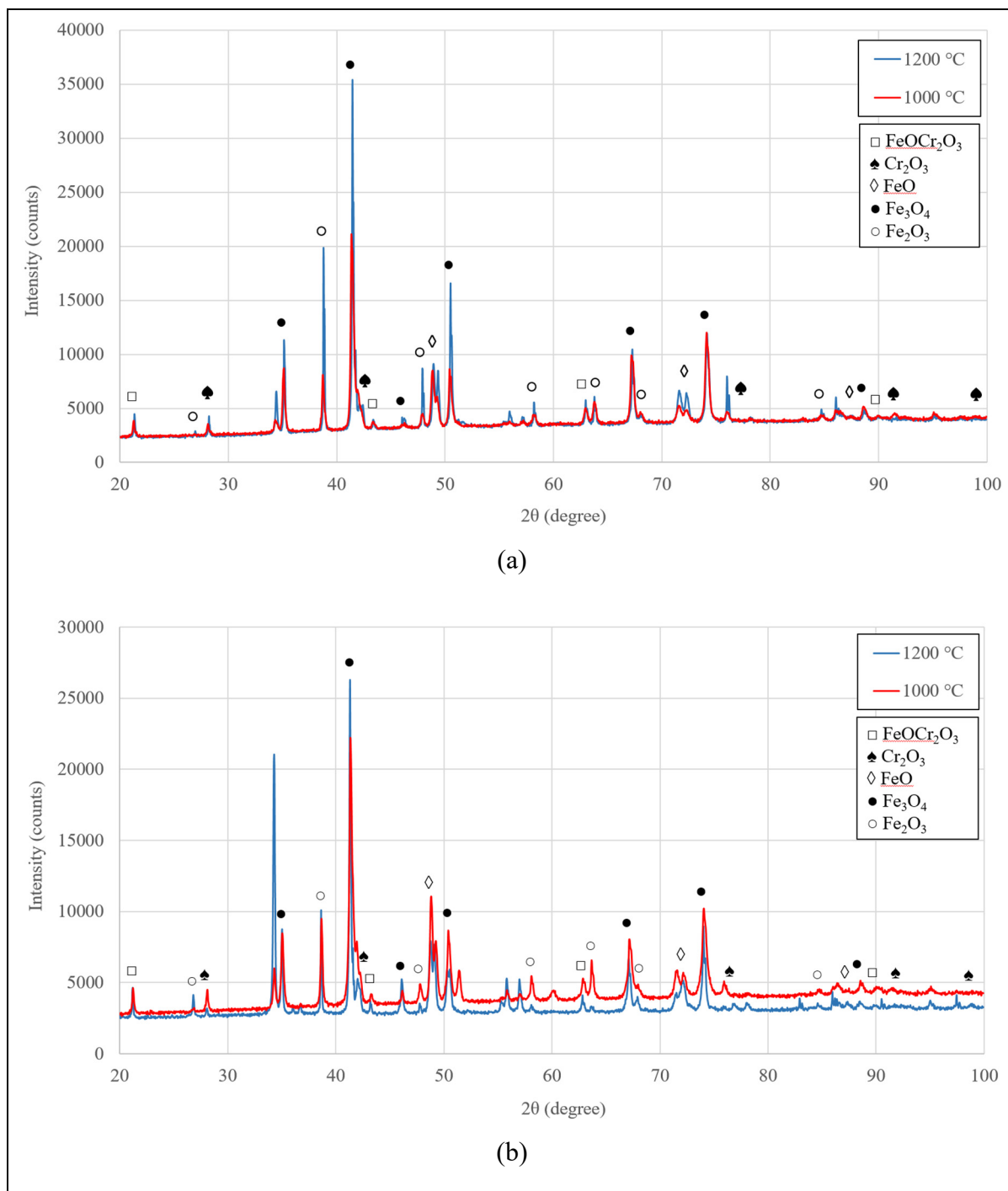
Figure 2.7 XRD analysis of HNi steel oxide powder for
oxidation time intervals of: a) 10 and b) 60 min
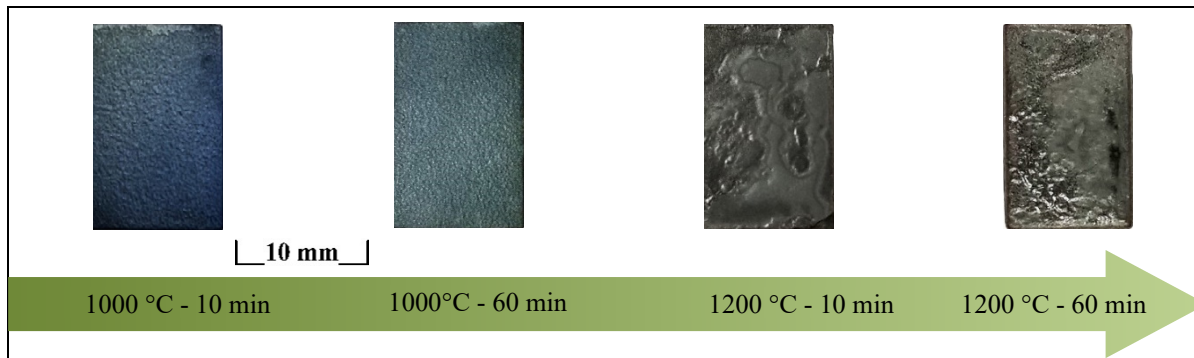
Figure 2.8 Surfaces of HNi samples oxidized at 1000 °C and 1200 °C for 10 and 60 min

2.3.3   Role of Ni on compositional evolution of the oxide layers

The effect of Ni content on the oxidation behaviour was studied in detail using Energy-dispersive X-ray spectroscopy (EDS). Fig. 2.9 shows the elemental map obtained for O and Ni for HNi steel. One of the evident differences between the two steels is the presence of a Ni rich band on the top zone of transition layer in HNi steel. A Cr rich layer is present in the vicinity of the wustite zone for both alloys (see Fig. 2.13-b). The Cr concentration gradually decreases towards the base metal. Using the XRD analysis results reported in Figs. 2.6 and 2.7, the presence of spinel and Cr_2O_3 phases peaks could be inferred. Since the spinel composition is $FeOCr_2O_3$, it could be expected that this layer is placed between wustite and Cr_2O_3 phases (L. Chen et al., 2018; Falk-Windisch et al., 2015; Yuan, Wu, et al., 2013). It should be also noted that Cr_2O_3 layer shows a decreasing gradient toward the base metal. However, as given in Fig. 2.10, the thickness of the Cr_2O_3 layer is thinner in the HNi steel (about 12 μm in LNi and about 4 μm in HNi). From the Ni elemental map, shown in Fig. 2.10, it can be seen that the Ni rich layer and the spinel phases are placed in the same region in the HNi alloy. Therefore, it appears that the formation of the Ni rich layer between the spinel and the Cr_2O_3, results in a thinner Cr rich layer.

The oxygen elemental map for HNi, oxidized at 1200 °C for 10 min, is shown in Fig. 2.9-a. The presence of an oxygen concentration gradient from the top oxide layer to the lower one is

visible in this figure Line scan analysis allowed for precise identification of the boundaries between the different layers, as well as the higher amount of oxygen for magnetite and hematite as compared to wustite as shown in Fig. 2.9-b.
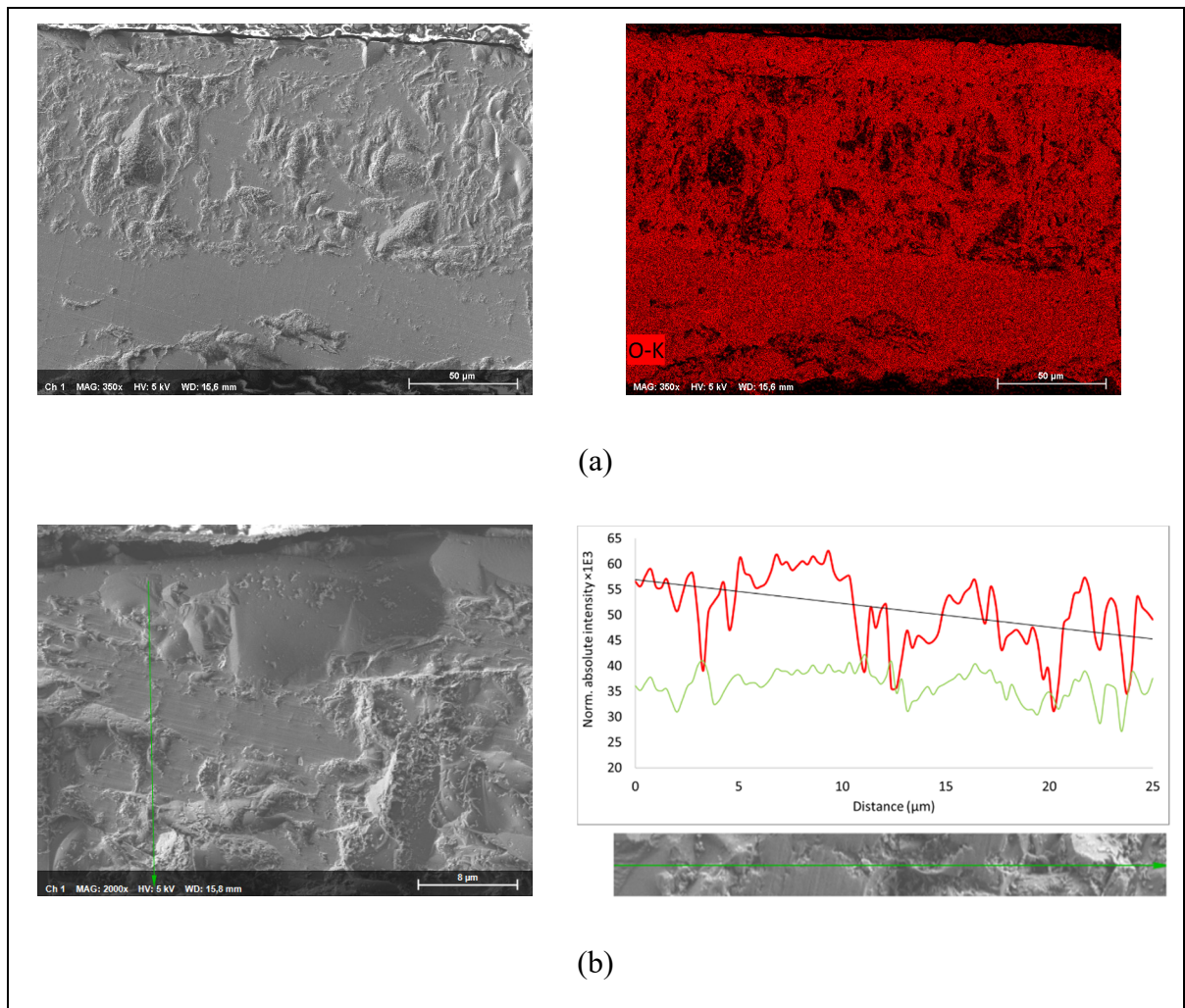
Figure 2.9 HNi steel, oxidized at 1200 °C for 10min: a) oxygen elemental map, and b) oxygen line analysis (red line), (green line is the variation of Fe element)

Elemental map analysis of Ni at the interface of base metal - wustite (zone A in Fig. 2.5-a) showed that this zone is richer in Ni than the base metal. This enrichment, as shown in Fig. 2.10-a, is probably due to the fact that Ni is more noble than iron and therefore it accumulates at the oxide-metal interface (Tsao, Yeh, Kuo, & Murakami, 2016). As will be

shown below, the diffusion of Ni in iron is very slow and as a result, it could not diffuse back rapidly to iron and will concentrate at the oxide-metal interface. The above observations are in support of those by other researchers who reported that the Ni enrichment at the interface for Fe-1 wt% Ni alloy, oxidized at 1000 °C, almost approached 70 wt% (Y. N. Chang & Wei, 1989). The higher concentration of Ni at the oxide-metal will increase the resistance to oxidation.

(a)

(b)
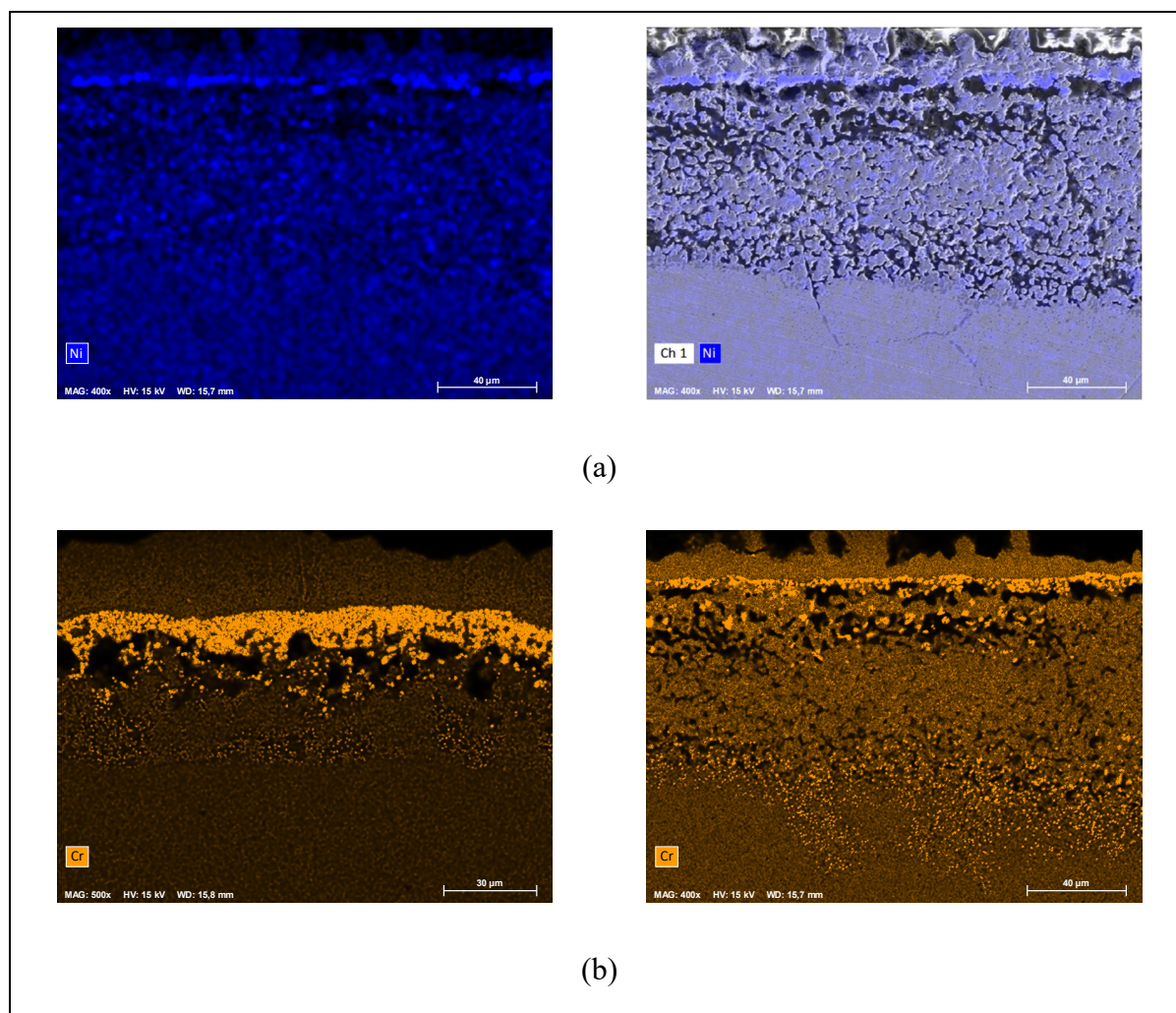
Figure 2.10 Oxidized at 1200 °C for 10min: a) Ni elemental map for HNi, and b) Cr elemental map for LNi (left) and HNi (right)

One possible operating mechanisms of Ni as oxidation barrier could be in terms of its influence on the diffusion of both oxygen and iron in the oxide layer as compared to the austenite lattice. The calculations were done at all tested temperatures; however, only those at 1200C are shown as they better illustrate the impact of Ni: Oxygen diffusion in the iron lattice was calculated based on the work published by Takada and Adachi (Takada & Adachi, 1986):

$$D = \left(2.91^{+3.40}_{-1.57}\right) \times 10^{-3}. \exp\left(\frac{-89.5}{R \times 1200}\right) \tag{2.7}$$

where D is diffusion coefficient (cm^2.sec^{-1}), R is gas constant (J.mol^{-1}.K^{-1}), and T is temperature (°K). Similarly, the diffusion of oxygen in Ni was calculated as reported by Garruchet et al. (Garruchet, Politano, Arnoux, & Vignal, 2010) and Nam et al. (Nam, Yoon, Kim, Hwang, & Lee, 2011). The results indicated that the diffusion of oxygen in iron at 1200C is about 2.88×10^{-3} (cm^2.sec^{-1}) and 4.6×10^{-6} (cm^2.sec^{-1}) in Ni, (i.e. it is almost 1000 times slower in Ni). Furthermore, Buffington et al. (Buffington, Hirano, & Cohen, 1961) reported that the self-diffusivity of iron at 1200 °C is equal to 2.8×10^{-4} (cm^2.sec^{-1}) which is almost 10^6 times faster than in Ni, 2.58×10^{-10} (cm^2.sec^{-1}) (Heuer, 1969). Consequently, a Ni rich layer will be produced that will limit the accessibility of oxygen and iron to each other and will significantly delay the oxidation process.

Fig. 2.11 shows that in the transition layer, oxygen and silicon (Si) have produced a network of particles at the grain boundaries, which could be related to the higher affinity of Si to oxygen as compared to Mn, Cr, Fe, and Ni, in accordance with the Ellingham diagram (Bhadeshia & Honeycombe, 2017). On the other hand, once the oxide is formed at the grain boundary, a Fe depleted zone would develop on both sides of the grain boundary, creating a driving force that will fuel the movement of alloying elements from grain interior toward the grain boundaries.
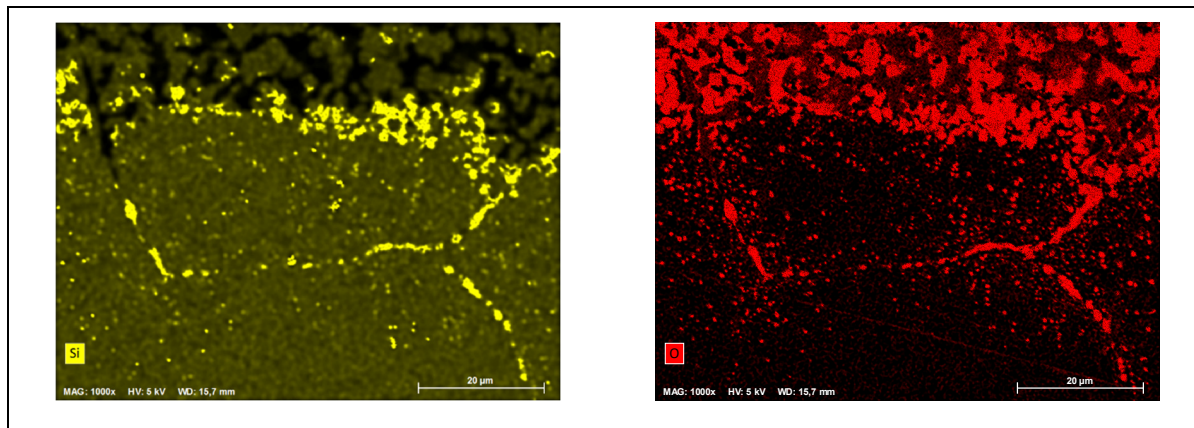
Figure 2.11 The network of particles made from oxygen and Si
in grain boundaries of HNi steel, oxidized at 1200 °C for 10min

Apart from higher thermodynamic stability of SiO_2 oxides, in terms of kinetic approach, Si has higher diffusivity in Fe compared to other alloying elements like Ni and Cr or even self-diffusion of Fe atoms (Slater, 1964). Hence, Si would produce the initial protection layer at the lower surface of the transition layer at the oxide-metal interface (Brandes, Brook, & Paufler, 1993; Buffington et al., 1961). As is demonstrated in Fig. 2.12, Mo demonstrates to segregate in the same site as of Ni in transition layer.
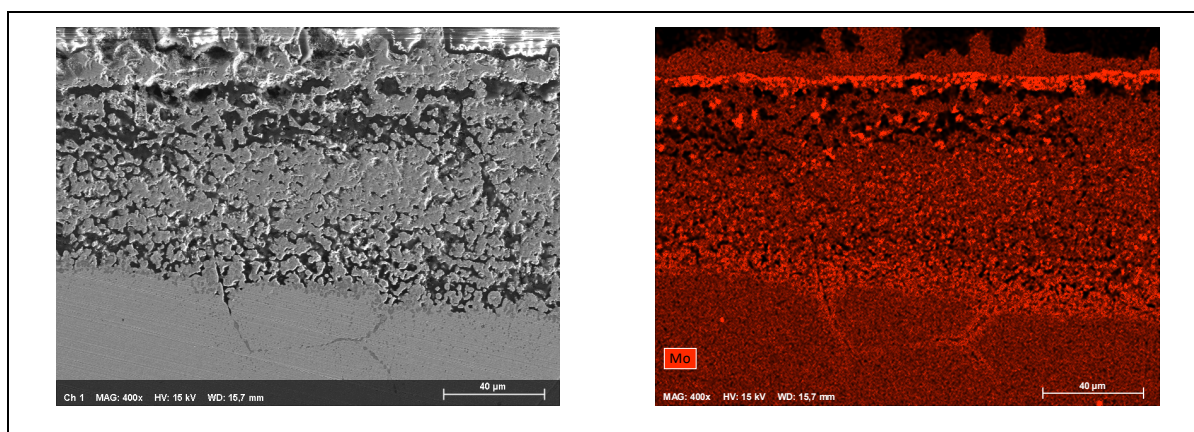
Figure 2.12 Mo segregation in transition zone of oxide of HNi steel,
oxidized at 1200 °C for 10min

The concentration of alloying element increases mainly in bulk rather than metal surface, in case that the diffusion coefficient of alloying element is higher than the oxidation rate (Krzyzanowski & Beynon, 2006). Alloying elements such as Ni or oxides such as SiO_2 and Cr_2O_3, remain in the transition zone (see Fig. 2.13). Also, Cr is rejected at scale-metal interface, making a Cr rich layer and reducing the oxidation. One of the critical factors in reducing the oxidation is the formation of Fe-Cr spinel next to base metal (Takeda et al., 2010; Yuan, Wu, et al., 2013). Furthermore, in this region, iron oxides were also detected as network of discrete grains (internal oxidation), which should be evidently in type of wustite. These grains are shown in Fig. 2.14 and related to initial stages of oxidation by former studies (Krzyzanowski et al., 2010; Yu et al., 2015).

a
b
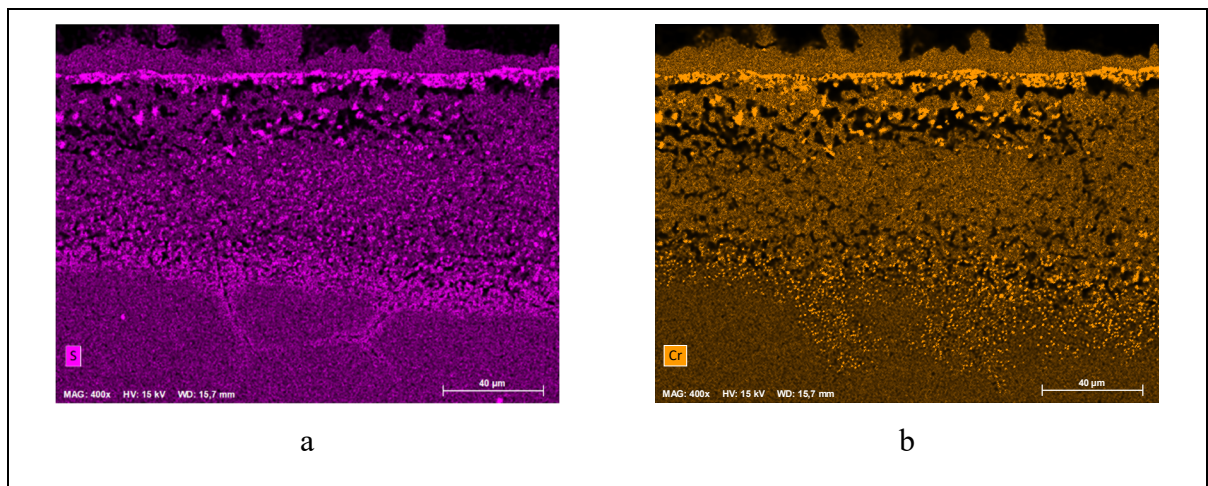
Figure 2.13 Remained a) SiO_2 and b) Cr_2O_3 oxide in transition
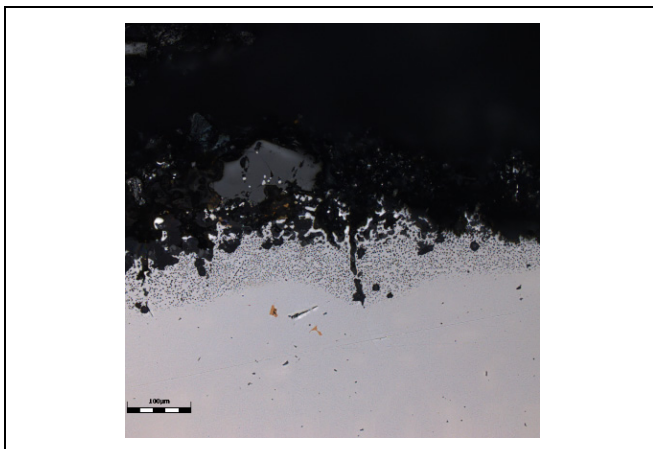
Figure 2.14 Spherical shape oxides in type of wustite
for HNi steel, oxidized at 1200 °C for 10min

Finally, it has been reported that synergistic effects may occur among different alloying elements which in some cases could significantly affect the oxidation kinectics (Tawancy, 1996). Hence, a future focus point could be the study of such synergistic effects and their impact on high temperature oxidation.

2.4   Conclusions

To investigate the effect of Ni on high temperature oxidation of steels, thermogravimetry and direct oxidation experiments were employed to oxidize two steels with different Ni concentration. The provided samples were assessed in terms of mass gain and investigated by means of SEM, EDS and XRD. The obtained outcomes are as follows:

1) By increasing the oxidation time and oxidation temperature, the oxidation rate of both LNi and HNi steels increased. The oxidation rate was increasing faster at the initial stages of oxidation, but it decreased gradually by time.

2) The oxidation of the HNi steel was less than that of the LNi steel for all tested conditions.

3) The activation energies were calculated as 238 and 275 KJ.mol^{-1} for LNi and HNi, respectively, demonstrating the higher resistance to oxidation for the steel rich in Ni.

4) The oxide layers were thinner on the HNi steel compared to the LNi, but the fraction of sub-layers to the overall oxide remained the same for both steels.

5) For oxidation at 1200 °C, blisters were observed on oxide surfaces due to generated stress during oxidation and accumulation of CO and CO_2 gas at the interface of oxide - metal.

6) The oxide - metal interface was rougher for HNi steel compared to LNi, with thicker transition layer, which would decrease the scale removability.

7) EDS analysis revealed a gradient of oxygen concentration from top oxide layer way to lower layer direction. Ni was more enriched in wustite compared to the base metal. Due to its low diffusivity, Ni was accumulated at the oxide-metal interface and made an additional bond. This bond would resist against oxidation and decrease the scale removability, as the transition layer was thicker in the HNi steel. Chromium is rejected at the interface of oxide-metal and makes a resistance against oxidation by forming a spinel layer next to base metal.

8) The spinel composition of $FeOCr_2O_3$ was placed between wustite and Cr_2O_3. The thickness of Cr_2O_3 was thinner in HNi steel. The spinel phase was placed in the same site as Ni rich layer. This issue would impede the interaction between FeO and Cr_2O_3, causing thinner Cr rich layer.

9) Considering the lower diffusivity of oxygen in Ni compared to iron lattice, and faster self-diffusivity of iron in comparison with its diffusion in Ni, a Ni rich layer would confine the accessibility of oxygen and iron to each other and consequently decrease the oxidation.

80

2.5 Acknowledgment

2.6 Data Availability

1) The raw/processed data required to reproduce these findings cannot be shared at this time due to legal or ethical reasons.

2) The raw/processed data required to reproduce these findings cannot be shared at this time as the data also forms part of an ongoing study.

CHAPTER 3

INFLUENCE OF THERMALLY GROWN OXIDE LAYERS THICKNESS ON TEMPERATURE EVOLUTION DURING THE FORGING OF LARGE SIZE STEEL INGOTS

Ali Vedaei-Sabegh[1], Jean-Benoît Morin[2], Mohammad Jahazi[1*]

[1] École de Technologie Supérieure, Department of Mechanical Engineering, 1100 Notre-Dame Street West, Montreal, QC, H3C 1K3, Canada.

[2] Finkl Steel Inc., 100 McCarthy, Saint-Joseph-de-Sorel, QC, J3R 3M8, Canada

Abstract

Medium carbon low alloy specialty steels are preheated in gas-fired furnaces before undergoing open die forging operation. Oxide layers with different thicknesses and compositions are formed on the surface and significantly influence the temperature evolution during the forging process. In the present work, the kinetics of oxide growth of two high-strength medium carbon steels with different Ni concentrations, were determined. Four oxidation temperatures and five oxidation times were used to simulate various forging and intermediate heat treatment conditions. Three distinct oxide layers with different thicknesses were identified and correlated with the applied thermal cycles. The results indicated that the kinetics of oxidation varied with the Ni concentration of the alloys, but interestingly the fractions of different layers were the same at different oxidation temperatures. A 3D finite element model (3D-FEM) was developed, and the effect of the oxide layer investigated on the temperature evolution of the ingots. Correlations are made between the thickness of the oxide layers and the cooling pattern of the ingots, as well as their impact on the forging die temperature. The 3D-FEM predicted critical temperatures were validated by experimental temperature measurements on the ingot during the forging process.

Keywords: High-temperature oxidation, Oxidation kinetics, oxide layer thickness fractions, heat transfer

3.1 Introduction

The majority of steel will experience thermally grown oxidation, during heat treatment or hot deformation, due to the interaction of reactive gaseous environments with solid material Birks et al. (2006). Thermal oxidation is a source of material waste and causes surface defects like cracking that can impose severe surface integrity problems and decrease the service time of parts Utsunomiya et al. (2009). This material waste can be affected by slight changes in material composition Hu et al. (2013). During forging, the oxide layers can detach and penetrate ingots, causing cracks, which sometimes leads to scraping an ingot. The oxide layers can remarkably influence the friction between die and ingot and make tool wear Barrau et al. (2003). Also, oxide layers can affect the heat transfer of ingot to the ambience or in contact with the die Jang et al. (2010). Hence, it is crucial to evaluate the kinetics of oxide growth and provide a better understanding of the influence that scale has on heat transfer of ingots, as the temperature gradient can cause undesired material characteristics in different zones of an ingot. Throughout the oxidation process, the Fe ions diffuse outward through different oxide layers to reach the air for oxidation at the top surface of the oxide. The chemical equilibrium is instated at the interfaces of metal-oxide and oxide-reactive gas. The diffusion of Fe cations (Fe^{2+} and Fe^{3+}) and oxygen anions (O_2^-) are the factors affecting the oxidation process Suárez, Rodríguez-Calvillo, Houbaert, et Colás (2010). However, the diffusion of Fe cations in steel is faster compared to the diffusion of oxygen in steel. Hence, the main affecting factor in the kinetics of oxide growth is the diffusion of Fe cations Wakasa et Yamaki (1988).

Temperature and time are pivotal factors affecting the diffusivity of Fe, and therefore, the growth rate of oxide layers Munther et Lenard (1999). (Hu et al., 2013) assessed the oxidation of high carbon steels at high temperatures above 1073 K and observed the parabolic oxidation behavior. The results indicated a higher oxidation rate above 1173 K, particularly in the first 20 s. (Birosca et al., 2005) observed the parabolic behavior of oxidation for low carbon steels

for oxidation in air at 923 to 1373 K. The assessment of oxidation kinetics for short-time oxidation of low-carbon, low-silicon steel in the air at 1123 to 1453 K was conducted by (R. Y. Chen & Yuen, 2008). The study concluded that the oxidation had a linear growth kinetic which substituted to parabolic behavior after a certain oxidation thickness was achieved. This thickness increased by increasing the oxidation temperature. The same oxidation behavior, varying from linear to parabolic behavior, was reported by (Cao et al., 2014) for low carbon steel oxidation, at 773 to 1173 K in air. (R. Chen & Yeun, 2003) investigated the oxidation behavior of pure iron and mild carbon steel at an oxidation temperature of 973 to 1373 K. The oxidation kinetics had a parabolic growth for different oxidation environment, including oxygen or air. (Higginson et al., 2006) compared the growth of oxides in low alloy steel and stainless steel at temperatures between 1273 and 1473 K in air. The results showed that the oxidation rate of stainless steel was slower than low alloy steels, due to the formation of passive layers composed of corundum or spinel crystallographic structures.

Considering the oxidation kinetics, the oxidation atmosphere can remarkably influence the oxidation at high temperatures. (Yuan, Wang, et al., 2013) assessed the oxidation of iron in oxygen and steam at 923 to 1023 K. The results demonstrated parabolic and linear-parabolic oxidation behavior for oxidation in oxygen and steam, respectively. (Cheng et al., 2015) evaluated SUS 430 oxidation at 1273 to 1423 K in the humid air. The results conveyed the parabolic behavior of oxidation at all temperatures.

Along with the oxidation temperature and time, the chemical composition of the alloy is another critical factor affecting the oxidation behavior. In this regard, one of the most critical alloying elements influencing the oxidation kinetics is carbon reported by (R. Chen & Yeun, 2003). (C. Wang & Duh, 1988) showed that depending on the oxidation conditions, carbon can demonstrate both accelerating or decelerating effect on oxidation. Other alloying elements such as Si (Silicon), Al, and Cr (Chromium) also have important impacts on the oxidation kinetics of low alloys steels. (Mouayd et al., 2014) investigated the effect of Si on oxidation of low alloy steels. The results indicated a remarkable decrease in oxide growth below 1450 K and a lower effect of Si above this oxidation temperature. The influence of Al (Aluminium) on

the resistance to high-temperature oxidation of carbon steels was investigated by (Kao & Wan, 1988), who reported that the formation of α-Al_2O_3 during oxidation was the main contributing factor to the observed improvements. The beneficial effects of Al on high-temperature oxidation was related to the increase in the formation temperature of wustite by (Krzyzanowski & Beynon, 2006). (Takeda et al., 2010) investigated the effect of Cr on the oxidation of three low carbon steels. They found that the formation of $FeOCr_2O_4$ at the oxide–metal interface reduced the oxide removability, thereby slowing down the oxidation rate. (Krzyzanowski et al., 2010) reported that in the oxidation temperature range of 773 to 973 K, the effect of Si or Al on oxidation resistance was more than Cr, by comparing the outcomes of former studies.

Little information is available on the effect of Ni (Nickel) on high-temperature oxidation of Ni-rich medium carbon steels. Among the few available studies, (L. Yin et al., 2010) investigated the effect of Ni on the high-temperature oxidation of Fe-Cu-Ni alloys and reported that the addition of Ni decreased the oxidation rate at 1423K. This phenomenon was contributed to the decrease of Fe activity in the liquid-Cu phase by enrichment of Ni at the liquid-Cu/γFe interface. (B. Webler, Yin, & Sridhar, 2008) evaluated pure iron oxidation by adding 0.3 Cu and 0.3 Cu + 0.1 Ni as alloying elements and found that the oxidation was decreased to half by adding the Cu + Ni in iron. In another study, (Asai et al., 1997) reported that the addition of Ni decreased oxide removability in a 0.02 mass% Si steels oxidized at 1373 and 1523 K; however, they did not study the kinetics of oxidation in the presence of Ni.

Furthermore, it has also been reported that the effectiveness of alloying elements varies with the oxidation temperature. For instance, (R. Chen & Yuen, 2005b) investigated the effect of Cu and Ni on the oxidation of copper-containing steels in the temperature range of 1253 to 1493 K. They reported that at 1253 K, the addition of Cu and Ni increased the oxidation resistance while at1393 K, the presence of Cu decreased the oxidation resistance. At 1493 K, the addition of Cu and Ni had no significant effect on oxidation resistance.

The scale of pure iron is comprised of three distinct layers: wustite (FeO), magnetite (Fe3O4), and hematite (Fe2O3), with the thickness fraction of each layer being about 0.95, 0.4, and 0.1,

respectively Suarez et al. (2009). Wustite is closer to the base metal, and its growth depends on the diffusivity of Fe. In contrast, hematite is at the outermost, and its growth depends on the diffusion of oxygen due to the abundance of oxygen. From a mechanical resistance point of view, wustite has the lowest hardness and acts as a lubricant during high-temperature deformations. Hematite has the highest hardness and causes friction and wear on die surfaces, while magnetite has intermediate hardness levels Zambrano et al. (2015).

It must be noted that the fraction and characteristics of each layer vary as a function of the chemical composition of the base metal, oxidation temperature, oxidation atmosphere, oxidation time, and oxidation pressure Birks et al. (2006). For example, (Liu et al., 2013) investigated the oxidation of a micro-alloyed steel at 1173-1473 K and reported that the wustite thickness increased by increasing the oxidation time and temperature. In contrast, the magnetite layer's thickness decreased, while no remarkable effect was found on hematite thickness. (R. Y. Chen & Yuen, 2009) oxidized low carbon steel in a $17H_2O-N_2$ atmosphere at 1173 K and observed only outer thin magnetite and an inner wustite layer. (Yun et al., 2013) did not observe any wustite layer for the oxidation of a low carbon steel at 773 K. In comparison, when the same steel was oxidized at 973 K, the thickest oxide layer was made of wustite. (HT Abuluwefa et al., 1997) investigated the oxidation of a low carbon steel at 1073-1423 K, in different oxidation atmospheres. The results showed a single wustite layer and all three layers of oxides for oxidation in water vapor and pure oxygen, respectively.

The above analysis of the state-of-the-art shows that the chemical composition and mechanical properties of each of the oxide layers are different and that their thickness varies with the processing conditions. Therefore, it is reasonable to expect that such differences influence the heat transfer process during ingot forging. However, although many publications are available on the experimental or modeling of heat transfer during hot deformation of low alloy carbon steels Bai et al. (2012), very little information is available on the role of oxide layers on the heat transfer process. For example, (Dubey et al., 2012) developed a model to evaluate the effect of heating for a steel billet with oxide layer. A significant difference in the temperature gradient of billets with and without scale was revealed by the authors. (Jang et al., 2010)

assessed the heating characteristics of a high carbon steel slab in a reheating furnace by considering the effect of oxide growth at 1473 K. The outcomes indicated the slow heating rate of the slab due to the low conductivity of the oxide layer. (Dong et al., 2017) employed an implicit finite difference method to evaluate the temperature field of the slab with oxide during heating. The results demonstrated that the scale could remarkably impact the slab temperature. (M. Kim, 2013) showed that by increasing the oxide thickness of a large-sized high carbon steel slab heated at 1473 K, the oxide layers could prevent heat transfer from the furnace to the slab. The average temperature of the slab with the oxide layer was 100 °C lower than a slab without scale in some regions. (X. Wang et al., 2018) evaluated the heating of the dynamic slabs in walking-beam reheating furnaces, considering the insulating effect of the oxide layer. This study revealed that the soaking time of the slab to reach 1473 K will increase 1000 s by 2 mm of scale. (Jaklič et al., 2002) employed three-dimensional finite-difference solutions to investigate billet temperature during transportation from the furnace to the rolling mill. The developed model was verified using a thermal camera and indicated a remarkable temperature difference between billet with oxide layer and billet without oxide.

Although the above analysis of the published literature shows a clear impact of the presence of the oxide layer on heat transfer, very little information is available on the role of each layer. The information is even more scarce when it comes to forging large-sized ingots, being mostly focused on rolling applications. Hence, the main aim of this study is to develop a better understanding of the growth of oxide layers during the heating and cooling cycles corresponding to the open die forging of large size ingots. The determined constitutive equations were then implemented in a 3D finite element (FE) model that was developed in the present study in order to assess the effects of oxide layers on the heat transfer process in a large size ingot. Two medium carbon low alloy steels with different Ni contents were also studied to evaluate the impact of chemical composition on the kinetics of oxide growth and its impact on the heat transfer process. The fractions of different layers were assessed for different oxidation times and temperatures for the two alloys. The developed model simulated the heat transfer of the large size ingot in the presence of the oxide layers. Finally, model predictions were validated at the industrial scale, demonstrating about 7% discrepancy with experimental

evaluation at 1473 K. So, the developed model can be employed in the industry as the simulation results are in an appropriate agreement with the experimental test.

3.2   Materials and methods

Table 3.1 provides the chemical composition of two employed high strength steels for this study. These steels are identified as low nickel (LNi) for modified AISI P20 steel and high nickel (HNi) for Nickel-modified AISI 4330 steel, where the HNi has 6 times higher nickel content compared to LNi. The steels were supplied by Finkl steels Sorel, Quebec, Canada.

Table 3.1 Chemical composition of utilized steels in this study (wt%)

	C	Mn	Si	Ni	Cr	Mo	Cu
LNi	0.35	0.99	0.41	0.5	1.86	0.53	0.16
HNi	0.35	0.99	0.41	2.92	1.86	0.53	0.16

For oxidation tests, considering that it was not possible, due to the intense heat and safety issues, to measure the oxide thickness on the actual ingots (about 40 tons) at the oxidation temperatures, samples were machined from the as-cast ingots, and experiences were conducted in the laboratory. Cylindrical samples were prepared with 10 mm of diameter and 15 mm of length, using a precision cutter for oxidation tests. Four oxidation temperatures of 1273.15, 1373.15, 1425.15, and 1473.15 K were selected according to the actual working temperatures in the industry to measure the oxide thickness for oxidation times of 3, 10, 20, 30, and 60 min. Prior to conducting oxidation tests, samples were grounded by 320 mesh SiC papers to provide the same surface roughness on all samples. Afterward, samples were cleaned ultrasonically in distilled water and ethanol for 15 min and protected in a vacuum chamber. The indicated sample preparations were employed to provide the same test condition for all samples and make an appropriate comparison and analysis. However, on the industrial scale, the surfaces can be different. The contaminations like dust or oils can be present on the surface, suppressing the oxidation by decreasing the diffusion of oxygen in material Vedaei-Sabegh, Morin, et Jahazi (2020). The ambiance air can affect the oxidation kinetics, too. The humidity in the air

can boost oxidation at high temperatures Yuan, Wang, et al. (2013). Also, the surface roughness can be different, particularly for as-cast ingots. The higher surface roughness will bring a higher surface to volume ratio, and consequently, higher oxidation rate Nowak (2018). However, some studies showed that the higher surface roughness could decrease the oxidation of some materials Nowak (2020).

The oxidation tests were conducted employing a material testing system machine (MTS) equipped with a radiative furnace, ChamberIR E4 elliptical chamber heater. The radiative chamber takes advantage of four elliptical polished aluminum reflectors to focus the provided infrared energy on the center axis.

For oxidation experiments, samples were heated under the protection of argon gas with a flow rate of 50 ml.min^{-1}. Samples were heated at a rate of 2 °C/s. When the samples reached the desired temperature, the argon gas switched off, allowing the air to enter the chamber and start the oxidation. After oxidation for a designated time, the argon gas was reintroduced to the chamber to suppress further oxidation and cool the sample down to room temperature. The furnace temperature was controlled by a proportional–integral–derivative controller (PID controller), with an accuracy of ±3 °C. To ensure the uniformity of temperature distribution all around the sample, two K-type thermocouples were used on the opposite side of the furnace thermocouple, and the temperature profiles were recorded by Graphtec data logger. The heating cycle for the oxidation process is given in Fig. 3.1.

Temprature(° C)

1200
1150
1100

1000

25

Oxidation under air
for 3, 10, 20, 30 and 60 min

Time (min)
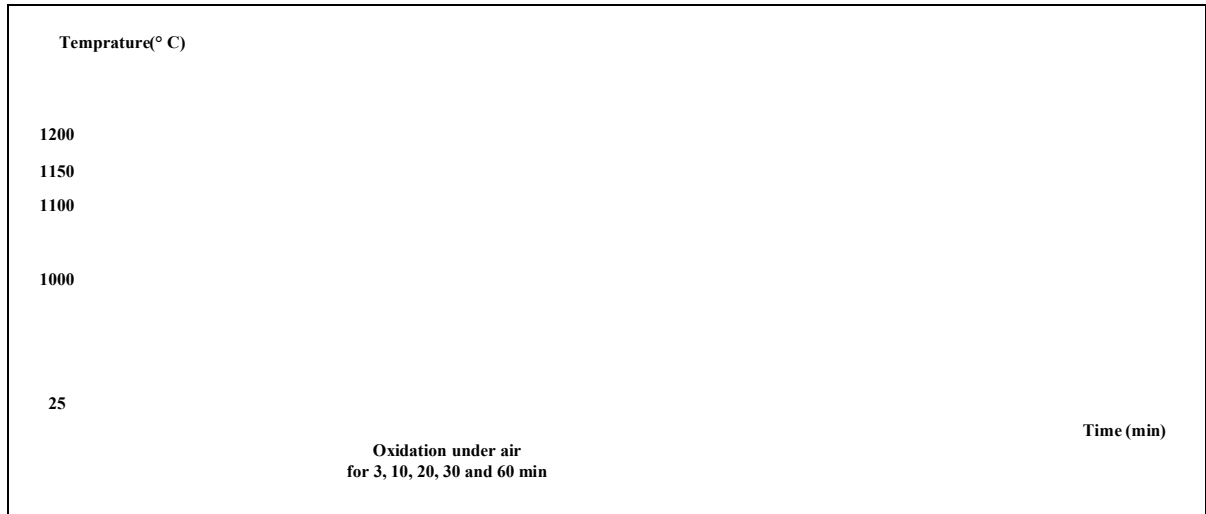
Figure 3.1 Heating cycle for the oxidation process

Oxide layers on the samples are fragile and need special care to preserve oxide integrity for microscopic examinations. In this regard, a special copper-based powder cold mount was employed to guard the oxide and minimize the damage during manipulation. The Technovit 5000 powder (which is 90% copper) is mixed with Technovit 5000 liquid (which is methyl methacrylate+ tetramethylene dimethacrylate+ triethylen glycol dimethacrylate) with mixing ratio of 2:1, respectively. The mixture is poured on the sample slowly letting the trapped air bubbles to escape. The samples are ready after seven minutes in room temperature. After the cold mount, the samples were cross sectioned utilizing a diamond blade on a precision cutter and were grounded to 800 mesh on SiC papers. To provide a smooth surface finish, samples were polished on a Buehler vibrometer polisher for 6 hours in a 0.05 μm colloidal silica suspension. A LEXT OLS4100 laser confocal microscope was employed for microscopic investigations.

3.3   Finite element modeling and boundary conditions

To assess the effect of oxide layers thickness during the cooling of ingots, a finite element model was developed using Abaqus CAE software. Two sets of simulations were developed.

In the first set, the ingot was not in contact with other materials; therefore, no conduction occurred in the process. In the second set, the same ingot is in contact with the forge anvil. In this regard, industrial size ingots were modeled with dimensions of 1.4×1×2.75 m (W×H×L). LNi material was selected for finite element analysis, and JMatPro software was utilized to acquire the thermal properties (such as thermal conductivity and specific heat) of LNi as a function of temperature. This approach was successfully employed in former studies Saunders, Guo, Li, Miodownik, et Schillé (2003). For this purpose, the chemical composition and cooling rate of the material are given to software to acquire the phase fractions and thermal properties. Whenever possible, the above constants were determined experimentally to minimize the use of the software. These experiments also helped to validate the predictions made by the JMatPro database. To this end, the thermal properties of the LNi alloy were determined up to 1223.15 K using a FlashLine™ 3000 thermal properties tester. In this method, a short laser pulse is beamed on the surface of a thin disc, and the temperature variation is measured on the rear surface to acquire the thermal properties. The thermal properties of different oxide layers were extracted from former studies. (Akiyama, Ohta, Takahashi, Waseda, & Yagi, 1992) used the flash method to acquire the conductivity of oxide layers, which is given in Fig. 3.2.a. The specific heat of oxide layers was studied by (M. Li et al., 2019), and the results are presented in Fig. 3.2.b.
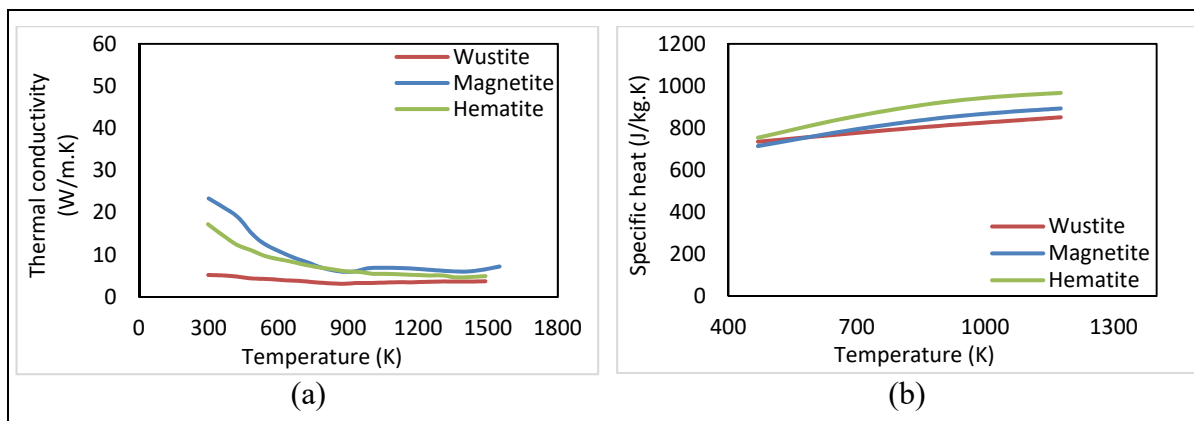
Figure 3.2 Thermal properties of oxide layers: a) thermal conductivity, and b) specific heat
Taken from Akiyama et al. (1992, p. 830) and Li et al. (2019, p. 400)

The forging anvils were made from waspaloy. The thermal properties of waspaloy were obtained from the database of FORGE® NxT 3.0 software and from the literature, as reported in Fig. 3.3 by (Ding & Shin, 2013).
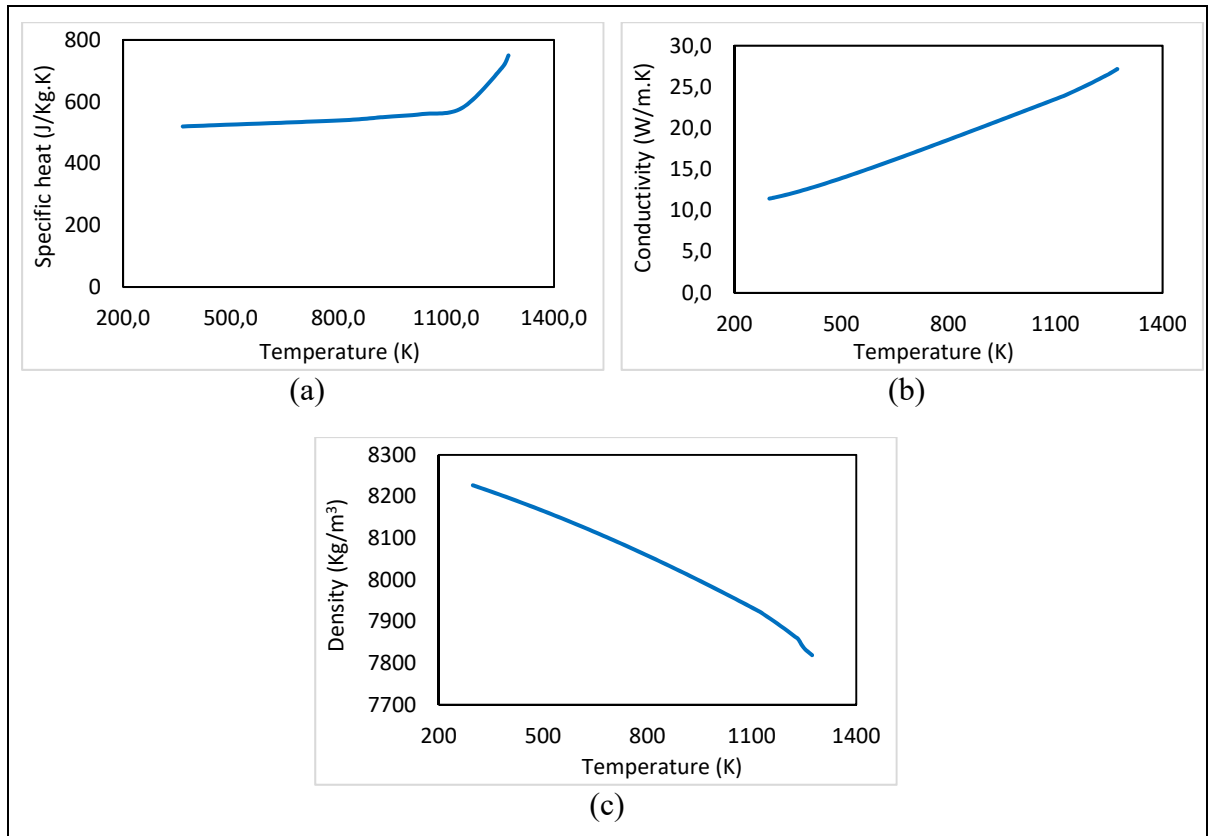
Figure 3.3 Material properties of Waspaloy: a) specific heat, b) conductivity, and c) density

The simulations were conducted as transient heat transfer. During the cooling from high temperature, the oxide continues to grow. However, this growth has not been considered in former studies (e.g., (Y. Chang, Tang, Zhao, Hu, & Wu, 2016)). To consider the growth during cooling, the cooling of an ingot was simulated without oxide. The acquired temperature for cooling is utilized to obtain the oxide growth during the cooling. For convection, the emissivity coefficients of 0.9 for the oxide layer Burgess et Foote (1916), 0.7 for the ingot surface Chalkley (2020), and 0.8 for waspaloy anvil Kieruj, Przestacki, et Chwalczuk (2016) were utilized. For convection, the h-values (W/m.K) will be different for different surfaces of ingot

and die. Different surfaces of ingot and die are shown in Fig. 3.14. For this purpose, the Rayleigh number is obtained as follows by (Holman, 2002):

$$R_a = G_r \times P_r = \frac{g\beta(T_s - T_\infty)L^3}{v^2} P_r \tag{3.1}$$

$$T_f = \frac{T_\infty + T_s}{2} \tag{3.2}$$

where G_r is the Grashof number for characteristic length x, P_r is the Prandtl number, g is the acceleration due to gravity, β is the thermal expansion coefficient (equals to $1/T$, and T is absolute temperature), T_s is the surface temperature, T_∞ is the quiescent temperature (fluid temperature far from the surface of the object), and v is the kinematic viscosity. The properties of P_r, v, and β are obtained at the film temperature, T_f.

The Nusselt number (the ratio of convective to conductive heat transfer across a boundary) can be acquired as follows by (Holman, 2002):

$$Nus = \frac{\bar{h}l}{k} \tag{3.3}$$

where $\bar{h}$ is the convective heat transfer coefficient, L is the characteristic length, and k is the thermal conductivity of the fluid. The nusselt number for different surfaces of the ingot can be calculated according to (Holman, 2002), as follows:

$$Nus\ (top) = 0.27 \times R_a^{\frac{1}{4}} \qquad\qquad \text{Top surface} \tag{3.4}$$

$$Nus\ (side) = 0.825 + \frac{0.387 \times R_a^{\frac{1}{6}}}{\left[1 + \left(\frac{0.492}{P_r}\right)^{\frac{9}{16}}\right]^{\frac{8}{27}}} \qquad 10^9 < R_a < 10^{12} \quad \text{Side surfaces} \tag{3.5}$$

$$Nus\ (side) = 0.68 + \frac{0.670 \times R_a^{\frac{1}{4}}}{\left[1 + \left(\frac{0.492}{P_r}\right)^{\frac{9}{16}}\right]^{\frac{4}{9}}} \qquad R_a < 10^9 \quad \text{Side surfaces} \qquad (3.6)$$

$$Nus\ (bottom) = 0.54 \times R_a^{\frac{1}{4}} \qquad\qquad\qquad \begin{array}{c}\text{Bottom}\\\text{surface}\end{array} \qquad (3.7)$$

Hence, the convective h-values can be accessed for different surfaces. For the first set of simulations, a quarter of ingot is considered, taking advantage of symmetry and decreasing the simulation time. For the second set, half of the ingot and anvil are modeled (the simulation by a quarter of the ingot was not possible in this case, as the ingot was in contact with the anvil just on the front side of the ingot). The DC3D8 elements were used for oxide layers, steel, and waspaloy. DC3D8 is an 8-node linear heat transfer brick. A suitable mesh size was allocated considering the convergence of boundary values of developed model, where decreasing the mesh size below employed amounts did not affect the accuracy of model. The thickness of the oxide layer is divided into 5 nodes, with total number of 307350 elements. The ingot and die are biased meshed, where the meshes are finer near the oxide layers and coarser in the outlying areas from critical contact zones, with total element numbers of 227500 and 103284 for ingot and die, respectively (see Fig. 3.14).

After analyzing the convergence of the boundary value, a suitable mesh density around the contact area was found to be roughly a quarter of the coating thickness.

3.4   Results and discussion

3.4.1   Kinetics of oxide growth and different sub-layers

Fig. 3.4 illustrates the scale growth by time and temperature for LNi and HNi steels. The parabolic growth can be seen for both steels.
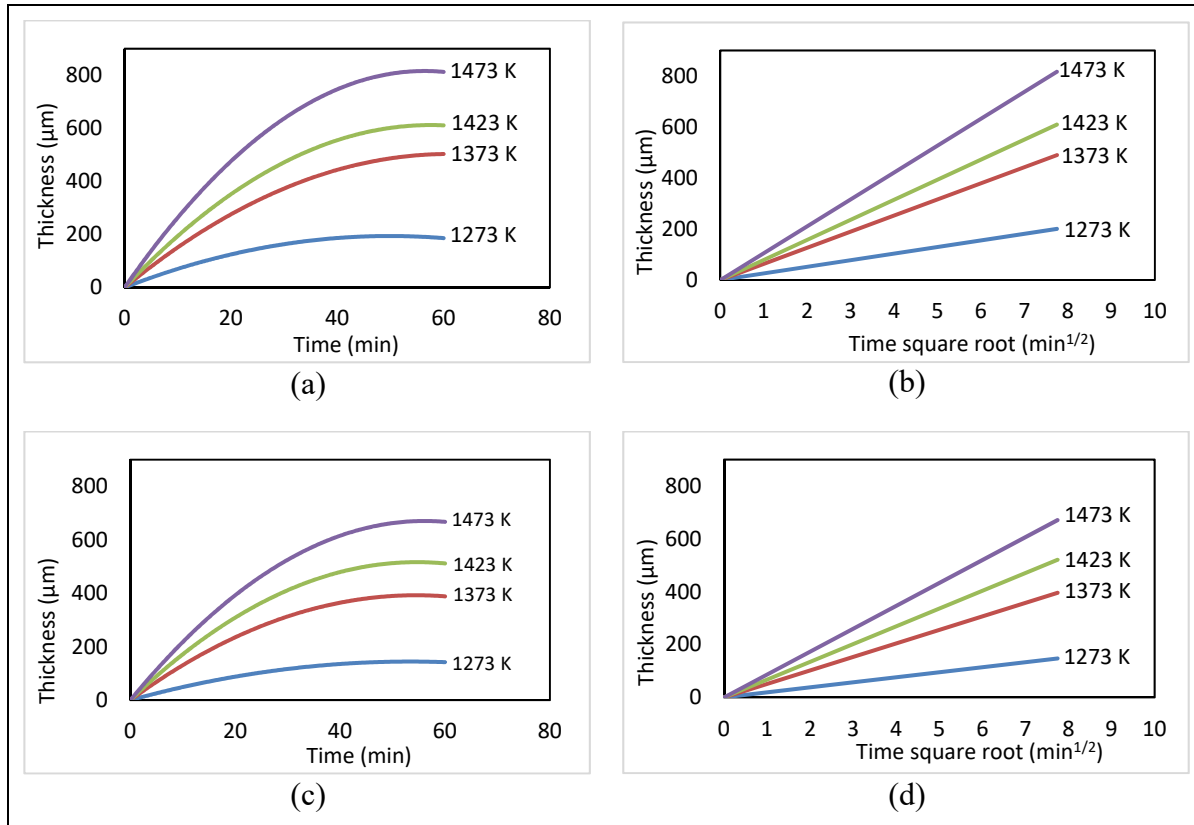
Figure 3.4 Oxide thickness growth for: a) LNi, b) LNi growth by time square root, c) HNi, and d) HNi growth by time square root

For both steels, the oxide thickness increases by increasing the oxidation temperature and time. For each specific oxidation temperature, the oxidation rate decreases with time. For instance, the oxide thickness of LNi steel at an oxidation temperature of 1273 K, increased 86% by increasing the oxidation time from 3 min to 10 min. However, the oxide thickness increased 56% after raising the oxidation time from 10 min to 20 min. This phenomenon is more remarkable at higher temperatures. As for the oxidation temperature of 1473 K, the oxide thickness increased 116% after raising the oxidation time from 3 to 10 min. The rise was 32% for increasing the time of oxidation from 20 to 30 min. As the rate-controlling factor in the oxidation process, the solid-state diffusion can be attributed to this behavior. At the commencing steps of oxidation, there are no oxide layers on the steel surface. Hence, oxygen can easily reach Fe to cause oxidation. However, as the oxidation proceeds, oxygen must pass

through formed oxide layers to reach Fe. So, the freshly formed oxide layers work as barriers for oxygen diffusion, which slow down the oxidation. In other words, the increase in the oxide thickness, after initial oxide growth stages, will rely on how easily the diffusion will take place for oxygen and Fe through formed oxide layers.

The above-discussed mechanism is in agreement with the parabolic growth rate of oxide thickness, which is expressed as follows Suárez et al. (2008):

$$h = \sqrt{k.t}$$
(3.8)

where h, k, and t are oxide thickness (cm), parabolic growth rate (cm^{2}s^{-1}), and time (s), respectively. The oxidation will decrease until it reaches a plateau. Afterward, more oxidation will result in thicker oxide, but with the same growth rate. At 1473 K, the oxide thickness increased about 61% and 32% for increasing oxidation time from 10 to 20, and 20 to 30 min, both 10 min time intervals. However, for raising the oxidation time from 30 to 60 min, the oxide thickness increased 32%, demonstrating a plateau had been reached for the oxidation rate.

Furthermore, considering the close results for oxidation at 10 and 20 min for both steels, the oxidation results of 3 min are remarkably lower than all other oxidation times. The lower results could be attributed to the relation of oxide thickness to the square root of time, where there was not enough time for oxygen diffusion. For a particular oxidation time, by increasing the oxidation temperature, the oxide thickness will increase. For instance, the oxide thickness for LNi steel at 20 min of oxidation time increased about 123% and 168% by increasing the oxidation temperature from 1273 to 1373 and 1423 K, respectively. The oxide thickness increased remarkably about 262% by increasing the oxidation temperature from 1273 to 1473 K, which shows the importance of temperature in oxidation.

The discussed trends were observed for both steels at all oxidation temperatures and times, though the oxide thickness was lower for HNi steel than LNi. The oxide thickness was about

22% more for LNi at an oxidation temperature of 1473 K and an oxidation time of 60 min. The difference between the two steels in terms of oxide thickness was more significant at higher oxidation temperatures and oxidation times. Hence, the material waste due to oxidation is higher for LNi, compared to HNi steel. The only difference between two steels at the same oxidation conditions was Ni as an alloying element. The mechanisms that Ni hinders the oxidation process were discussed in detail in a former study Vedaei-Sabegh et al. (2020).

Based on illustrated results in Fig. 3.3, and considering equation 3.4, the activation energy (E_A) for the oxidation of two materials can be acquired from the slope of the curve ($ln\ k_p/k_0$-$1/RT$) given in Fig. 3.5 Young (2008):

$$k_p = k_0 exp\left(-\frac{E_A}{RT}\right)$$

(3.9)

Where k_p, k_0 are parabolic oxidation kinetic constants ($g^2.cm^{-4}.s^{-1}$), E_A is the activation energy for the oxidation ($J.mol^{-1}$), R is the gas constant ($8.314\ J.mol^{-1}.K^{-1}$), and T is the absolute temperature (K).

(a)   (b)
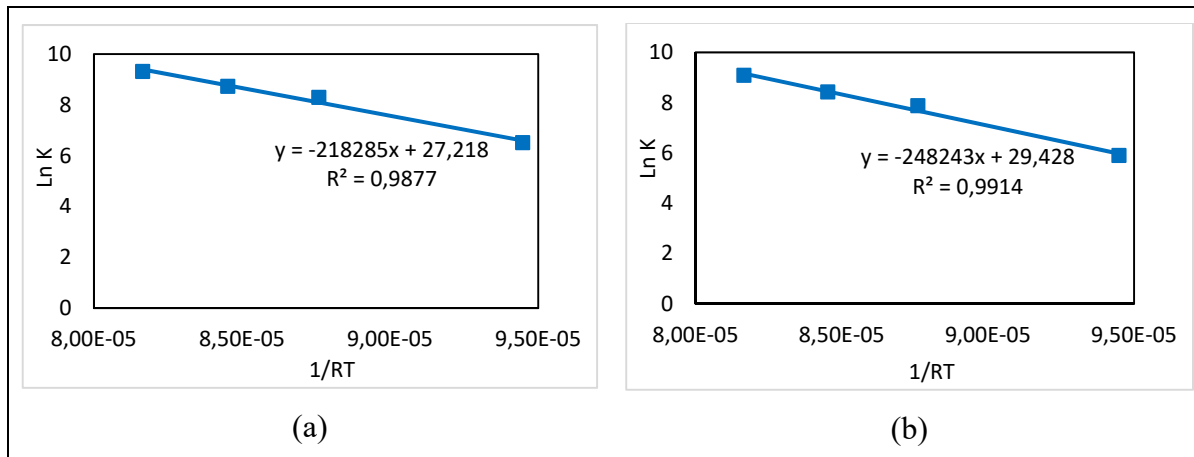
Figure 3.5 Acquired activation energies for the oxidation process of:
a) LNi and b) HNi steels

The activation energies for LNi and HNi steels are 218 and 248 kJ.mol^{-1}, respectively. The higher resistance of HNi steel to oxidation can be seen with its higher activation energy. Examining the images by LEXT confocal microscope in Fig. 3.6 for oxidized samples at 1273 K for 60 min, the three major sub-layers of wustite, hematite, and magnetite can be seen for both steels. The overall thickness of HNi and all the sub-layers are thinner compared to LNi.
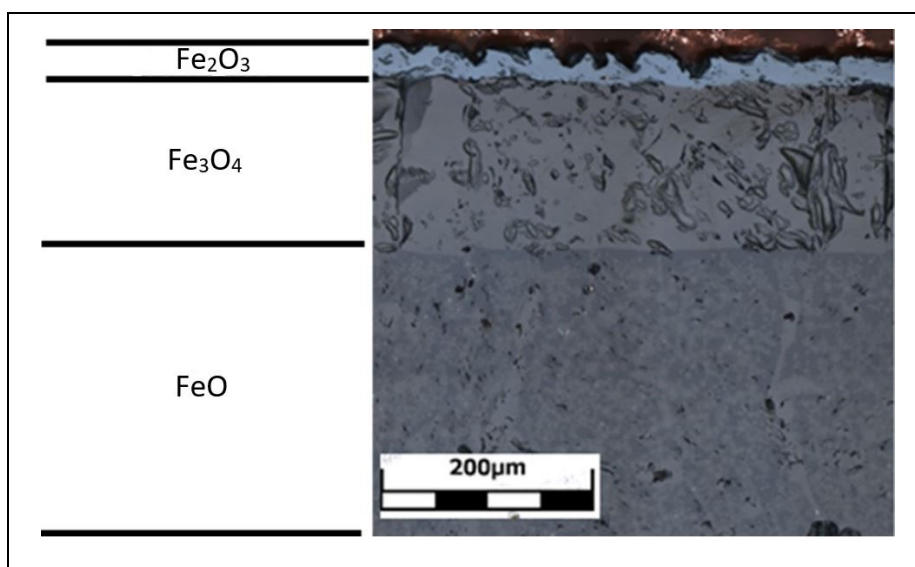
Figure 3.6 Image by LEXT laser confocal from oxide layers
of the oxidized sample at 1000 °C for 60 min, LNi steel,
(magnification on the top side of sub-layers of LNi oxide)

Similar to the parabolic growth of oxide overall thickness, the sublayers demonstrated the parabolic growth rate in all oxidation temperatures. This behavior was observed for both steels (see Fig. 3.7).
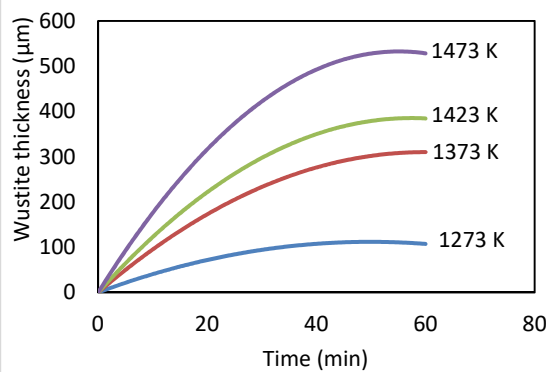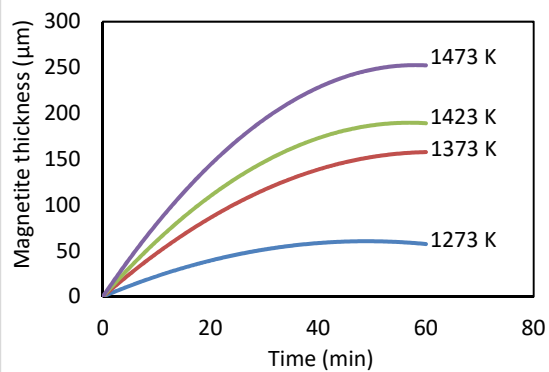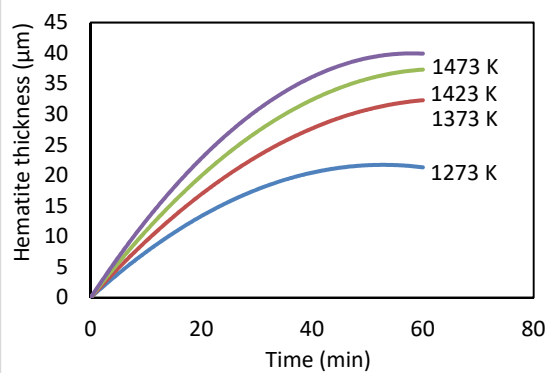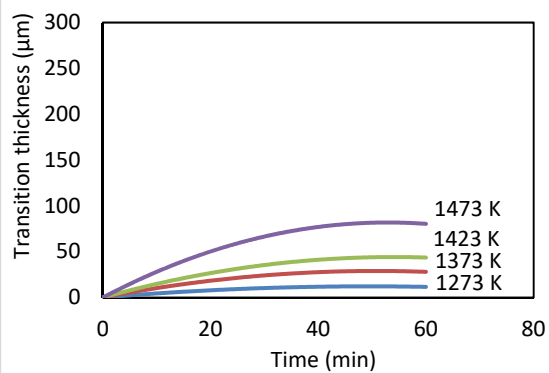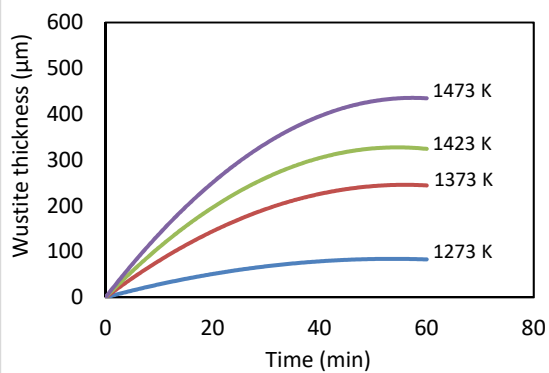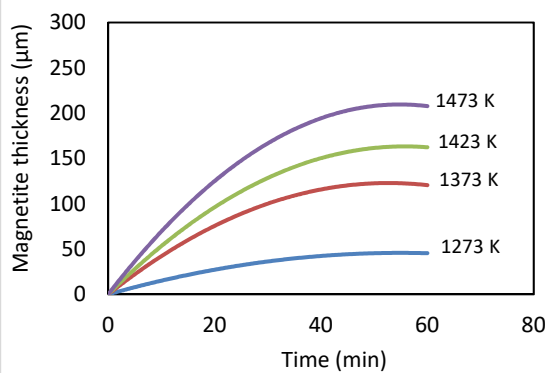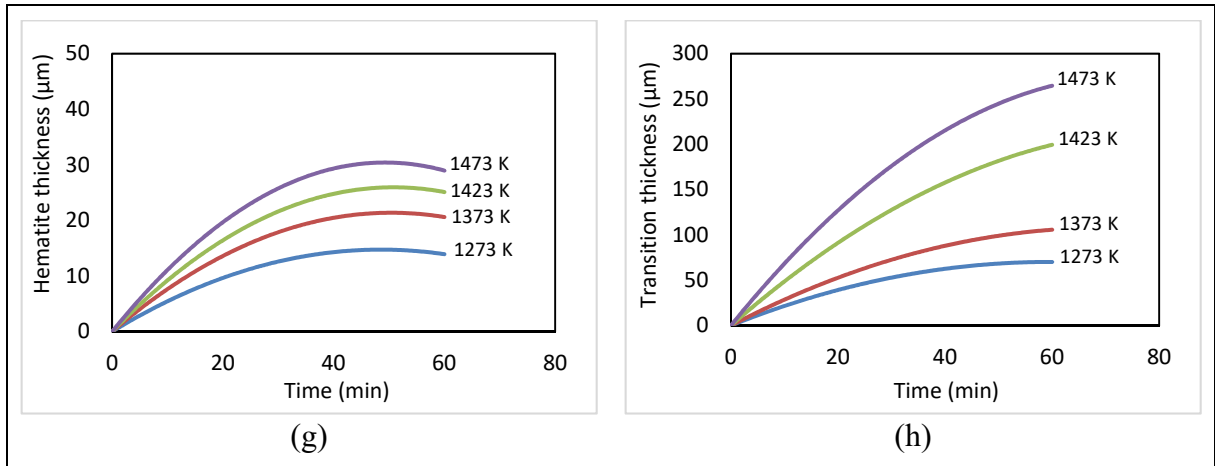
Fig. 3.7 Oxide sublayers parabolic growth for: a)LNi wustite, b) LNi magnetite, c) LNi hematite, d) LNi transition, a)HNi wustite, b) HNi magnetite, c) HNi hematite, and d) HNi transition

All the sublayers of HNi steel are lower than those of LNi. However, the transition layer of HNi is far higher than the LNi transition. This thicker transition layer provides bonding between the steel substrate and oxide layers, decreasing the scale removability. Hence, if this oxide is not cleared properly, it can penetrate the ingot during hot deformation and cause cracking and material waste.

As different sub-layers have distinct characteristics, it will be meaningful to assess the variation of thickness for each sub-layer. So, the fractions of layers were obtained for different oxidation temperatures and times. The fraction of layers for both steels oxidized at 1473 K for 60 min are given in Fig. 3.8.
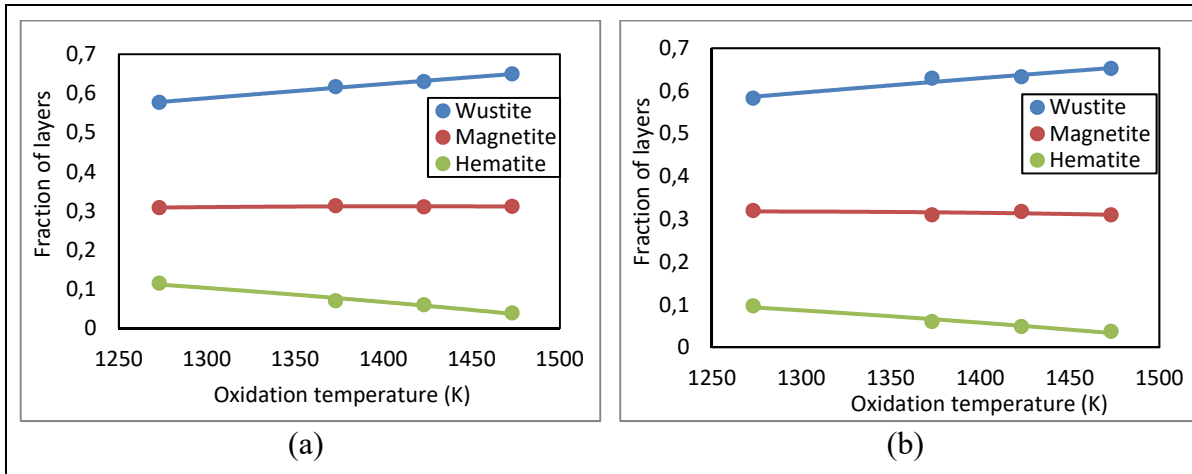
Fig. 3.8 Fraction of sublayers for oxide samples oxidized at 1473 K for 60 min:
a) LNi, and b) HNi

The fraction of wustite is 57% at 1273 K. By increasing the oxidation temperature, wustite fraction increases to 65% at 1473 K. Hematite demonstrates a declining trend by decreasing from 12% to 4% by increasing the oxidation temperature from 1273 to 1473 K. Magnetite does not show any variation by changing the oxidation temperature, dwelling at about 31%. This behavior was experienced for all the oxidation times. Despite the lower thickness of oxide for HNi steel, the same sub-layers were observed with a similar fraction of layers. Considering these fractions of the oxide layers at 1473 K and the density of 7750, 5000, and 4900 kg/m³ for wustite, magnetite, and hematite, respectively, the 60 min oxidation can cause 101 kg of material waste. This material waste will be even more remarkable for some industrial cases discussed in the following sections. So, taking advantage of the indicated results, the industry can predict and avoid excessive material waste at different temperatures due to oxidation.

3.4.2 Developing the finite element model for cooling of large size ingots

The LNi steel was selected for finite element simulations, as the layers of the oxide for both steels are the same Vedaei-Sabegh et al. (2020). In this regard, the thermal properties and density of LNi steel were acquired by JMatPro software and are given in Fig. 3.9 as a function of temperature.
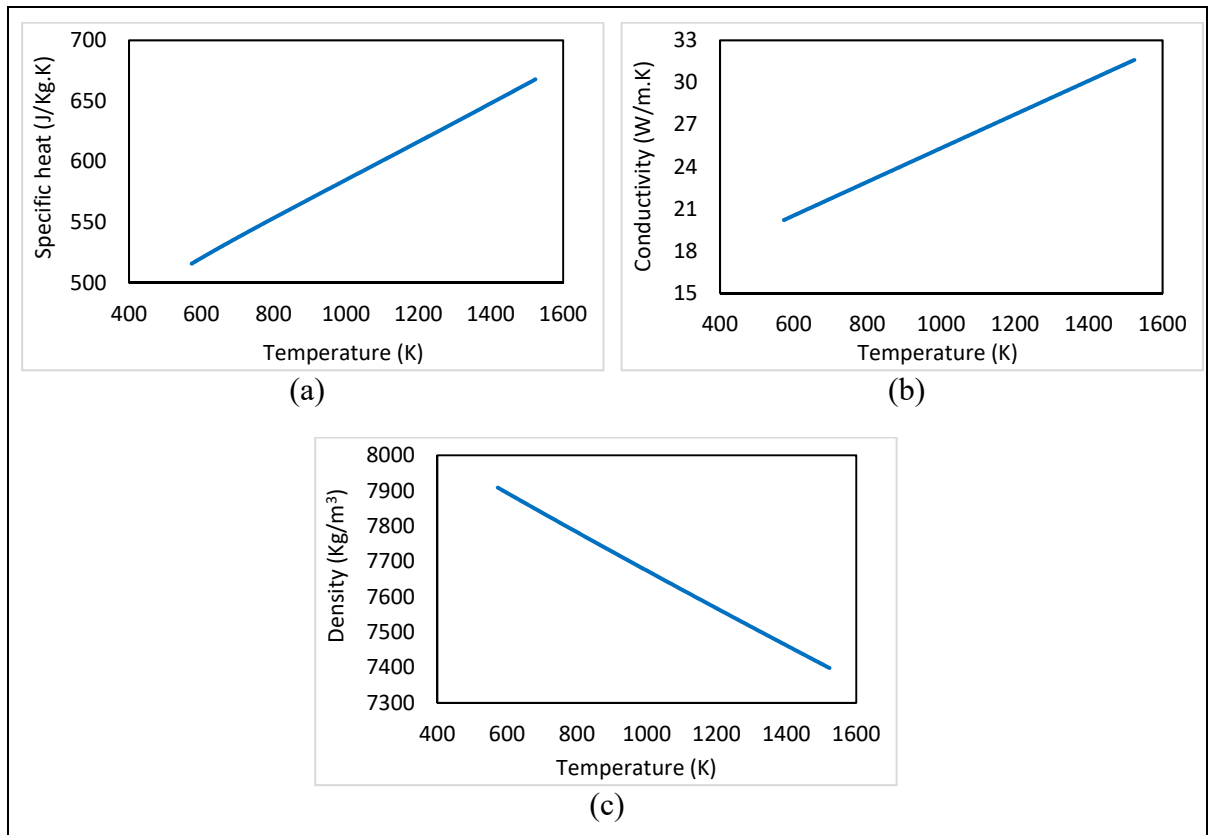
Figure 3.9 Material properties of LNi steel by JMatPro:
a) specific heat, b) conductivity, and c) density

To acquire the illustrated property results on JMatPro, only the austenite part was selected, as the cooling rate and cooling temperature of this study never reach the other phases of steel such as bainite or pearlite. Fig. 3.10 shows the phase fraction of the studied steel during cooling for two different cooling rates. The other phases start to emerge at around 773 K, far lower than the temperature reached in this study during cooling.
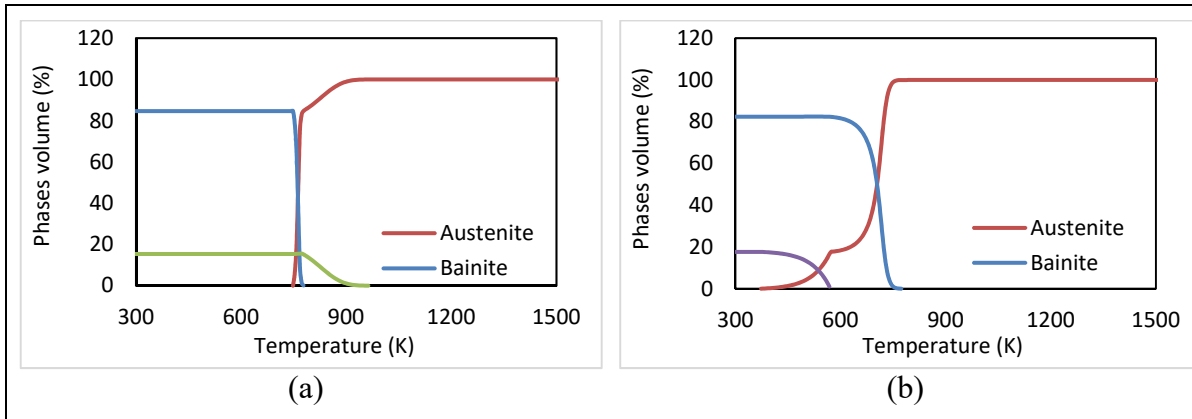
Figure 3.10 Phase volume fraction of LNi during cooling
for cooling rates of: a) 0.01 °C/s, and b) 0.1 °C/s

To ensure the accuracy of the acquired results by JMatPro, the thermal properties were measured utilizing a FlashLine™ 3000 thermal properties tester. The tests were conducted up to 1223 K. The results for thermal properties are illustrated in Fig. 3.11 and are in reasonable agreement with the acquired results from JMatPro software at the studied temperature range.
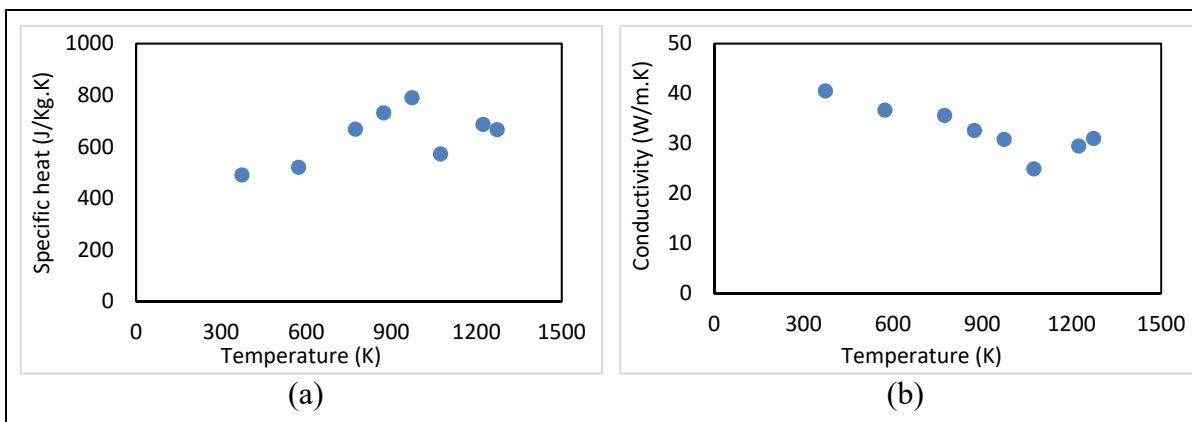
Figure 3.11 Thermal properties of LNi, acquired by flashline thermal property tester

The oxide thickness can be calculated for a large ingot surface from the presented results in Fig. 3.4 for a certain oxidation time and temperature. However, the oxide layer proceeds to grow during cooling up to about 973 K as the situation is still ongoing for reactions causing

thermally grown oxides. To calculate the oxide growth during cooling, an ingot is simulated to cool down from 1473 K without having any oxides. For this purpose, the convection h-values of different surfaces of ingot and the die for finite element simulations are calculated as of Fig. 3.12, according to the given equations of 3.7.
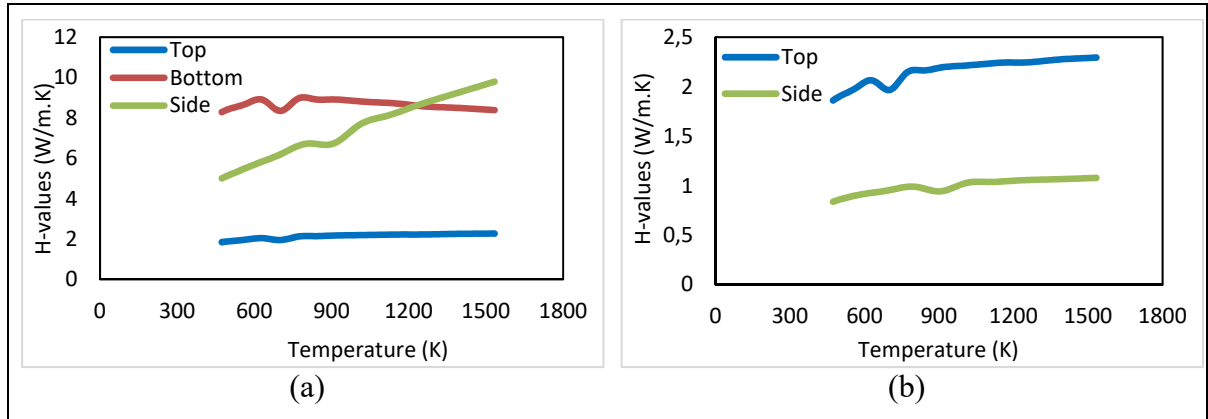
Figure 3.12 h-values for different surfaces of ingot for cooling determined using equations 3.3-3.7

Employing the h-values from Fig. 3.12, the cooling of an ingot without oxide from 1473 K is given in Fig. 3.13. Considering that the acquired oxide thickness results for Fig. 3.4 are for certain oxidation temperatures, the cooling time is calculated for ranges of 1473 to 1423K, 1423 to 1373 K, 1373 to 1273 k, and 1273 to 973 K, where the oxidation due to high temperature diminishes to negligible amounts, and the oxide thickness are acquired for that oxidation temperature and time, as given in Table 3.2.
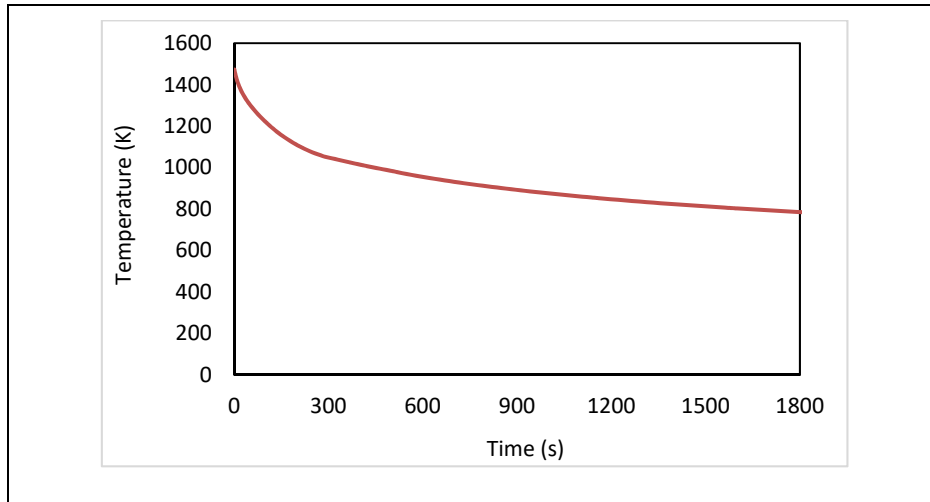
Figure 3.13 Cooling of the ingot from 1473 K without oxide layers

Table 3.2 The oxide thickness growth during cooling of the hot ingot

Temperature range (K)	Cooling time (s)	Oxide thickness (μm)
1425-1473	8	3
1373-1425	11	4
1273-1373	41	8
973-1273	940	105

Accordingly, if for instance, the ingot is being oxidized in a furnace for 60 min, and then it is being cooled, the 120 μm of oxide for cooling stages should be added to the constant oxide thickness of 820 μm, obtained from Fig. 3.4. Furthermore, for each step of cooling, the fraction of layers for the three sub-layers of wustite, magnetite, and hematite are delineated in Fig. 3.7. The developed FE model is shown in Fig. 3.14. The mesh refinement can be seen in the adjacent area to oxide layers. Different sublayers were allocated based on the fraction of layers, and each layer was divided into 5 elements to assure the accuracy of meshing.

Top surface
BC:Radiation-Convection

Steel-oxide interface
BC:Conduction

Big side surface
BC:Radiation-Convection

Steel
BC:Internal conduction

Small side surface
BC:Radiation-Convection

Bottom surface
BC:Radiation-Convection

(a)

Hematite
Magnetite
Wustite

(b)

Die top surface
BC:Radiation-

Die top surface
BC:Conduction to ingot

Die side surfaces
BC:Radiation-

(c)

Figure 3.14 Developed FE model for cooling of large ingot: a) meshing of ingot and oxide layers, b) different sublayers of oxide in the model, and c) meshing of die

Although the oxide thickness and fraction of sublayers are calculated and developed in the FE model, but oxide growth is by time, and the whole thickness will not be on the surface from the outset. Hence, different time steps were allocated for the temperature drop intervals, and the correlated oxide layer was activated at that time step to simulate the growth by time.

3.4.3   Validation of the finite element model of cooling for large size ingots

Prior to verification of the model, considering the close thermal properties of wustite, magnetite, and hematite, the complexity of design for new models, and consequently increasing the simulation time due to the need for finer meshes in each sub-layer, all the sublayers are substituted by wustite (as the dominant layer) to facilitate the simulation process. To evaluate the accuracy of the new procedure, the most complex situation from all testing conditions was selected. The ingot, which was oxidized for 60 min, was in contact with the die and being cooled down from 1473 K for 30 min. To simulate the oxide growth during cooling stages, there will be the simulation steps of 8, 11, 41, 940, and 2600 s for the temperature intervals of 1473 to 1423 k, 1423 to 1373, 1373 to 1273, 1273 to 973, and finally 973 to lower

temperatures (where there will be no oxide growth due to high temperatures), respectively. During each step, a new set of oxide layers will be activated to simulate the oxide growth by time and make the outcomes closer to real-world situations. The thickness of scale layers is designed as of the indicated results in Figs. 3.4 and 3.8 and Table 3.2. The cooling outcomes for two surfaces of the model are illustrated in Fig. 3.15 for temperature variation on the top and bottom surfaces of ingots.
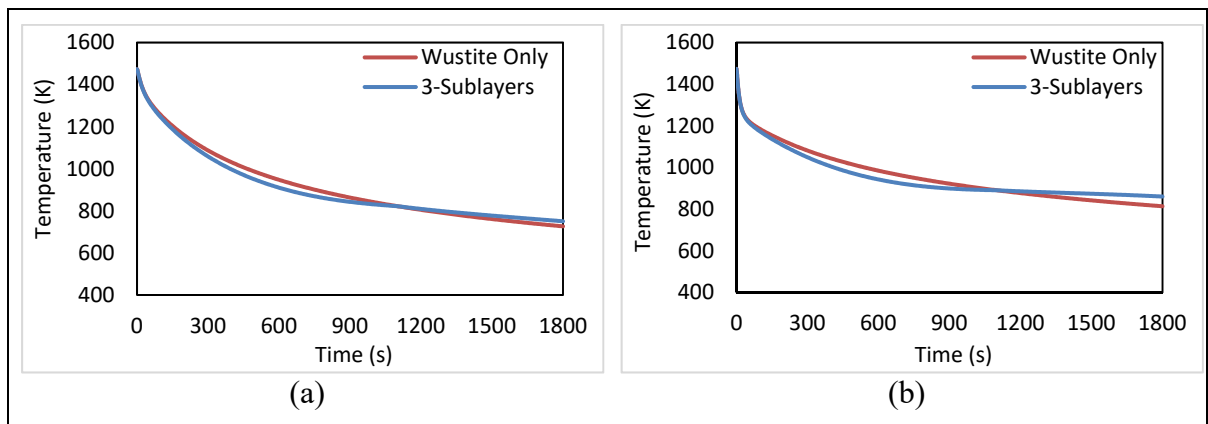
Figure 3.15 Temperature variation of the ingot with 3-oxide sublayers compared to ingot with the wustite layer only on: a) top surface, and b) bottom surface

The maximum temperature difference of the two models on the top and bottom surfaces were 42 and 46 K, respectively. Considering the initial temperature of cooling from 1473 K, the differences are about 3%, which could be considered as a negligible error. Therefore, the 3-sublayers were substituted by wustite.

To validate the reliability of the developed finite element model, an ingot was considered, which is cleaned from oxide layers after the oxidation in the furnace. In fact, in a real industrial situation, the surface of the ingot is being cleaned from oxide layers utilizing a high-pressure water jet before starting the deformation process. Hence, the oxide due to heating in the furnace is dismissed, and the mere oxide will be the one formed during cooling from 1473 K to 973 K. Still, the time steps and the activation of oxide layers for time intervals are taken into account in the calculations. The Temperature variation of the small side of the ingot is as illustrated in

Fig. 3.16. To confirm the calculated temperature by simulations on the industrial ingot, an infrared camera VarioCAM HD head 900 was utilized. The temperature was measured on the center of the small side surface of the ingot, and the outcome is given in Fig. 3.16. The maximum discrepancy between FE and experimental measurement was 69 K, which is less than 6%, confirming a reasonable agreement between the results of finite element simulations and experimental tests.

(a) (b)
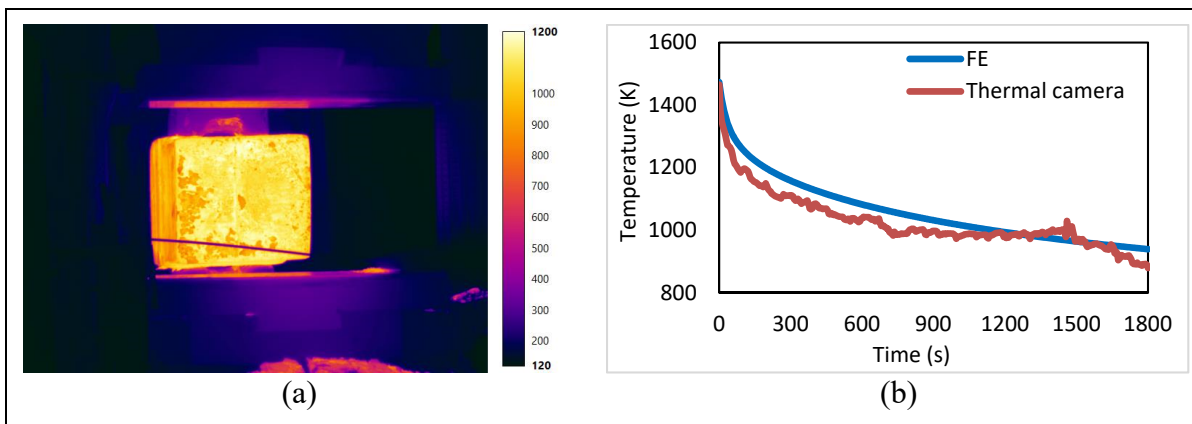
Figure 3.16 Acquired temperature variation by the thermal camera

3.4.4   The temperature variation on ingot surfaces with oxide layer

In industrial situations, two options are feasible. The oxide is continuously cleaned by a water jet before and during the deformation to keep the ingot without oxide layers, or the oxide remains intact. So, the two possibilities will be compared to observe the effect of the oxide layer on temperature variation on different surfaces of the ingot. Considering the different h-values for dissimilar surfaces, the comparison should be made on the same surface for both scenarios. Fig. 3.17 illustrates the temperature difference of oxidized ingots for 60 min, compared to ingots without oxide during cooling for different surfaces of the ingot. In other words, this figure is illustrated by subtracting the temperature curve of ingot without oxide from ingot being oxidized for 60 min to facilitate the analysis. The ingots are being oxidized and cooled from 1473, 1423, 1373, and 1273 K.

The curves are illustrated by subtracting the temperature of the oxidized ingot, at each time increment, from the ingot without oxide. The negative values demonstrate that the ingot with oxide cools down faster, despite the low conductivity of oxide, which can suppress the heat transfer to ambient. The main parameter to consider at this stage is to take into account that it is a thermal insulator due to its low conductivity. The thermal insulator is dependent on parameters such as thermal conductivity, specific heat, and the surface area of thermal contact. In fact, up to a certain amount, increasing the insulation thickness will increase the thermal loss due to increased thermal surface contact. Hence, the thermal insulator will be effective after a critical thickness is achieved, where after that amount, more insulator thickness will result in less heat loss Bahadori (2014). Furthermore, the faster cooling of an ingot with oxide is due to the high emissivity of oxide layers compared to the steel surface. The steel surfaces are vast, which makes the radiation the ruling effect on cooling, compared to the isolating effect of the oxide layer for convection.
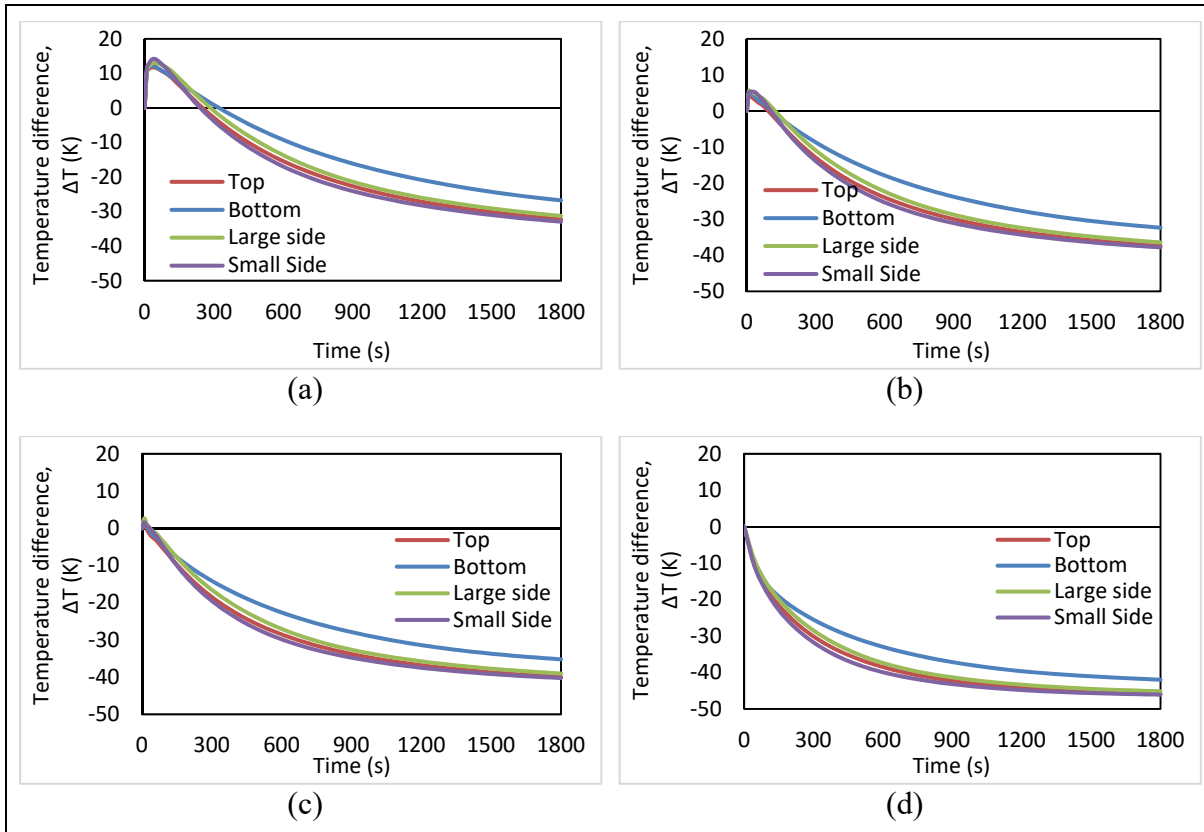
Figure 3.17 Temperature difference of oxidized ingot for 60 min, compared to ingot without oxide (subtraction of temperature curve of ingot without oxide from oxidized ingot for 60 min) at an initial temperature of: a) 1473 K, b) 1423 K, c) 1373 K, and d) 1273 K

All the surfaces of the ingot with oxide cool down faster compared to ingot without oxide. The temperature difference is lower at higher oxidation temperatures. At 1273 K oxidation, the temperature difference between ingot with oxide compared to ingot without oxide was 46 K. This difference was 40 and 37 for oxidation temperatures of 1373 and 1423 K, respectively. The lowest temperature difference was experienced for the oxidation temperature of 1473 K, at 32 K. Moreover, the temperature difference for the top, large side, and small side were close, where the bottom surface had the lowest temperature difference for all testing oxidation temperatures. The temperature difference for the small side was 46 K at 1273 K, while the bottom surface had a difference of 42 K. At oxidation temperature of 1473 K, the highest temperature difference was 32 K, but the lowest temperature difference occurred at the bottom surface as 27 K. This phenomenon can be contributed to different h-value of the bottom surface and the different area of radiation compared to side surfaces.

Moreover, the temperature difference seems to start at positive values, emphasizing that the ingot with the oxide layer started to cool down slower than the ingot without oxide at the outset, where the trend changed after sometimes. Fig. 3.18 gives the magnification of initial time steps of cooling from Fig. 3.17.
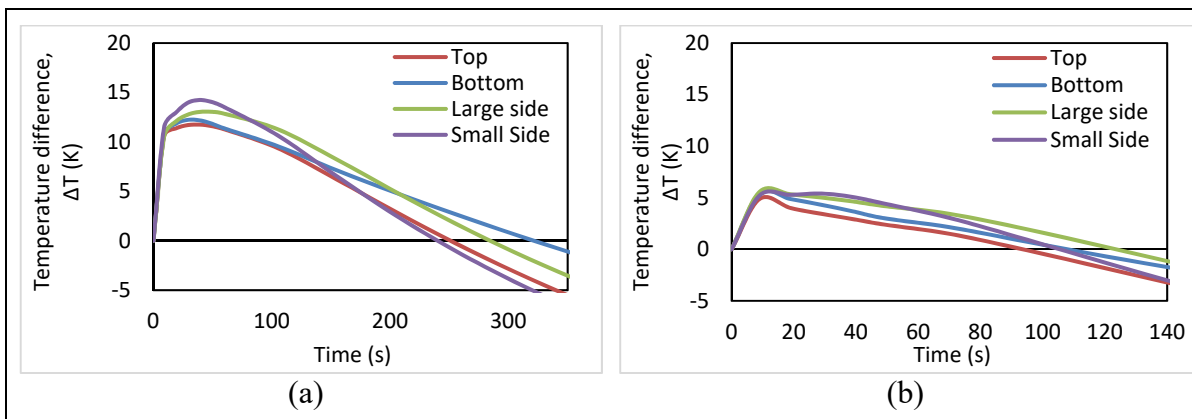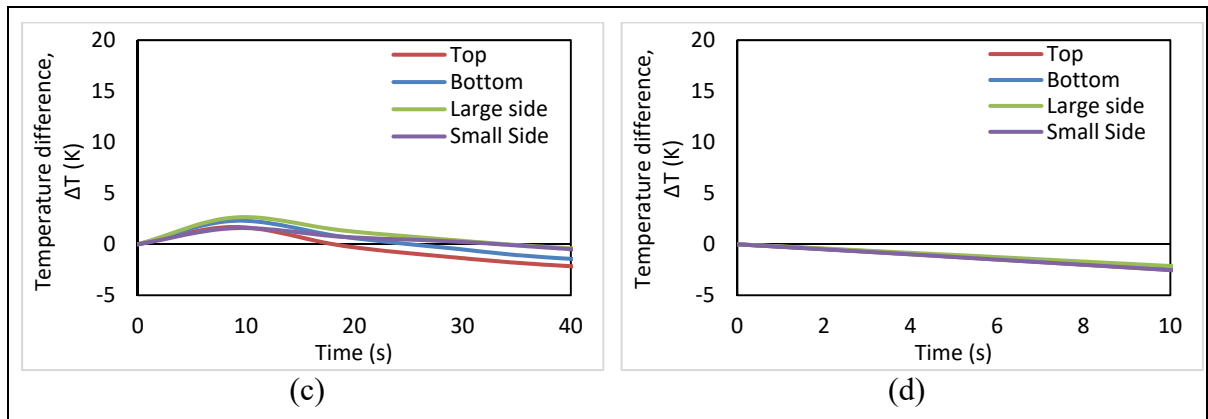
Figure 3.18 Magnification of initial seconds for temperature difference of oxidized ingot for 60 min, compared to ingot without oxide on different surfaces at: a) 1473 K, b) 1423 K, c) 1373 K, and d) 1273 K

In contrast to the general faster cooling of the ingot with oxide than ingot without oxide, the trend was inverse for initial seconds. In other words, the ingot with oxide was cooling slower compared to the ingot without oxide for commencing seconds. The heat needs to pass through the oxide barrier for radiation and convection to ambient. As it was stated before, the model is developed to simulate the oxide growth by time increments. By increasing the oxidation time, the oxide thickness increases (in each simulation time step), and time is needed for heat to pass through this thermal insulation. Afterward, the radiation by surfaces will accelerate the heat loss to ambient. When the oxidation temperature is higher, and consequently there is higher oxide thickness, the time needed to pass by thermal insulation of oxide will be higher. This time was between 300 to 350 s for different surfaces of oxidized ingot at 1473 K. It was reduced to 100 to 130 s, and 20 to 35 s, for different surfaces of oxidized ingots at 1423 and 1373 K, respectively. For oxidized ingot at 1273 K, the oxide layer was so thin that the curves never get any positive value, demonstrating the faster cooling of oxidized ingot compared to ingot without oxide for all simulation time intervals.

The illustrated curves in Fig. 3.19 show the heat flux by top surfaces of oxidized ingots at oxidations temperatures of 1473 and 1273 K, compared to ingot without oxide.
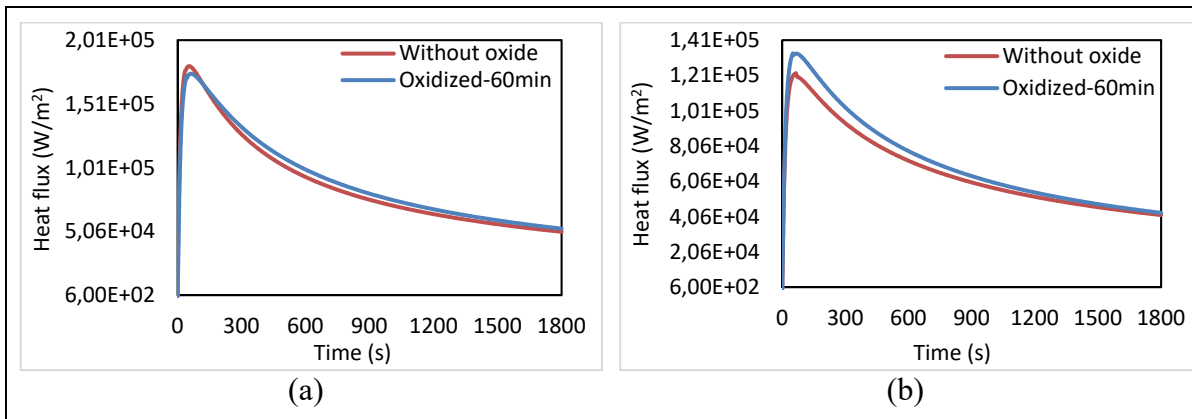
Figure 3.19 Heat flux by top surface of ingots oxidized at: a) 1473 K, and b) 1273 K

The oxidized ingot at 1473 K is cooling slower at the initial steps of cooling, which turns to lose higher heat flux after some seconds (after the peak). As discussed before, the thin oxide thickness of ingot oxidized at 1273 K does not suppress the heat loss to ambient, leading the ingot to cool down faster with oxide from the initial cooling times. The difference between heat flux of oxidized ingot and ingot without oxide tends to decrease over time as the temperature decreases. In Fig. 3.20, the heat flux curves are given with the magnification of the curves at the commencing times for ingots with oxidation temperature of 1423 and 1373 K.
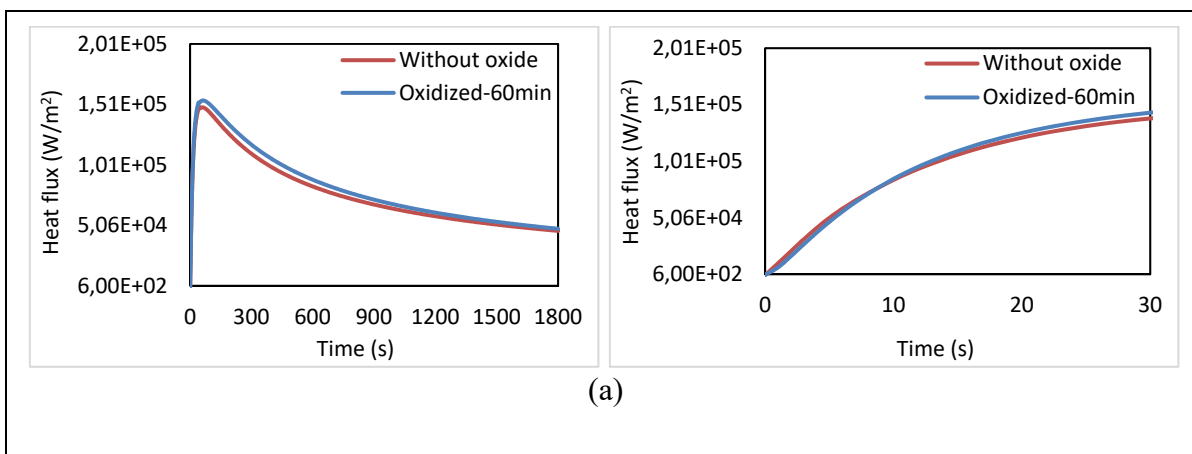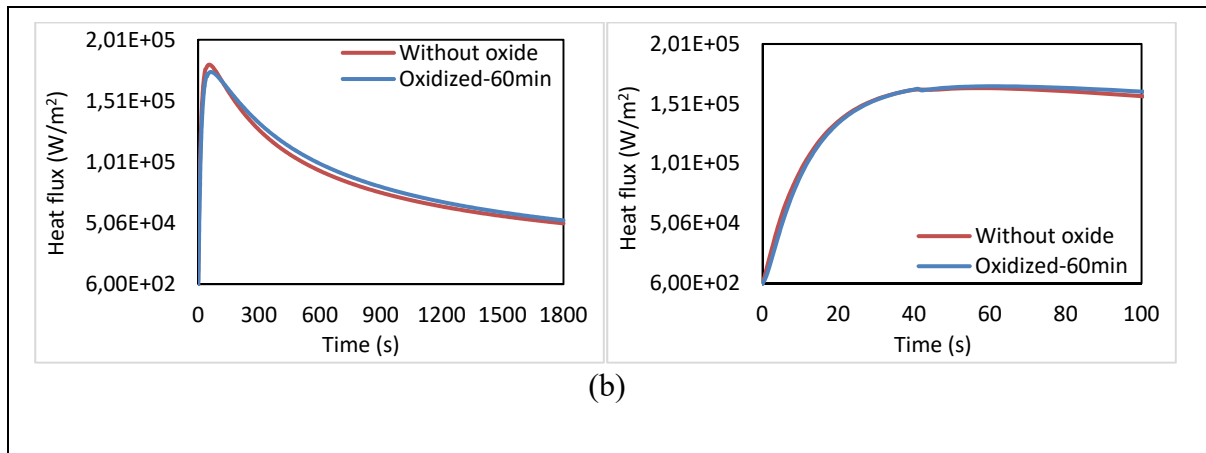
Figure 3.20 Heat flux on the top surface of ingots oxidized at: a) 1423 K, and b) 1373 K

The same behavior experienced for oxidized ingot at 1473 K was observed here for oxidized ingots at 1423 and 1373 K. However, the time that the ingot with oxide was cooling slower than the ingot without oxide decreased. Considering the overall faster cooling of the ingot with thin oxide layers, the question could be raised about the critical oxide thickness when the oxide can be effective as a thermal barrier.

3.4.5   Implementation of the verified model on an Industrial case

The employed ingot dimensions are very large and assuring a homogenous temperature distribution is time-consuming. For the industrial partner of this study, the ingots could stay for remarkable times in the furnace for that the ingot core reaches the desired deformation temperature. This process can cause excessive oxide layer thickness that can affect the temperature distribution even more. A typical case of industrial oxide is shown in Fig. 3.21.
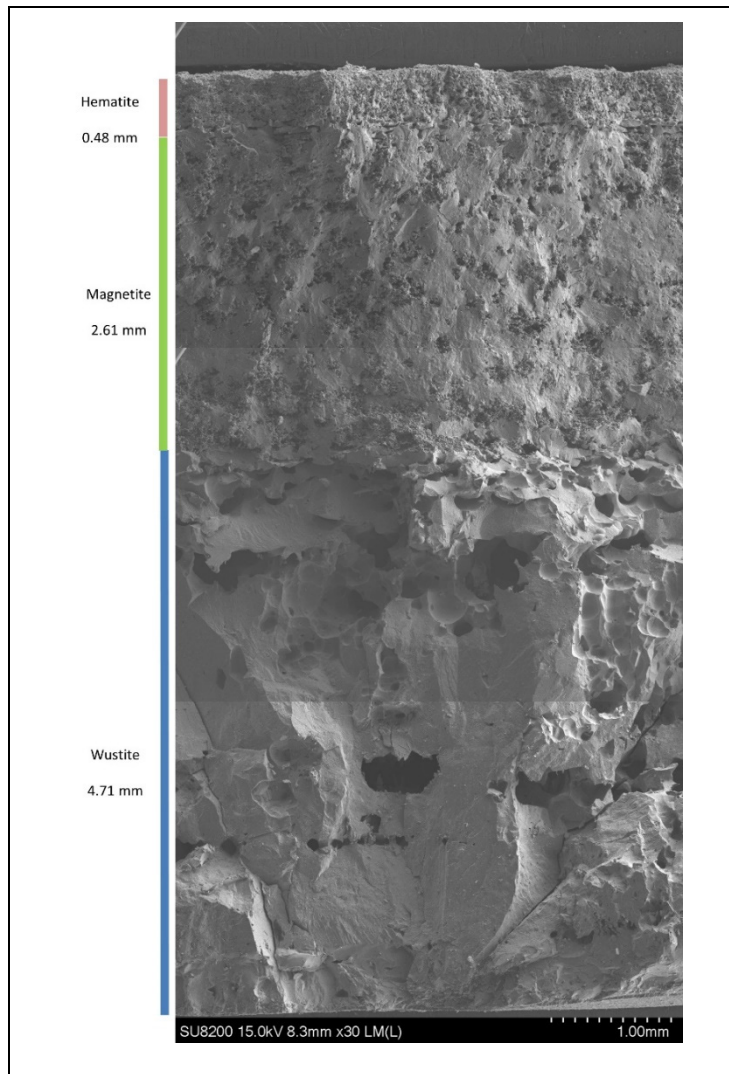
Figure 3.21 SEM of industrial oxide

This in situ oxide is 7.8 mm thick, which is almost 10 times of the oxides produced in the lab in 60 min. The material waste and effects on heat transfer situations can be remarkable by this thickness. Considering the thickness fraction of different layers, the given oxide in Fig. 3.21 causes a remarkable material waste of 855 kg. The temperature difference of this industrial ingot with oxide compared to ingot without oxide is given in Fig. 3.22 for different surfaces.
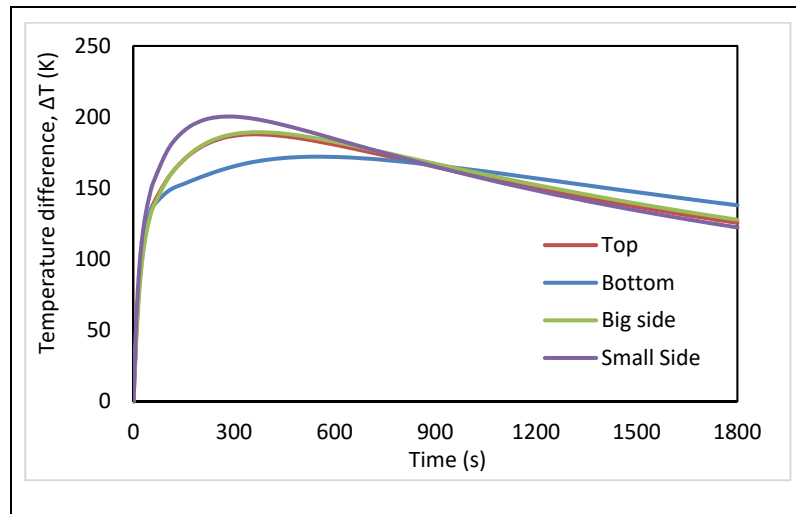
Figure 3.22 Temperature difference of oxidized ingot
in industrial furnace, compared to
ingot without oxide on different surfaces

Fig. 3.22 demonstrates the isolating effect of the oxide layer for heat transfer on ingot, as the low conductivity of oxide suppresses the heat transfer of ingot to ambient. For the small thickness of oxide, the low conductivity of oxide could not hinder the heat transfer, and the ingot with thin oxide tended to cool down faster. Despite this phenomenon, for the thick industrial oxide, the oxide can suppress the heat transfer to ambient. The temperature difference between the ingot with oxide and without oxide can reach to 187and 189 K for top and large side surfaces, in 355 s, respectively. The small side surface reaches 200 K as the highest temperature difference between all surfaces in the fastest time of 305 s. In contrast, the bottom surface has the lowest temperature difference of 172 K, which reached in 555 s. The temperature difference starts to decrease after its peak value with time, as more time realizes the heat to conduct from steel to the outer surface of oxide and then to ambient air. Fig. 3.23 gives the heat flux for the top and bottom surfaces of the oxidized ingot in the industrial furnace, compared to ingot without oxide. A remarkable discrepancy could be seen from initial stages between two ingots in both curves, where the heat flux of ingot without oxide is almost 2 times of ingot with oxide. This difference tends to diminish by time, where the heat flux of

the ingot with oxide surpasses the ingot without oxide. This is due to the higher temperature on the surface of ingot with oxide, where the oxide layers came to be effective as thermal insulators. The time that the heat flux of ingot with oxide overweight the heat flux of ingot without oxide, is longer due to different h-values and cooling rate by temperature.
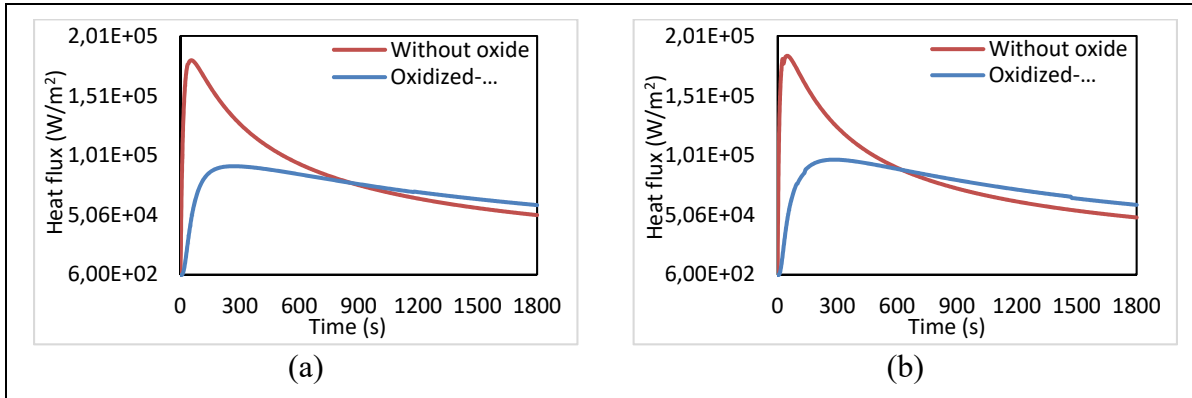
Figure 3.23 Heat flux of ingot oxidized in industrial furnace compared to
ingot without oxide for surfaces of: a) top, and b) bottom

In the second set of simulations, the ingot is in contact with the forge anvils. These simulations aim is to assess the effect of the oxide layer on the conduction between the ingot and forge anvils. The thermal camera showed the initial contact temperature of the die as 673 K. Although, the anvil temperature can be higher or lower, if the forge is being continuously conducted, or in case that the forge has just started. In these simulations, the ingots (oxidized for 60 min, and the industrial ingot with 7.8 mm oxide), are in contact with the die at 476 K. The temperature differences of oxidized ingots are obtained compared to ingot without oxide in contact with anvils. The temperature differences are acquired on the ingot surface, die surface, and a quarter of height inside the die, illustrated in Fig. 3.24. The heat flux curves of ingot surface and die surface are given in Fig. 3.25, for ingot without oxide, compared to oxidized ingots.
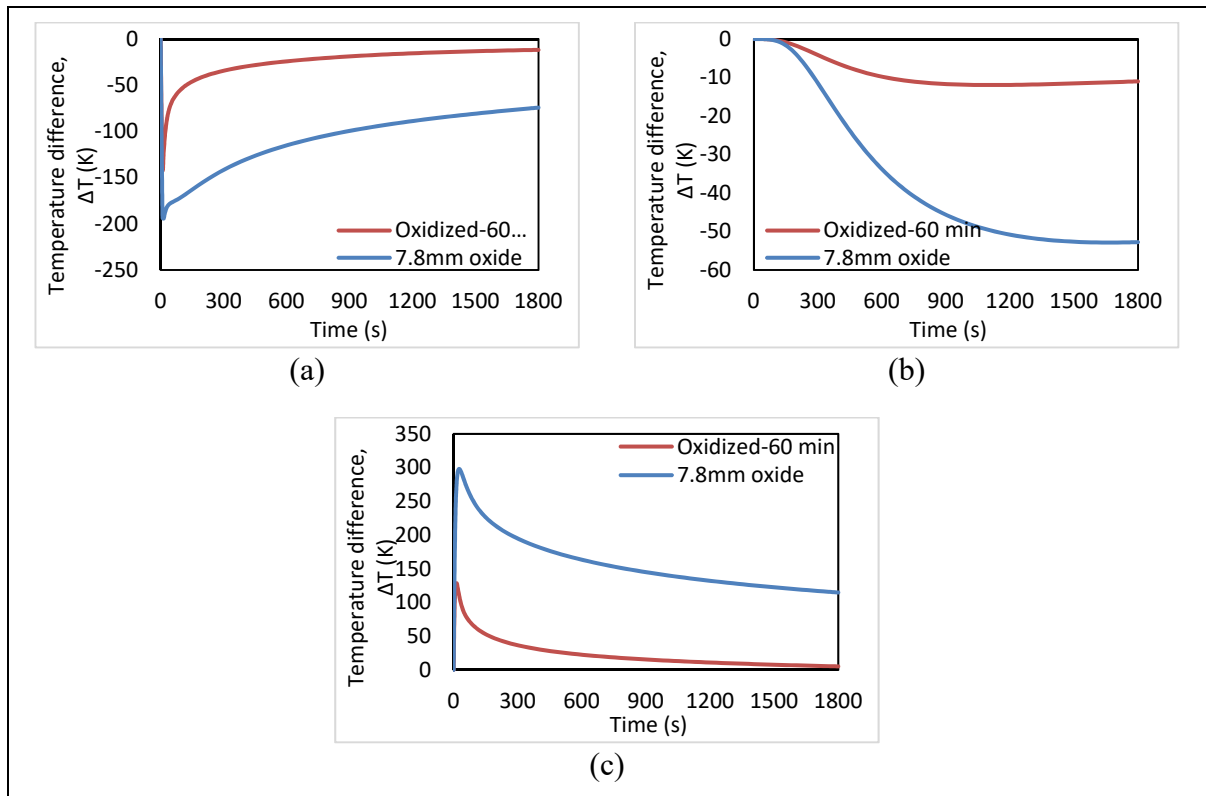
Figure 3.24 Temperature difference between oxidized ingot and ingot without oxide, being in contact with die at 673 K, on: a) die surface, b) quarter of die, and c) ingot surface

The temperature difference curves indicate that the die surface with oxide experiences 123 K less temperature increase by contacting the hot ingot compared die being in contact with ingot without oxide. This difference was 194 K for the die being in contact with ingot with industrial oxide. Not only the die surface can experience the temperature increase by hot ingot. A quarter of the height inside the die can have 11 and 53 K less temperature increase by hot ingot, compared to die contacting ingot with cleaned oxide. Moreover, the temperature drop at the ingot surface will be avoided by having the oxide between the ingot and the die. The ingot surface will be 129 and 298 K hotter, compared to ingot without oxide, which loses its surface temperature by contacting the colder anvil. The heat flux conveys the lower heat loss for die and ingot with oxide layers as the thermal insulators.
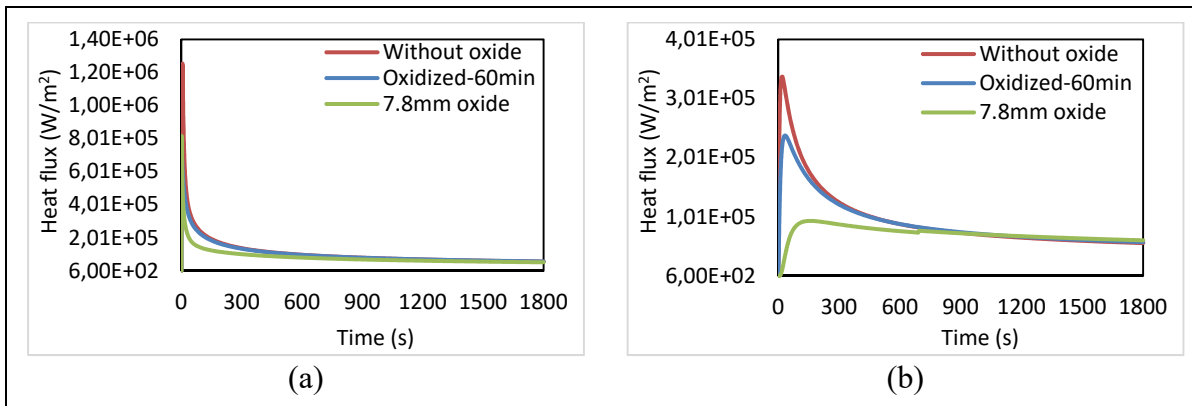
Figure 3.25 Comparison of heat flux of simulated cooling, where ingot is in contact with anvil, on: a) die surface, and b) ingot surface

To assess the effect of die temperature on the conduction between ingot and anvil with the oxide layer in between, the simulations were conducted for oxidized ingots being in contact with die at temperatures of 473, 673, and 873 K. The temperature variation on the surface of ingot and die are given in Fig. 3.26, for ingot oxidized for 60 min, and ingot with industrial oxide.

According to the illustrated curves in Fig. 3.26, in certain oxide thickness, the surface temperature of ingot and die increases by increasing the die temperature. The heat transfer of ingot and die can be predicted more precisely by this study regarding the addressed outcomes. It would be feasible to avoid undesired material characteristics in ingot and anticipate the die temperature, which is cost consuming to repair or replace.
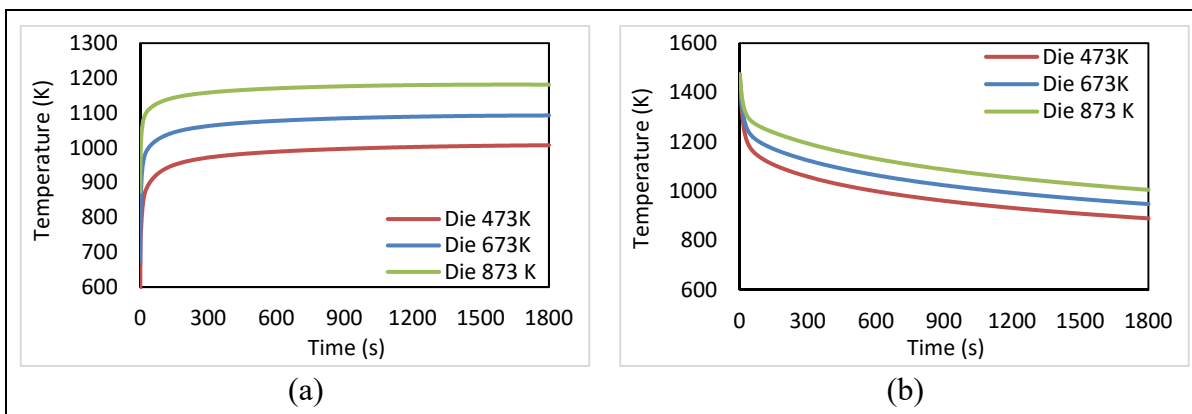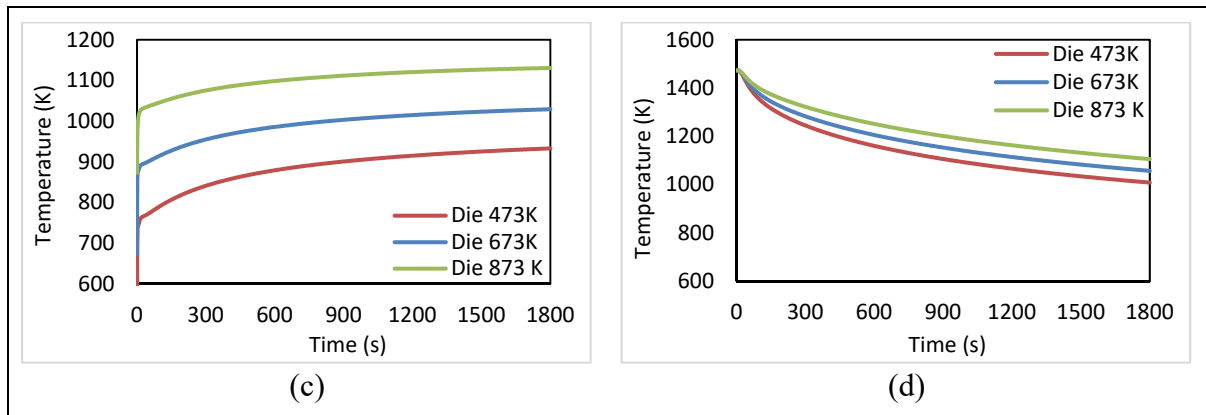
Figure 3.26 Temperature variation on the surfaces of ingot and die for different temperatures of die: a) die surface, ingot oxidized for 60 min, b) sample surface, ingot oxidized for 60 min, c) die surface, ingot with industrial oxide, and d) ingot surface, ingot with industrial oxide

3.5 Conclusions

The oxidation growth kinetics of two high-strength medium carbon steels, different in Ni concentration, were assessed employing an MTS machine with an installed radiative furnace:

1) The outcomes demonstrated a parabolic growth for both steels, which was faster at the initial steps, decreasing gradually over time. The oxide thickness increased by increasing the oxidation time and oxidation temperature for both steels. However, the oxide thickness was lower for HNi steel compared to LNi at all testing conditions.

2) The higher activation energy of HNi steel, 248 kJ.mol^{-1}, compared to 218 kJ.mol^{-1} of LNi, indicated the resistance to oxidation by additional Ni.

3) The thickness fraction of wustite increased by increasing oxidation temperature, reaching 65% to at 1473 K. In contrast, hematite decreased by increasing the oxidation temperature, reaching at 4% at 1473 K. Magnetite kept the same thickness fraction of 31% fro all the testing temperatures. The 60 min oxidation causes 101 kg of material waste, whereas the industrial oxide caused a waste of 855 kg.

4) The developed finite element model revealed that the ingot with the oxide layer was cooling faster than the ingot without oxide. This can be associated with the higher emissivity of the oxide layer compared to the steel surface.

5) The thicker industrial oxide layers came to effect as a thermal insulator, causing almost 200 K higher temperature compared to ingot without oxide. This higher temperature gradient can cause undesired material characteristics. Furthermore, the ingot with the oxide layer does not raise remarkably the temperature of the anvil. The 60 min oxidation and industrial oxidation of ingot, prevented a die temperature rise of 123 and 194 K.

3.6   Acknowledgment

3.7   Data Availability

1) The raw/processed data required to reproduce these findings cannot be shared at this time due to legal or ethical reasons.

2) The raw/processed data required to reproduce these findings cannot be shared at this time as the data also forms part of an ongoing study.

CHAPTER 4

INFLUENCE OF THERMALLY GROWN OXIDES ON INTERFACIAL FRICTION DURING HOT DEFORMATION OF LARGE-SIZE FORGING INGOTS

Ali Vedaei-Sabegh[1], Jean-Benoît Morin[2], Mohammad Jahazi[1*]

[1] École de Technologie Supérieure, Department of Mechanical Engineering, 1100 Notre-Dame Street West, Montreal, QC, H3C 1K3, Canada.
[2] Finkl Steel Inc., 100 McCarthy, Saint-Joseph-de-Sorel, QC, J3R 3M8, Canada

Abstract

High-strength steels are pre-heated in gas-fired furnaces before undergoing open-die forging process. This process increases thermal oxidation on steel surfaces which can affect the interfacial friction between ingot and anvils during deformation. In the current study, two medium carbon high-strength steels with different nickel contents were oxidized at two oxidation temperatures of 1373 and 1473 K for 10, 30, and 60 min. Microstructural characteristics of the different oxide layers were investigated by confocal laser microscopy. Micro and nano-indentation methods were used to determine the mechanical properties of the different oxide layers. It was found that the formed layers on high nickel steel had lower Young modulus and hardness compared to the steel with lower nickel. A finite element model was developed to assess oxide layers' effect on interfacial friction during deformation. Ring tests were carried out to experimentally evaluate the influence of oxide layer on deformation behavior of the alloys and to validate the developed finite element model. The results demonstrated that oxide layers' formation decreased the interfacial friction and deformation load, as the oxide layers acted as lubricants at high temperatures.

Keywords: High-temperature oxidation, oxide layer characteristics, micro-indentation, nano-indentation, ring test, FEM simulation

4.1   Introduction

Thermally grown oxides can form on most steels during hot deformation by the interaction of solid with reactive gaseous atmosphere (Birks et al., 2006). In addition to material waste and surface quality deterioration by oxidation, the interfacial condition can be influenced by scale layers. The presence of oxide can change the heat transfer between the ingot and the dies as well as the surrounding environment (Jang et al., 2010). During deformation, the oxide layers can detach and break into the ingot, causing cracking (Utsunomiya et al., 2009). Also, friction and wear between the ingot and the dies can be affected by the presence of oxides, thereby, decreasing their useful service time (Barrau et al., 2003).

To form the oxide layers, the Fe ions must diffuse outward the surface. The oxidation kinetics is influenced by the diffusion of Fe ions (Fe^{2+} and Fe^{3+}) and inward diffusion of oxygen anions (O_2^-) (Suárez et al., 2010). Temperature and time are two factors increasing the diffusion of Fe and oxygen and therefore increasing the kinetics of oxidation (Munther & Lenard, 1999). The thermally grown oxide on pure iron is comprised of three layers: wustite (FeO), magnetite (Fe_3O_4), and hematite (Fe_2O_3) (Suarez et al., 2009). Wustite is the first layer, closest to the base metal, with the lowest hardness between all scale layers. Hematite has the highest hardness, causing wear on contacting surfaces. Magnetite has an intermediate hardness compared to the two other layers (Zambrano et al., 2015). The chemical composition of the alloy, oxidation atmosphere, oxidation time, and oxidation temperature all influence the diffusion of Fe and oxygen and therefore the thickness of the different scale layers (Birks et al., 2006).

For oxidation of low carbon steel at 1073-1423 K, Abuluwefa et al. (HT Abuluwefa et al., 1997) observed all three scale layers by oxidation in pure oxygen. However, only a single wustite layer was found for the oxidation of the same steel in the water vapor atmosphere. Si was found to decrease the oxidation of low alloy steel below 1450 K by Mouayd et al. (Mouayd

et al., 2014). Takeda et al. (Takeda et al., 2010), reported that Cr decreased the oxidation kinetics of low carbon steels by forming a $FeOCr_2O_4$ layer at the oxide-metal interface. Webler et al. (B. Webler et al., 2008) found that the addition of 0.3Cu + 0.1Ni decreased pure iron oxidation. Yin et al. (L. Yin et al., 2010) assessed Fe-Cu-Ni alloys' oxidation at 1423K, where Ni increased the oxidation resistance. In a recent study, the effect of Ni on high temperature oxidation of high-strength steels was evaluated by Vedaei et al. (Vedaei-Sabegh et al., 2020). The results showed a remarkable decrease in oxidation kinetics by adding Ni. However, the impact of the oxide layers on interfacial friction during high temperature deformation was not studied. Such evaluation would require accurate determination of the mechanical properties of the oxide layers.

Considering each oxide layer's different characteristics, the friction and wear conditions can be remarkably affected at the die-ingot interface. Methods like ring test and pin on disk, can be employed to investigate the oxide layer's effect on the friction between the die and the ingot. Ashimabha et al. (Ashimabha et al., 2018) investigated the friction of 316L stainless steel using ring compression test in dry deformation condition. The rings were deformed in the temperature range of 1173 to 1473 K, without considering the effect of thermal oxidation on interfacial friction. The authors reported a higher friction at 1173K and smaller at 1473K and associated the obtained results to changes in different degrees of thermal softening and material flowability with temperature. Munther and Lenard (Munther & Lenard, 1999) assessed the effect of oxide layers on the interfacial friction during rolling of AISI 1018 steel and reported that the friction coefficient decreased by increasing the oxide thickness with the highest friction for 0.015 mm of scale and the lowest for 1.01 mm. Employing high temperature pin on disc method, Vergne et al. (Vergne, Boher, Gras, & Levaillant, 2006) investigated the effect of oxidation on friction of a AISI 1018 disc with a cast iron pin. It was found that oxidation at 1223 K for 1 h decreased both interfacial friction and wear. Graf et al. (Graf et al., 2018) used ring compression tests at 1173 and 1273 K for evaluation of friction and deformation load of C15 steel and reported that the presence of 30 and 50 μm of scale layers remarkably decreased the friction and deformation load of rings. Hardell et al. (Hardell et al., 2015) employed pin on disc to assess the influence of oxide formation

on interfacial friction between two steels. It was found that the formation of higher amounts of magnetite layers at 673 K decreased the friction and wear rate between contacting surfaces. Odabas (Odabas, 2018) investigated the dry sliding friction between AISI 3315 Steel against AISI 3150 Steel with pin on ring method. They reported lower interfacial friction on samples submitted to higher loads or sliding speeds and related their findings to higher temperatures at the surface, and hence oxidation, of such samples. Matsumoto et al. (Matsumoto, Osumi, et al., 2014) used ring compression tests to investigate the oxide layer's effect on the deformation of Cr rich steels at 1273 K and concluded that the presence of oxide layers with thickness in the range of 6-300 μm resulted in reduced deformation loads. However, in their simulations, the oxide layer was considered as a single layer of wustite and very little microstructure analysis of the oxide material behavior was carried out.

The above studies show that the formation of thermal oxides reduces the interfacial friction during deformation. Therefore, accurate quantification of the impact of oxide layers requires a more precise determination of the mechanical and morphological characteristics of different oxide layers as a function of process parameters such as oxidation temperature, oxidation time, initial composition, or oxidation atmosphere. The evaluation of the above characteristics of *different* oxide layers and their different effects on interfacial friction is a critical information that needs to be determined for accurate prediction of the friction coefficient. To acquire the mechanical properties of the different oxide layers, tensile or compression tests could be employed. However, these methods need molds, machining, furnaces, and difficult sample preparations that makes them time consuming and costly. Micro and nano-indention methods are prevalent methods to investigate thin films and coatings and more convenient to conduct compared to compression tests. However, micro and nano-indentation test results are very sensitive to small variations in oxidation temperature, oxidation time, oxidation atmosphere or initial composition. For instance, Takeda et al. (Takeda et al., 2009) measured at room temperature the hardness of formed oxide layers on pure iron at 1273 K. The Vickers hardness for wustite, magnetite, and hematite was 3.5, 4, and 6.7 GPa, respectively. On the other hand, Barrau et al. (Barrau et al., 2002) reported different hardness values, 2.64–2.94, 4.2–4.9, and

10.1 GPa for wustite, magnetite, and hematite layers formed on iron, respectively. Luong and Heijkoop (Luong & Heijkoop, 1981) obtained 4.6, 5.3, and 10.3 GPa for the three oxide layers formed on AISI 1340 steel oxidized at 1423±20 K in air. Amano et al. (Amano et al., 2006) reported 3.5, 3.9, and 7.2 GPa values for the hardness of wustite, magnetite, and hematite formed on Fe-0.5Si alloys at 1273 K for 18 ks in air and measured at room temperature. Zambrano et al. (Zambrano et al., 2015) investigated the hardness of different oxide layers formed at 1473 K in air on a low carbon steel and obtained hardness values of 5.5±1.1, 6.5±0.9, and 12±2.5 GPa for wustite, magnetite, and hematite layers at room temperature. Finally, Hutchings and Shipway (Hutchings & Shipway, 2017) reported a hardness range of 3.6 to 5.9 GPa for magnetite, for different oxidation conditions. The above studies reveal that the initial composition has a significant influence on the characteristics of each oxide layers and therefore the need for conducting indentation tests for each specific steel. Finally, it must be noted that one of the factors that could also influence the reported results is the measurement technique (i.e., nano-indentation or micro-indentation), as evidence by results reported by Chicot et al. (Chicot et al., 2011) and Seo and Chiba (Seo & Chiba, 2001) on magnetite hardness values. Therefore, in the present study, both nano indentations and micro indentation techniques were used in order to ensure the accuracy of the obtained mechanical characteristics of the thermal oxides

Although the indicated analysis shows impacts of oxide layers on friction between die and ingot, very little information is available on the specific roles of each oxide layer and the evolution of its morphological and mechanical properties as a function of oxidation parameters. The aim of the present study is to investigate the characteristics of each oxide layer and assess the effect of oxidation on interfacial friction between ingot and anvil during open-die forging. In this regard, oxidation experiments were carried out on two different high-strength steels at different temperatures and the mechanical properties of each oxide layer was assessed employing micro and nano-indentation tests. The results were then employed as input for finite element simulations to evaluate oxide layers' effect on the interfacial friction between anvils and ingot using high temperature ring tests to simulate the open die forging process.

4.2 Materials and methods

Two high-strength medium carbon low alloy steels were used in the present study. One of the sub-objectives of the project was to evaluate the impact of a higher Ni content on the oxidation behavior of large size components during open die forging and therefore a higher Ni content was employed, as shown in table 4.1. For ease of use, the steels are identified as low nickel (LNi) and the high nickel (HNi). The materials were provided by Finkl steel, Sorel, Quebec, Canada and were obtained from large size forgings used in energy and transportation industries.

Table 4.1 Chemical composition of employed steels (wt%).

	C	Mn	Si	Ni	Cr	Mo	Cu
LNi	0.35	0.99	0.41	0.5	1.86	0.53	0.16
HNi	0.35	0.99	0.41	2.92	1.86	0.53	0.16

4.2.1 Oxidation experiments

Samples for the oxidation experiments were cylinders with 10 mm diameter and 15 mm height. Before oxidation experiments, the samples were grounded by 320 mesh SiC papers, to achieve similar surface roughness, and ultrasonically cleaned and kept in the vacuum chamber. The oxidation tests were conducted employing a radiative furnace mounted on a Material Testing System (MTS), serie 809. The furnace was a water-cooled IR E4 Research Inc. radiative type and was equipped with four lamps and elliptical polished aluminum reflectors that provided the infrared radiation and produced a hot zone with uniform temperature over a 100 mm distance thereby, producing uniform temperature conditions all around the samples. . Samples were heated to an oxidation temperature of 1473 K with a heating rate of 2 K/s. The heating was conducted under the protection of argon gas with a flow rate of 50 ml.min^{-1} to avoid oxidation during heating. At this temperature, the argon was switched off for 60 min, leaving the sample to oxidize in the air. Then, the argon flow was connected again to cool down the sample to room temperature and avoid oxidation during cooling. The formed scale layers are

fragile, and therefore need to be carefully preserved for metallography, indentation, and microscopy. A method was developed to guard the scale layers from manipulation damages. This consisted in using a cold mounting product composed of 60 - 70% Zirconium oxide, 20 - 40% fused Silica and 0- 10%Aluminum oxide with a hardener composed of Amines, polyethylenepoly, and triethylenetetramine and introduced to the oxidized sample in a vacuum chamber.

4.2.2   Indentation on oxide layers

To evaluate the material properties of different scale layers, indentation tests were conducted. Micro-indentation tests were conducted using an Anton Paar Micro-Hardness Tester (MHT), and nano-indentation tests were carried out with Micromaterials NanoTest Vantage. For both tests a Vickers diamond indenter was used on the transverse-section of oxide layers. Before nano-indentation, the sample were placed in the machine chamber for 48 hours to ensure temperature homogeneity. The diamond tip was applied to the examination point up to a specific load during the indentation where it was kept for 30 s, followed by unloading (Fischer-Cripps, 2011). The output of an indentation test is a curve showing the applied load versus the indentation depth. The contact depth of the indenter, h_c, was calculated using the Oliver and Pharr analysis (Warren Carl Oliver & Pharr, 1992; Warren C Oliver & Pharr, 2004):

$$h_c = h_m - \varepsilon \frac{F_m}{S}$$

(4.1)

where h_m is the maximum indentation depth (µm), ε is a constant related to the indenter geometry, F_m the maximum normal load (mN), and S is the stiffness of the sample (mN/µm) acquired from the slope of the unloading portion of the indentation curve. In the unloading part of the graph, the instrumented hardness of the tested material, H_{IT}, can be obtained using equation 4.2 (Warren Carl Oliver & Pharr, 1992; Warren C Oliver & Pharr, 2004):

$$H_{IT} = \frac{F_m}{A_p}$$

(4.2)

where A_p is the contact area between the indenter and the specimen at the maximum depth and load (µm²). Reduced elastic modulus, E_r (GPa), considers that the elastic displacement occurs in both indenter and sample and can be obtained as follows (Warren Carl Oliver & Pharr, 1992; Warren C Oliver & Pharr, 2004):

$$E_r = \frac{\sqrt{\pi}}{2\beta} \frac{S}{\sqrt{A_p}}$$

(4.3)

where β is a geometrical constant on the order of unity. The instrumented elastic modulus in the specimen, E_{IT}, is acquired as follows (Warren Carl Oliver & Pharr, 1992; Warren C Oliver & Pharr, 2004):

$$\frac{1}{E_r} = \frac{(1 - v_s^2)}{E_{IT}} + \frac{(1 - v_i^2)}{E_i}$$

(4.4)

where v_s is the Poisson's ratio of specimen and E_i and v_i are the elastic modulus and Poisson's ratio of the indenter, which for a Vickers indenter are 1141 GPa and 0.07.

4.2.3   Hot compression tests

To obtain the stress-strain behavior of the studied materials for friction assessment, hot compression tests were conducted. Cylindrical samples 10 mm diameter and 15 mm height were heated to 1373 and 1473 K under argon protection to avoid oxidation and compressed to 50% of their height. The strain rate was 0.25 s^{-1}. To minimize the effect of friction on results, graphite powder and mica sheets were placed between the sample and the anvils. However, a slight barreling was still observed, indicating, the presence of some friction during compression testing. The stress-strain curves were therefore corrected for this frictional effect

to ensure accurate evaluation of the material mechanical behavior during high temperature deformation. The instantaneous friction was calculated as follows (Y. Li, Onodera, Matsumoto, & Chiba, 2009):

$$\mu = \mu_0 + A \exp(\frac{\varepsilon}{\varepsilon_0})$$

(4.5)

where μ_0, A, and ε_0 are constants and are given in Table 4.2 for different temperatures based on empirical investigations (Y. Li et al., 2009). Using equation 4.5 and the data in Table 4.2, the friction related to the deformation can be corrected as follows (Y. Li et al., 2009):

$$\sigma = \frac{C^2 P}{2[\exp(C) - C - 1]}$$

(4.6)

$$C = \frac{2\mu r}{h}$$

(4.7)

where P is the acquired stress from the testing device, r and h are the specimen's initial radius and height.

4.2.4   Hot ring compression test for friction assessment

Rings with dimensions of 18 mm for outer diameter, 9 mm inner diameter, and 6mm height were machined from the as received materials. These rings were heated to deformation temperatures of 1373 and 1473 K and isothermally deformed to 50% of their height. The variation of the ring inner diameter with the height reduction can be be correlated with the friction at the die-part interface (Sofuoglu, Gedikli, & Rasty, 2001). If the friction is low, the ring will flow outwards, causing the inner diameter to increase. If the friction is high, the material will flow inward, and the inner diameter will decrease.

The rings were oxidized before deformation to evaluate thermal oxidation's effect on the interfacial friction during deformation. Before compression testing, the rings were hung with

the help of a support inside the furnace to allow both parallel surfaces of the sample to be in contact with the air and be oxidized by the indicated procedure in section 2.1. Two oxidation temperatures, 1373 and 1473 K and three oxidation times, 10, 30, and 60 min were used to assess the influence of different oxide thickness on interfacial friction.

4.3   Finite element modeling of the ring test

Friction calibration curves (FCC), as reported in the literature (Sofuoglu et al., 2001), have been widely employed to estimate the friction coefficient by obtaining the variation of inner diameter for a specific height reduction. However, the studies have demonstrated that the FCCs can be remarkably different for various materials, deformation temperature, heat transfer, ring geometry, etc. (Sofuoglu et al., 2001). In other words, utilization of conventional FCCs cannot be a precise approach for all investigations. On the other hand, experimental determination of FCC for all the experimental conditions encountered in real deformation processing conditions is a very time consuming exercise; hence, finite element (FE) with Abaqus/CAE software was used to develop each of the investigated steels' FCC. Due to the axisymmetric nature of the ring-compression test, a 2D axisymmetric model was developed. Furthermore, because of the planar symmetry during compression, half of the ring's cross-section was considered in the simulations which further reduced the computational time during the simulations. The die was considered as a non-deformable discrete rigid with 2-node linear axisymmetric rigid elements (RAX2). The ring was modeled as deformable elastic-plastic with 4-node bilinear axisymmetric quadrilateral mesh (CAX4R) for axisymmetric stress. The mechanical properties were acquired by the cylindrical compression tests. Rings were deformed up to 60% of the height. Fig. 4.1 shows the employed mesh and deformation of the LNi ring at 1473 K. The die temperature was considered the same as ring, as the temperature is uniform for 100 mm length inside radiative furnace. The ring could deform in both horizontal and vertical directions, whereas the die had the freedom to only move in vertical direction.
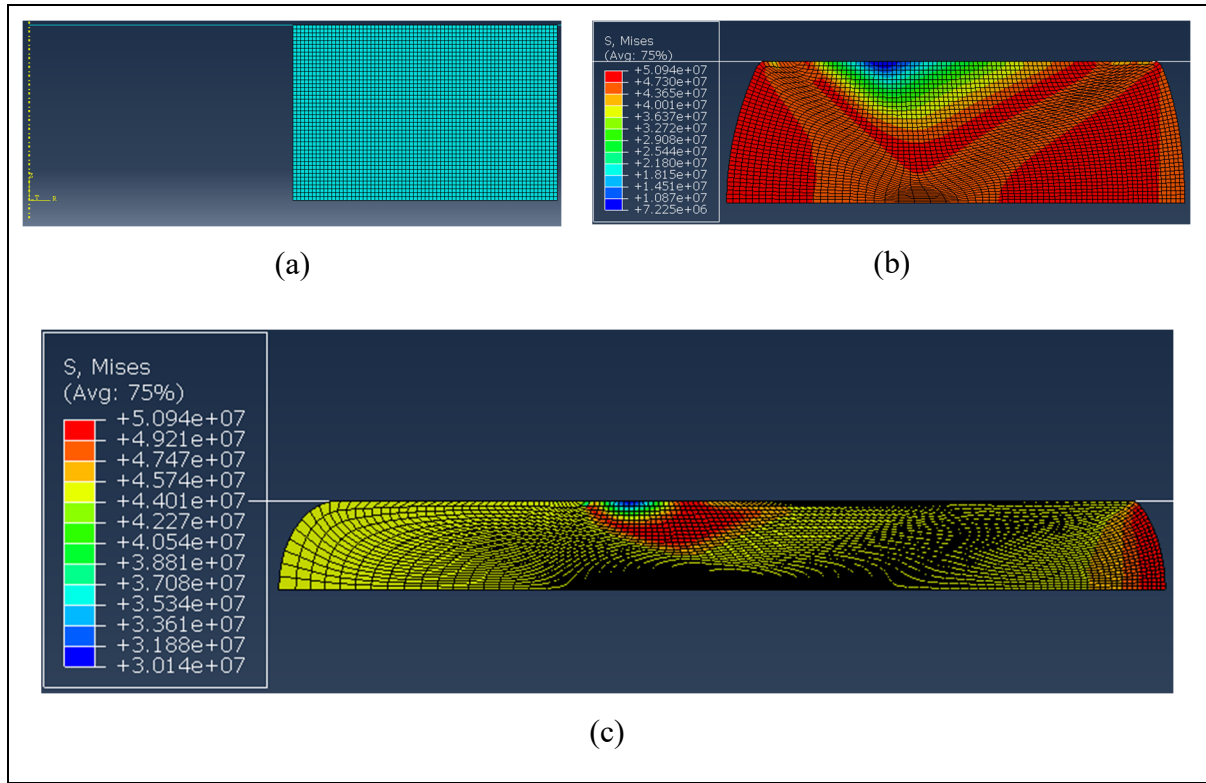
Figure 4.1 a) developed FE model, b) 45% compression of LNi ring at 1473 K, and c) 60% compression of LNi ring at 1473 K.

The two common friction models utilized in metal forming to describe the frictional conditions of contacting surfaces are the Coulomb friction model and constant shear friction law (Kobayashi, Kobayashi, Oh, & Altan, 1989). These models can be indicated as follows (Avitzur, 1964; Zhu et al., 2011):

$$\tau = \mu P \qquad \text{(Coulomb friction model)} \qquad (4.8)$$

$$\tau = mK, K = \frac{\sigma_s}{\sqrt{3}} \qquad \text{(Constant shear friction law)} \qquad (4.9)$$

where τ, μ, P, m, and σ_s are frictional shear stress, friction coefficient, normal stress, shear friction factor, and effective flow stress (Avitzur, 1964; Zhu et al., 2011). The FCCs in this study are developed by both models to understand better and compare two friction models.

4.4   Results and discussion

4.4.1   Micro-indentation and nano-indentation on oxide layers

Fig. 4.2 shows the formed oxide layers on LNi and HNi steel at 1473 K for 60 min. The three oxide layers of hematite at the top, magnetite as intermediary layer, and wustite at the bottom can be seen for both steels. The formed scale layers on HNi are thinner compared to LNi steel, as Ni suppressed the oxidation. The mechanism by which Ni hinders the oxidation was discussed in a former study (Vedaei-Sabegh et al., 2020). The formed thermal oxide on HNi steel is continuous and smooth, compared to rough and porous layers of LNi ones, particularly for the magnetite layer. Furthermore, the interface of oxide-metal for grown oxide layers on HNi steel is thicker, which shows the better adhesion of this scale to the base metal compared to LNi one. Despite the presence of pores and cracks during sample preparation, still there was sufficient room to properly conduct indentation tests.

The Vickers micro indenter was applied to different oxide layers, as shown in Fig. 4.3. The indenter was applied with different loads, hold for 30 s at peak load, followed by unloading as illustrated in Fig. 4.4-a for wustite formed on LNi steel. The evolution of the penetration depth as a function of time is shown in Fig. 4.4-b.
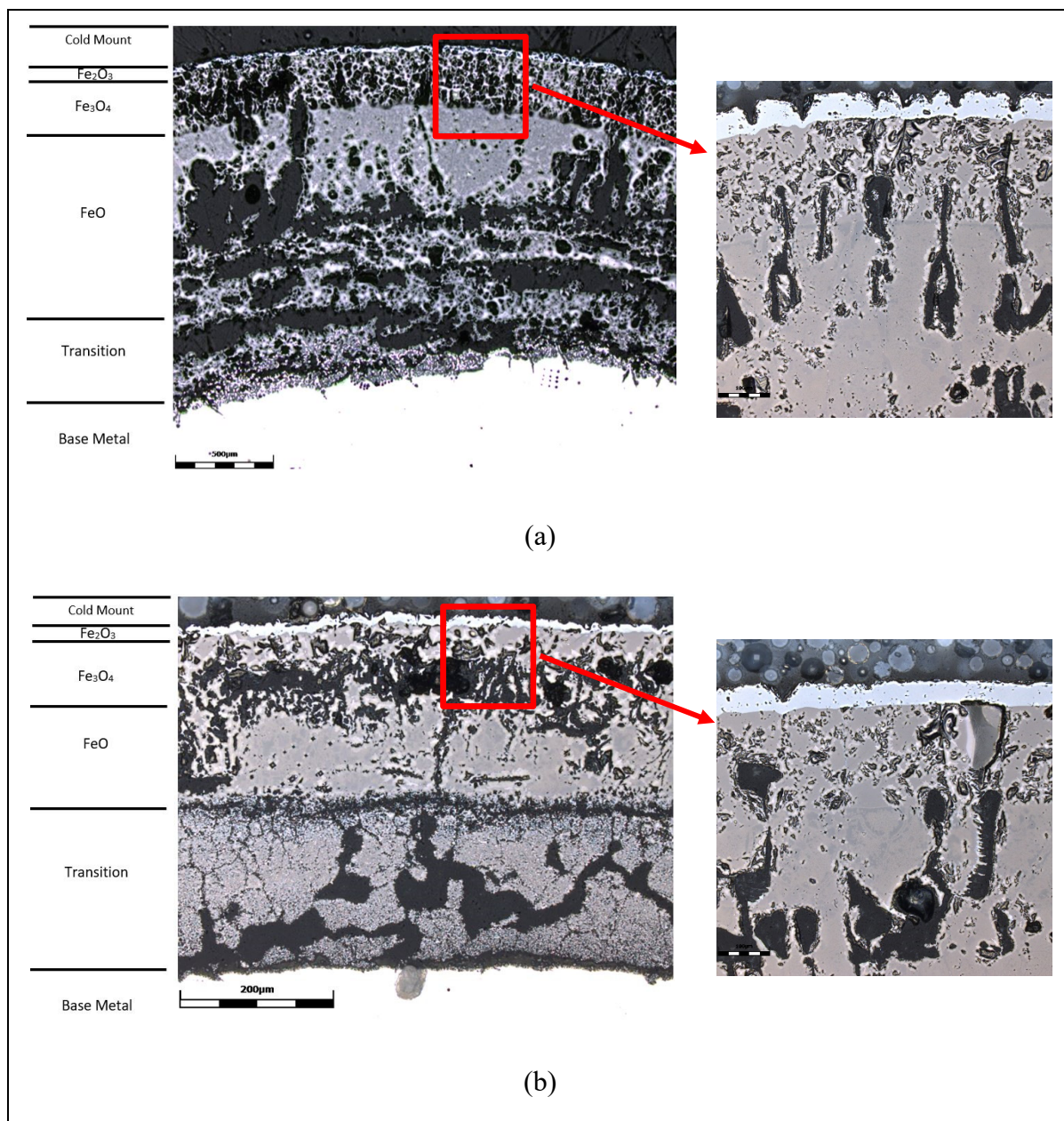
Figure 4.2 Formed thermal oxide layers on: a) LNI steel, 1473 K, 60 min, and b) HNI steel, 1473 K, 60 min.
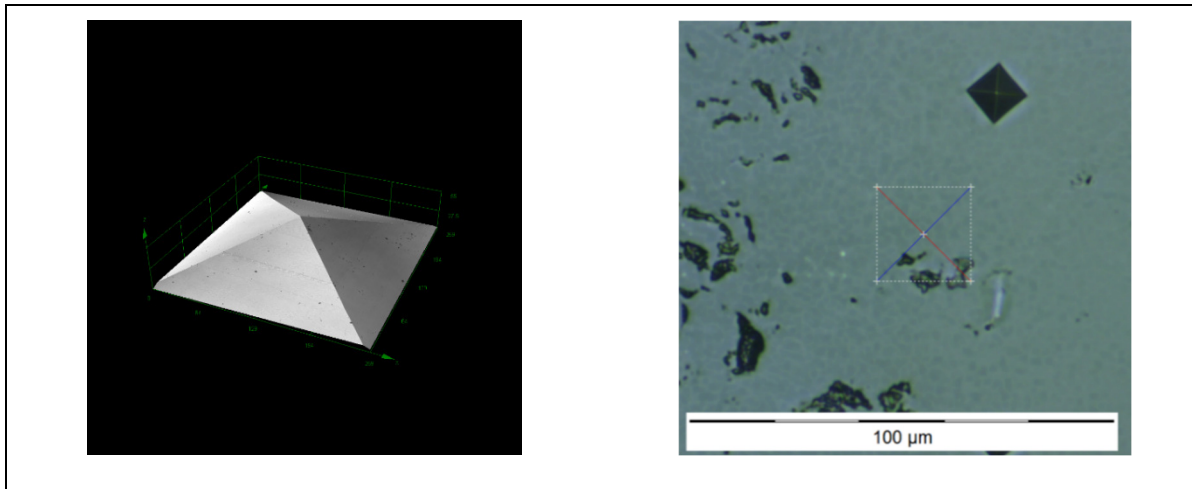
Figure 4.3 The Vickers indenter tip and the imprint of indenter on the oxide layer.
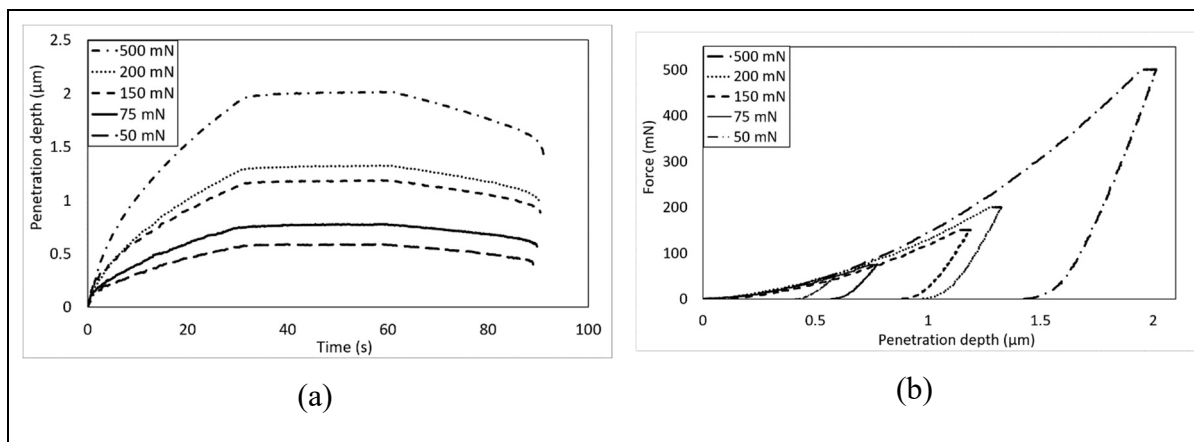
Figure 4.4 Indentation on wustite formed on LNi steel: a) penetration depth by time, and b) different applied loading cycle.

Employing Fig. 4.4 and equations 4.1 to 4.4, the Young modulus and hardness of different oxide layers were determined according to Oliver and Pharr's method (Warren Carl Oliver & Pharr, 1992; Warren C Oliver & Pharr, 2004). The results for the wustite layer of both steels are given in Fig. 4.5. The results reveal that the average Young modulus of wustite formed on LNi steel and acquired with micro-indentation was 141 GPa while the one for the HNi steel was remarkably lower, at 100 GPa. It is interesting to note that the Young modulus's results

obtained from nano-indentation of the LNi sample are very close to the ones obtained by micro indentation (145.5 GPa). This finding indicates the reliability of the less demanding micro-indentation technique as compared to the more complex experimental set-up of the nano-indentation one for characterizing oxide layers.

Figure 4.5 The indentation results on wustite layer: a) elastic modulus, b) hardness, c) stiffness, and d) conducted work.

The hardness of wustite on LNi was determined to be 6 GPa by both micro and nano-indentation techniques, further confirming the reliability of measures with micro-indentation technique. It is also interesting to note that the hardness of the wustite layer on the HNi steel was about 3.7 GPa which is much softer than the one in measured in the LNi steel. The results also show that the stiffness of wustite increases by increasing the applied load or penetration depth. The elastic-plastic work conducted to penetrate both wustite layers on steels was equal

to %26 and %74 for elastic work and plastic work, respectively. In agreement with the Young modulus results the stiffness of the wustite for LNi steel was higher compared to the one for the HNi steel.

Figure 4.6 The indentation results on magnetite layer: a) elastic modulus, b) hardness, c) stiffness, and d) conducted work.

The results for the magnetite layer are illustrated in Fig. 4.6. The average elastic modulus of magnetite layer acquired by micro-indentation and nano-indentation were 160 and 162 GPa, respectively. A lower value of 143 GPa was measured for the Young modulus for the magnetite layer grown on HNi steel. The same trend was observed for hardness as the hardness of magnetite on LNi was 6 GPa compared to 5 GPa of hardness for the layer on HNi steel. The stiffness for formed magnetite on LNi was slightly higher compared to the one on HNi. Still,

the same percentage of %26 and %74 was observed for elastic and plastic work of both steels' magnetite.

Fig. 4.7 gives the results for the outermost layer, hematite. The Young modulus reached 236 and 239 GPa acquired by micro and nano-indentation, further confirming the agreement between the measures made by both techniques. This value was remarkably lower at 195 GPa for hematite of HNi steel. The same trend was observed for hardness as it was 11 and 13.7 GPa for LNi compared to 8.8 GPa for HNi one. Like the magnetite layer, LNi hematite's stiffness was slightly higher than grown hematite on HNi steel. The ratio of elastic and plastic work was different from the previous two layers, equaling %42 and %58, respectively.

(a)

(b)

(c)

(d)
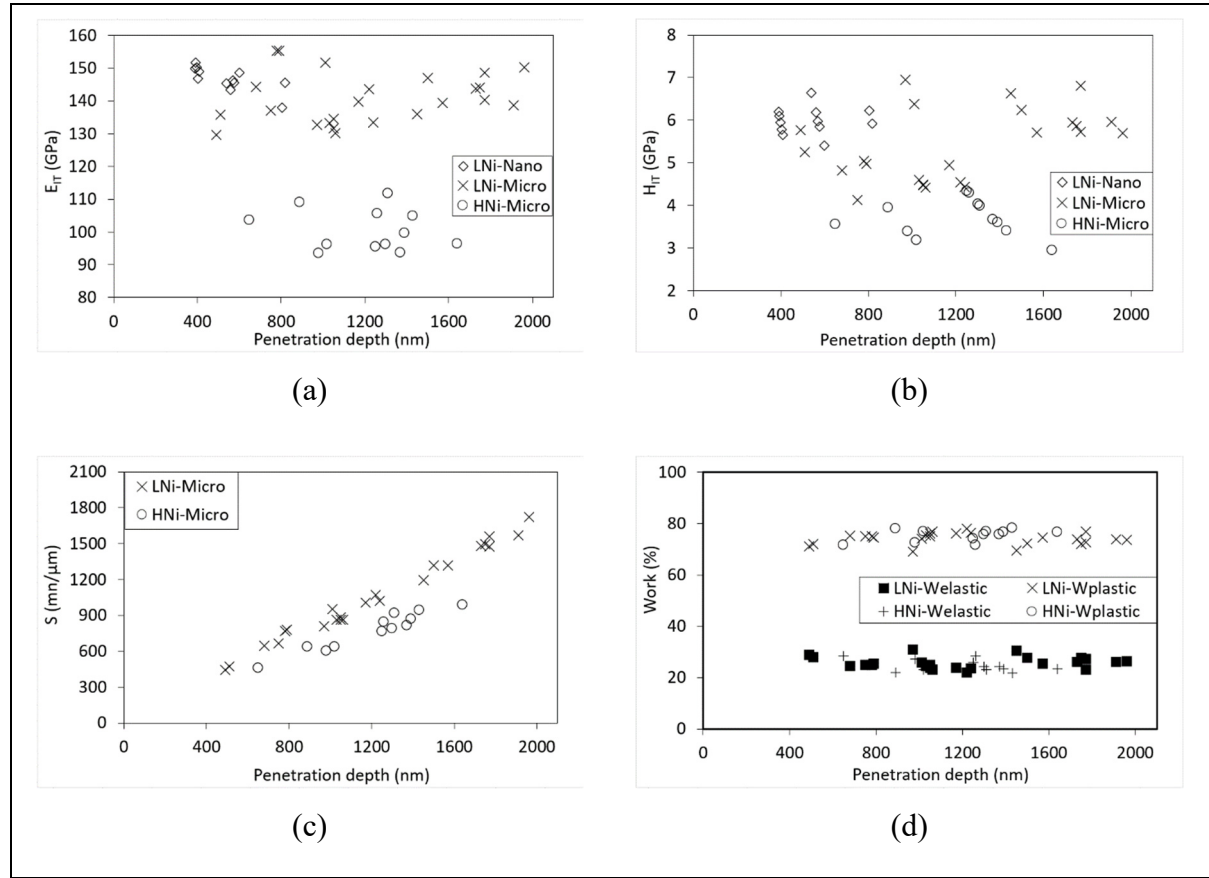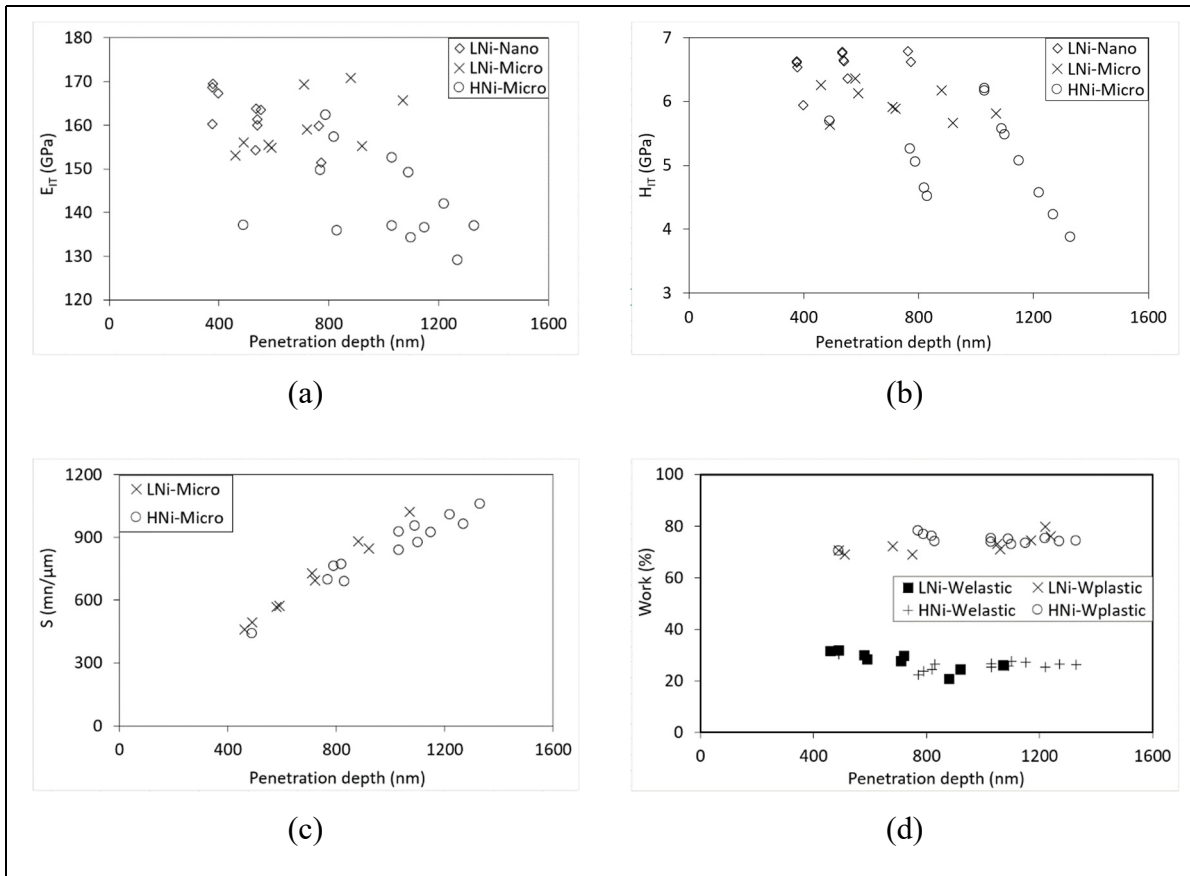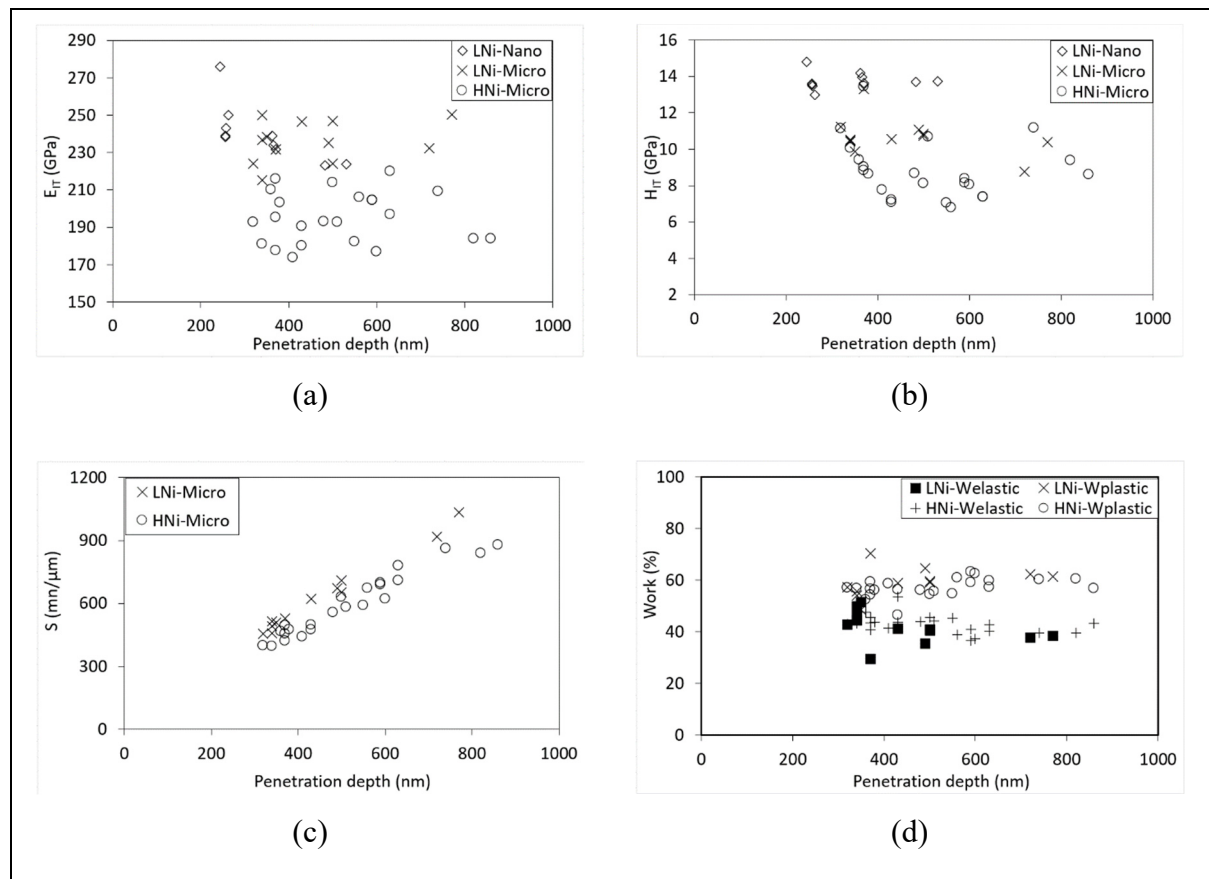
Figure 4.7 The indentation results on hematite layer: a) elastic modulus, b) hardness, c) stiffness, and d) conducted work.

The oxide-metal interface, known as the transition layer, is thicker for HNi steel compared to LNi. The thicker transition layer makes a better oxide-metal mechanical bonding, resisting for descaling of formed oxide on HNi steel. Micro-indentation on transition layer showed that the hardness was 5.1 and 4.7 GPa for LNi and HNi steel, where the thicker layer has a lower hardness. Immediately after the transition layer, the micro-indentation measures on the base metal indicated a hardness of 3.7 and 2.9 GPa for LNi and HNi, respectively. The low hardness level of the base metal in the zone adjacent to the oxide-metal interface, si due to the decarburization by diffusion of ions. The above results clearly reveal the differences in the mechanical properties of the different layers and therefore the need for the quantification of their effects on the interfacial friction between ingot and anvils during deformation.

4.4.2   Friction calibration curves (FCCs)

As illustrated in Fig. 4.8, both steels' stress-strain curves were obtained by compression tests at 1373 and 1473 K with 0.25 s^{-1}, and the effect of friction was corrected using the procedure described above. The corrected stress-strain curves were utilized for FE simulation of hot ring compression tests. The FCCs illustrated in Fig. 4.9 for LNi, and HNi steels were acquired at the above indicated temperatures by obtaining the variations of the inner diameter of rings by height reduction. The curves were acquired by both Coulomb and friction Constant shear friction models. The single points on the graphs show the results of the experimental tests for rings, with and without oxide layers.

The results show that both friction models came to the same predictions for a friction coefficient range from frictionless conditions to a friction coefficient of m=0.2. Afterward, the Coulomb model shows slightly higher values. However, the friction coefficient for conducted experiments never surpasses the coefficient of m=0.2. For all tested conditions, the highest friction was obtained for rings without oxidation, at m=0.2. At these temperatures, steel tends to stick to die surfaces and high frictional conditions are produced. The decrease in friction coefficient with the oxidation progress show that the oxide layers act as a lubricant at high temperatures.
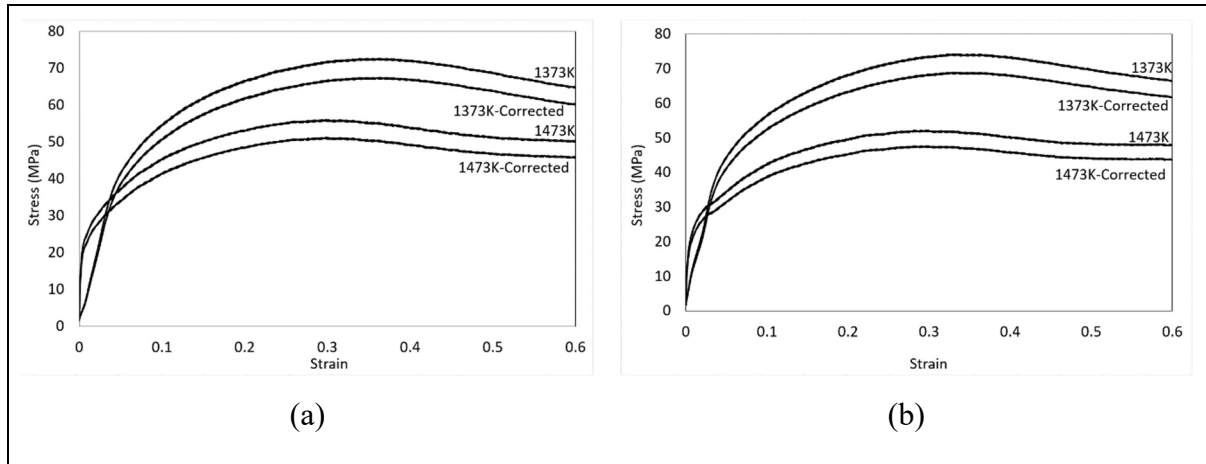
Figure 4.8 Stress-strain curves from hot compression tests, corrected for friction effects for a) LNi, and b) HNi.

For LNi, at deformation temperature of 1473 K, the friction decreased from m=0.2 for the ring without oxidation to m=0.14, 0.11, and 0.1 after oxidizing the ring for 10, 30, and 60 min, respectively. Therefore, as the oxide thickness increases, it can act more as a lubricant to decrease the ring and anvils' interfacial friction. For HNi steel, at the same deformation temperature, the friction decreased from m=0.2 to m=0.17, 0.14, and 0.12 for the 10, 30, and 60 min oxidation times, respectively. The friction decreased by oxidation for HNi steel, but at a lower level as compared to LNi steel. This issue is due to the lower thickness of the formed oxide on HNi steel than LNi steel, where the Ni modifies the oxidation. For LNi steel at deformation temperature of 1373 K, the friction coefficient was m=0.16, 0.14, and 0.12 by oxidation for 10, 30, and 60 min. For the same deformation temperature and oxidation times, friction coefficients of m=0.19, 0.15, and 0.13 were obtained for HNi steel. Temperature is a critical factor for the growth of thermally grown oxides. Hence, at a lower temperature, the oxide thickness was less, leading to a smaller decrease of friction by oxidation.
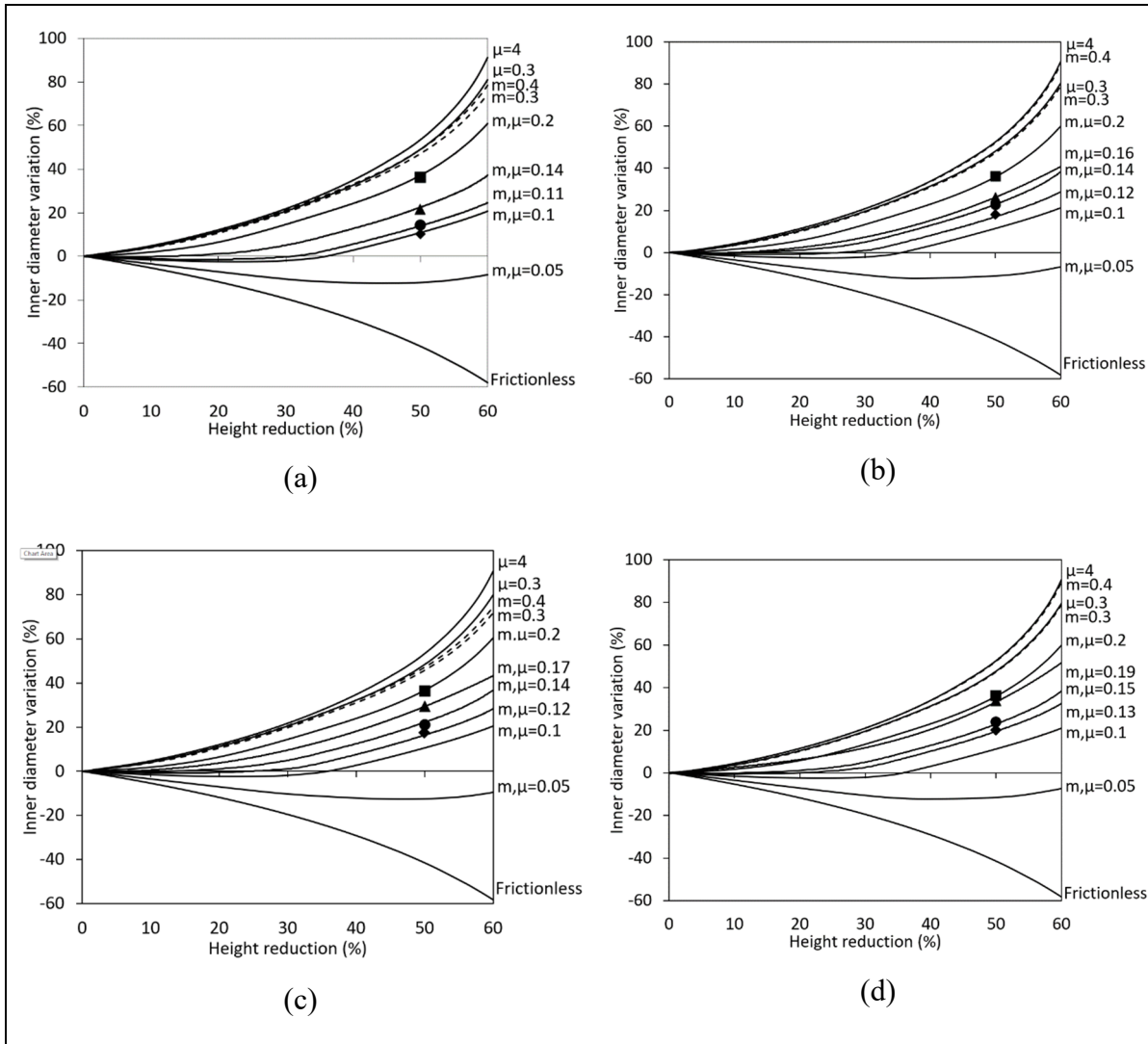
Figure 4.9 Acquired FCCs for: a) LNi at 1473 K, b) LNi at 1373 K,
c) HNi at 1473 K, and d) HNi at 1373 K.

Furthermore, the Young modulus and hardness of oxide layers formed on LNi steel were higher than the formed ones on HNi steel. This avoids the early disintegration of these layers as lubricants. Therefore, the oxide layers of LNi steel decreased friction in a greater degree compared to the HNi oxides. As a result of friction decrease by oxide layers, the forming loads decrease too. Fig. 4.10 illustrates the applied forming loads by the anvils to deform rings at 1473 K.
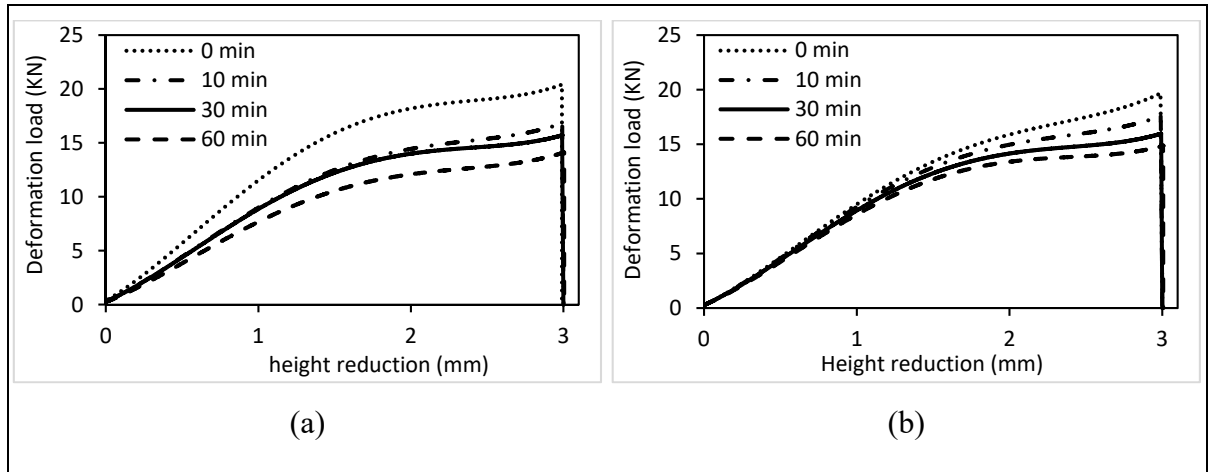
Figure 4.10 Deformation load required for deformation of rings by MT at 1473 K for:
a) LNi, and b) HNi.
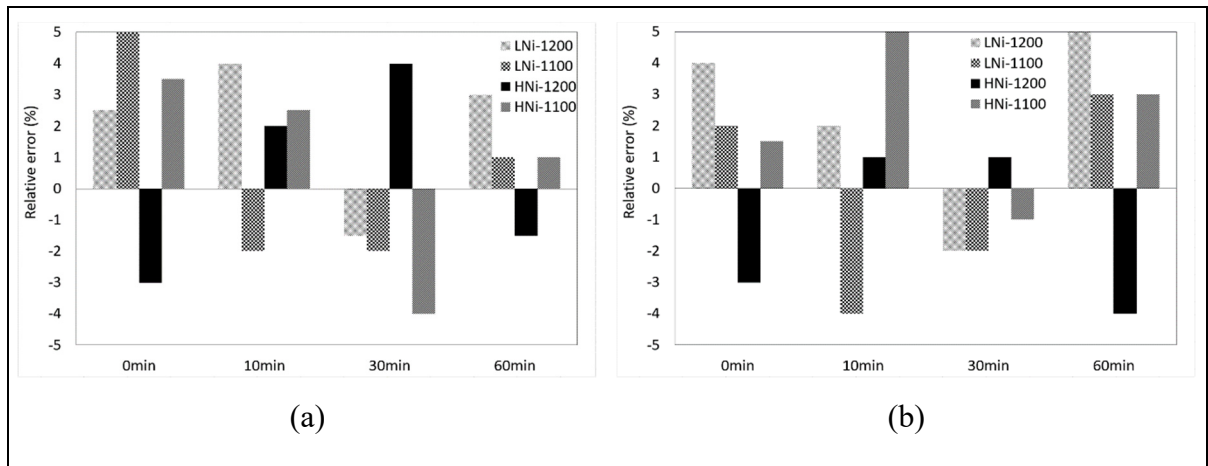
Figure 4.11 Relative error of the difference between FE and experimental tests for: a) outer
diameter and b) deformation load.

The required deformation loads for deformation of rings at 1473 K for both LNi and HNi steels
were decreased by oxidation. This is related to the fact that oxide layers act as lubricants at this
temperature. The loads for deformation of LNi steel decreased from 20412 N for without
oxidation condition to 16815, 15714, and 14121 N after oxidation for 10, 30, and 60 min. For
HNi steel, the deformation load decreased from 19677 N at its maximum to 17589, 15975, and
14874 N after oxidation for 10, 30, and 60 min. To validate the accuracy of the developed FE

model and FCCs, the outer diameters and deformation loads of both FE models and experimental tests were compared, and the relative errors were calculated. The obtained results are in a reasonable agreement, and the errors are given in Fig. 4.11.

4.5   Summary and conclusions

The mechanical characteristics of different oxide layers formed on two high-strength steels were evaluated by micro-indentation and nano-indentation methods. It was found that while the same layers of wustite, hematite, and magnetite were observed for both steels, their characteristics were different. The micro-indentation and nano-indentation results on thermally grown oxide layers on LNi steel were close and in a reasonable agreement. The Young modulus, hardness and stiffness of all oxide layers were higher for formed layers on LNi steel than HNi ones, whereas the elastic and plastic work ratios remained the same for two oxides. The Young modulus and hardness values of LNi oxide layers were consistently higher than those for the HNi oxide layers. Ring compression tests and FEM modeling were employed for the evaluation of interfacial friction using both Coulomb and constant shear friction models. The results clearly showed that the presence of the oxide layer acted as a lubricant at higher temperatures with the oxide layers on LNi steel decreasing the friction more than the formed oxides on HNi steels. This phenomenon was associated to the higher thickness of formed oxide layers on LNi steel and the higher mechanical properties of LNi oxides as compared to the HNi ones.

4.6   Declaration of Competing Interest

The authors declare that they have no competing interest that can influence the conducted study.

4.7   Acknowledgment

CONCLUSION

The main aim of this study was to investigate the thermally grown oxides on two high-strength steels and assess the effect of scale formation on heat transfer and interfacial friction during the open-die forging process. In this regard, the kinetics of oxide growth was acquired for two steels at high temperatures, and the effect of Ni was investigated on the formation of oxide layers. The heat transfer of the large-size ingots was evaluated by developing a finite element model using Abaqus CAE. The formation and growth of oxide layers were considered in this model, and the model was verified by experimental evaluation in a real industrial situation. The mechanical characteristics of each oxide layer were acquired employing indentation tests. The interfacial friction between die and ingot was then assessed by employing finite element simulations by Abaqus CAE, considering the oxide layers.

The following summarizes the obtained outcomes in the present thesis:

1) The oxidation kinetics of both steels increased with increasing the oxidation temperature and oxidation time. However, the oxidation of HNi steel was lower than LNi steel.

2) In addition to three general oxide layers of wustite, magnetite, and hematite, the spinel and chromite were detected. These layers and Ni-rich and Cr-rich bands hindered oxygen and Fe diffusion and consequently decreased HNi steel oxidation.

3) The thickness fraction of wustite increased by increasing the oxidation temperature, whereas the fraction of hematite decreased. The thickness fraction of magnetite stayed the same for all testing conditions.

4) Although the oxide thickness of HNi was lower compared to LNi, the thickness fraction of all the layers were the same for the formed scale on both steels.

5) The formation of the oxide layer up to a critical thickness can accelerate the cooling of a large-size ingot due to the higher radiation by vast surfaces of the ingot.

6) For the industrial case of oxide with a thickness of 7.8 mm, the insulation effect of oxide was effective, causing 200 K higher temperature for ingot with oxide than ingot without oxide.

7) The indentation test on different oxide layers showed that the formed oxide layer on HNi steel had lower hardness and young modulus than the formed scale on LNi steel.

8) The ring tests demonstrated that the oxide layers acted as additional lubricants at the higher temperature, decreasing the interfacial friction between die and ingot. Consequently, the deformation loads decrease.

RECOMMENDATIONS

1) As oxide formation is inevitable for the majority of steels during hot deformation, descaling is essential. The mechanical bonding and the interface between oxide and metal are different for steel's different chemical compositions. Thus, the adhesion of oxide layers can be assessed by employing micro tensile tests to evaluate the required descaling parameters.

2) Despite the detection of the same oxide layers for both steels of this study, the indentation results demonstrated different mechanical characteristics for formed scales. So, assessing the crystallography of formed scales on different steels can be meaningful to clarify the discrepancies between the two oxides.

3) The surface roughness of different oxide layers can be another important factor for heat transfer and interfacial friction of ingots. The Atomic force microscopy (AFM) can evaluate the oxide surface roughness in different oxidation conditions.

4) The caused wear by the formation of thermally grown oxides can be investigated for different frictional conditions. Different wear testing methods can be employed to assess the wear at high temperatures.

LIST OF BIBLIOGRAPHICAL REFERENCES

Abuluwefa, H., Guthrie, R., & Ajersch, F. (1996). The effect of oxygen concentration on the oxidation of low-carbon steel in the temperature range 1000 to 1250 C. *Oxidation of metals, 46*(5-6), 423-440.

Abuluwefa, H., Guthrie, R., & Ajersch, F. (1997). Oxidation of low carbon steel in multicomponent gases: Part I. Reaction mechanisms during isothermal oxidation. *Metallurgical and Materials Transactions A, 28*(8), 1633-1641.

Akiyama, T., Ohta, H., Takahashi, R., Waseda, Y., & Yagi, J.-i. (1992). Measurement and modeling of thermal conductivity for dense iron oxide and porous iron ore agglomerates in stepwise reduction. *ISIJ international, 32*(7), 829-837.

Altan, T., Ngaile, G., & Shen, G. (2005). *Cold and hot forging: fundamentals and applications* (Vol. 1). ASM international.

Amano, T., Okazaki, M., Takezawa, Y., Shiino, A., Takeda, M., Onishi, T., . . . Shishido, T. (2006). Hardness of oxide scales on Fe-Si alloys at room-and high-temperatures. Dans *Materials science forum* (Vol. 522, pp. 469-476). Trans Tech Publ.

Asai, T., Soshiroda, T., & Miyahara, M. (1997). Influence of Ni impurity in steel on the removability of primary scale in hydraulic descaling. *ISIJ international, 37*(3), 272-277.

Ashimabha, B., Parthasarathi, N. L., Arvinth, D., Utpal, B., & Jeevanantham, A. K. (2018). DETERMINATION OF FRICTIONAL COEFFICIENT OF 316L (N) STAINLESS STEEL BY RING COMPRESSION TEST USING SIMULATION. *Journal of Manufacturing Engineering, 13*(2), 113-117.

Avitzur, B. (1964). Forging of hollow discs. Dans *Israel Journal of Technology* (Vol. 2, pp. 295-&). WEIZMANN SCI PRESS ISRAEL 8A HORKANIA STREET PO BOX 801, JERUSALEM 91007, ISRAEL.

Bahadori, A. (2014). *Thermal insulation handbook for the oil, gas, and petrochemical industries*. Gulf Professional Publishing.

150

Bai, Q., Lin, J., Zhan, L., Dean, T., Balint, D., & Zhang, Z. (2012). An efficient closed-form method for determining interfacial heat transfer coefficient in metal forming. *International Journal of Machine Tools and Manufacture, 56*, 102-110.

Barrau, O., Boher, C., Gras, R., & Rezai-Aria, F. (2003). Analysis of the friction and wear behaviour of hot work tool steel for forging. *Wear, 255*(7-12), 1444-1454.

Barrau, O., Boher, C., Vergne, C., Rezai-Aria, F., & Gras, R. (2002). Investigations of friction and wear mechanisms of hot forging tool steels. *Karlstad University, 1*, 81-94.

Basabe, V. V., & Szpunar, J. A. (2006). Phase composition of oxide scales during reheating in hot rolling of low carbon steel. *steel research international, 77*(11), 818-824.

Baud, J., Ferrier, A., & Manenc, J. (1978). Study of magnetite film formation at metal-scale interface during cooling of steel products. *Oxidation of metals, 12*(4), 331-342.

Beddoes, J., & Bibby, M. (1999). *Principles of metal manufacturing processes*. Butterworth-Heinemann.

Behrens, B.-A., Chugreev, A., Awiszus, B., Graf, M., Kawalla, R., Ullmann, M., . . . Wester, H. (2018). Sensitivity analysis of oxide scale influence on general carbon steels during hot forging. *Metals, 8*(2), 140.

Bejan, A., & Kraus, A. D. (2003). *Heat transfer handbook* (Vol. 1). John Wiley & Sons.

Bergman, T. L., Incropera, F. P., DeWitt, D. P., & Lavine, A. S. (2011). *Fundamentals of heat and mass transfer*. John Wiley & Sons.

Bhadeshia, H., & Honeycombe, R. (2017). *Steels: microstructure and properties*. Butterworth-Heinemann.

Bhushan, B. (2000). *Modern tribology handbook, two volume set*. CRC press.

Birks, N., Meier, G. H., & Pettit, F. S. (2006). *Introduction to the high temperature oxidation of metals*. Cambridge University Press.

Birosca, S., West, G., & Higginson, R. (2005). Microstructural investigation of the oxide scale on low carbon steel. *Metal, 24*(26.5), 2005.

Boggs, W., & Kachik, R. (1969). The Oxidation of Iron-Carbon Alloys at 500° C. *Journal of the Electrochemical Society, 116*(4), 424.

Bradley, S. A., Barr, T. L., & Youtsey, K. J. J. J. o. M. S. (1979). Examination of the high-temperature (850° C) oxidation of an Ni-Si-B powder. *14*(10), 2317-2324.

Brandes, E., Brook, G., & Paufler, P. (1993). Smithells Metals Reference Book. Butterworth-Heinemann Ltd., Oxford, 1992. 1746 Seiten, Preis 150£, ISBN 0-7506-1020-4. *Crystal Research and Technology, 28*(4), 530-530.

Buffington, F., Hirano, K.-i., & Cohen, M. (1961). Self diffusion in iron. *Acta Metallurgica, 9*(5), 434-439.

Burgess, G. K., & Foote, P. D. (1916). *The Emissivity of Metals and Oxides: Iron oxide* (Vol. 12). US Department of Commerce, Bureau of Standards.

Cao, G.-m., Liu, X.-j., Sun, B., & Liu, Z.-y. (2014). Morphology of oxide scale and oxidation kinetics of low carbon steel. *Journal of Iron and Steel Research International, 21*(3), 335-341.

Caplan, D., Sproule, G., Hussey, R., & Graham, M. (1979). Oxidation of Fe-C alloys at 700° C. *Oxidation of metals, 13*(3), 255-272.

Chalkley, E. (2020). A Multivariate Emissivity Dataset to Facilitate Infrared Thermometry of High Temperature Materials. *Sensors & Transducers, 241*(2), 1-6.

Chang, Y., Li, S., Li, X., Wang, C., Hu, P., & Zhao, K. (2016). Effect of contact pressure on IHTC and the formability of hot-formed 22MnB5 automotive parts. *Applied Thermal Engineering, 99*, 419-428.

Chang, Y., Tang, X., Zhao, K., Hu, P., & Wu, Y. (2016). Investigation of the factors influencing the interfacial heat transfer coefficient in hot stamping. *Journal of Materials Processing Technology, 228*, 25-33.

Chang, Y. N., & Wei, F. I. (1989). High temperature oxidation of low alloy steels. *Journal of Materials Science, 24*(1), 14-22.

Chen, L., Zhou, Z., Tan, Z., He, D., Bobzin, K., Zhao, L., . . . Königstein, T. (2018). High temperature oxidation behavior of Al 0.6 CrFeCoNi and Al 0.6 CrFeCoNiSi 0.3 high entropy alloys. *Journal of Alloys and Compounds*.

Chen, R., & Yeun, W. (2003). Review of the high-temperature oxidation of iron and carbon steels in air or oxygen. *Oxidation of metals, 59*(5-6), 433-468.

Chen, R., & Yuen, W. (2000). A study of the scale structure of hot-rolled steel strip by simulated coiling and cooling. *Oxidation of metals, 53*(5-6), 539-560.

Chen, R., & Yuen, W. (2005a). Examination of oxide scales of hot rolled steel products. *ISIJ international, 45*(1), 52-59.

Chen, R., & Yuen, W. (2005b). Isothermal and Step Isothermal Oxidation of Copper-Containing Steels in Air at 980–1220° C. *Oxidation of metals, 63*(3-4), 145-168.

Chen, R. Y., & Yuen, W. (2008). Short-time Oxidation Behavior of Low-carbon, Low-silicon Steel in Air at 850–1,180° C—I: Oxidation Kinetics. *Oxidation of metals, 70*(1-2), 39-68.

Chen, R. Y., & Yuen, W. (2009). Oxidation of Low-Carbon Steel in 17H 2 ON 2 at 900° C. *Metallurgical and Materials Transactions A, 40*(13), 3091.

Cheng, X., Jiang, Z., Wei, D., Zhao, J., Monaghan, B. J., Longbottom, R. J., & Jiang, L. (2015). High temperature oxidation behaviour of ferritic stainless steel SUS 430 in humid air. *Metals and Materials International, 21*(2), 251-259.

Chicot, D., Mendoza, J., Zaoui, A., Louis, G., Lepingle, V., Roudet, F., & Lesage, J. (2011). Mechanical properties of magnetite (Fe_3O_4), hematite (α-Fe_2O_3) and goethite (α-FeO· OH) by instrumented indentation and molecular dynamics analysis. *Materials Chemistry and Physics, 129*(3), 862-870.

Committee, A. I. H. (1991). *ASM handbook: Heat treating* (Vol. 4). Asm Intl.

Ding, H., & Shin, Y. C. (2013). Improvement of machinability of Waspaloy via laser-assisted machining. *The International Journal of Advanced Manufacturing Technology, 64*(1-4), 475-486.

Dixit, P. M., & Dixit, U. S. (2008). *Modeling of metal forming and machining processes: by finite element and soft computing methods*. Springer Science & Business Media.

Doerner, M. F., & Nix, W. D. (1986). A method for interpreting the data from depth-sensing indentation instruments. *Journal of Materials research, 1*(4), 601-609.

Dong, X. x., He, A. r., Sun, W. q., Liu, Z. b., & Hong, B. (2017). Research on a 3D Temperature Field Model of a Slab with Oxide Layer Growth. *Heat Transfer—Asian Research, 46*(2), 147-159.

Dubey, S. K., Agarwal, N., & Srinivasan, P. (2012). Three dimensional transient heat transfer model for steel billet heating in reheat furnace. Dans *Heat Transfer Summer Conference* (Vol. 44786, pp. 963-967). American Society of Mechanical Engineers.

Dubey, S. K., & Srinivasan, P. (2013). Three dimensional transient explicit finite difference heat transfer modeling of billet transport. *Int. J. of Thermal & Environmental Engineering, 6*(2), 95-100.

Faghri, A., Zhang, Y., & Howell, J. R. (2010). *Advanced heat and mass transfer*. Global Digital Press.

Falk-Windisch, H., Svensson, J. E., & Froitzheim, J. (2015). The effect of temperature on chromium vaporization and oxide scale growth on interconnect steels for Solid Oxide Fuel Cells. *Journal of Power Sources, 287*, 25-35.

Fischer-Cripps, A. C. (2011). Applications of nanoindentation. Dans *Nanoindentation* (pp. 213-233). Springer.

Garruchet, S., Politano, O., Arnoux, P., & Vignal, V. (2010). Diffusion of oxygen in nickel: A variable charge molecular dynamics study. *Solid State Communications, 150*(9-10), 439-442.

Ghiotti, A., Fanini, S., Bruschi, S., & Bariani, P. (2009). Modelling of the Mannesmann effect. *CIRP annals, 58*(1), 255-258.

Graf, M., Ullmann, M., Korpala, G., Wester, H., Awiszus, B., Kawalla, R., & Behrens, B.-A. (2018). Forming and oxidation behavior during forging with consideration of carbon content of steel. *Metals, 8*(12), 996.

Hardell, J., Hernandez, S., Mozgovoy, S., Pelcastre, L., Courbon, C., & Prakash, B. (2015). Effect of oxide layers and near surface transformations on friction and wear during tool steel and boron steel interaction at high temperatures. *Wear, 330*, 223-229.

Heuer, C. F. (1969). *Diffusion of iron and cobalt in nickel single crystals* (Doctoral Dissertation, Missouri University of Science and Technology).

Higginson, R., Jepson, M., & West, G. (2006). Use of EBSD to characterise high temperature oxides formed on low alloy and stainless steels. *Materials science and technology, 22*(11), 1325-1332.

Holman, J. (2002). Heat transfer. *McGrawHill, New York, USA*.

Howell, J. R., Menguc, M. P., & Siegel, R. (2010). *Thermal radiation heat transfer*. CRC press.

Hu, X.-j., Zhang, B.-m., Chen, S.-h., Fang, F., & Jiang, J.-q. (2013). Oxide scale growth on high carbon steel at high temperatures. *Journal of Iron and Steel Research International, 20*(1), 47-52.

Hutchings, I., & Shipway, P. (2017). *Tribology: friction and wear of engineering materials*. Butterworth-Heinemann.

Jaklič, A., Glogovac, B., Kolenko, T., Zupančič, B., & Težak, B. (2002). A simulation of heat transfer during billet transport. *Applied Thermal Engineering, 22*(7), 873-883.

Jang, J. H., Lee, D. E., Kim, M. Y., & Kim, H. G. (2010). Investigation of the slab heating characteristics in a reheating furnace with the formation and growth of scale on the slab surface. *International Journal of Heat and Mass Transfer, 53*(19-20), 4326-4332.

Jha, R., Haworth, C. W., & Argent, B. B. (2001). The formation of diffusion coatings on some low-alloy steels and their high temperature oxidation behaviour: Part 2. Oxidation studies. *Calphad, 25*(4), 667-689.

Kao, C., & Wan, C. (1988). Effect of temperature on the oxidation of Fe-7.5 A1-o. 65C alloy. *Journal of Materials Science, 23*(6), 1943-1947.

Kieruj, P., Przestacki, D., & Chwalczuk, T. (2016). Determination of emissivity coefficient of heat-resistant super alloys and cemented carbide. *Archives of Mechanical Technology and Materials, 36*(1), 30-34.

Kim, I., Cho, W., & Kim, H. (2000). High-temperature oxidation of Fe3Al containing yttrium. *Journal of Materials Science, 35*(18), 4695-4703.

Kim, M. (2013). Effect of scale on slab heat transfer in a walking beam type reheating furnace. *International Journal of Mechanical, Aerospace, Industrial and Mechatronics Engineering, 7*(7), 410-414.

Kobayashi, S., Kobayashi, S., Oh, S.-I., & Altan, T. (1989). *Metal forming and the finite-element method* (Vol. 4). Oxford University Press on Demand.

Krzyzanowski, M., & Beynon, J. H. (2006). Modelling the behaviour of oxide scale in hot rolling. *ISIJ international, 46*(11), 1533-1547.

Krzyzanowski, M., Beynon, J. H., & Farrugia, D. C. (2010). *Oxide scale behavior in high temperature metal processing*. John Wiley & Sons.

Kumari, S. V., Vaidyan, V., & Sathyanarayana, K. J. J. o. m. s. (1991). Surface oxidation of ferrochromium thin films. *26*(7), 1899-1902.

Laukka, A., Heikkinen, E. P., & Fabritius, T. (2019). In-Depth Oxide Scale Growth Analysis of B and Ti Microalloyed AISI 304 in Oxygen-Containing Furnace Atmospheres and CH4 Burn-Simulating Furnace Atmospheres. *steel research international, 90*(1), 1800447.

Lawrence, S. K., Adams, D. P., Bahr, D. F., & Moody, N. R. (2013). Mechanical and electromechanical behavior of oxide coatings grown on stainless steel 304L by nanosecond pulsed laser irradiation. *Surface and Coatings Technology, 235*, 860-866.

Li, M., Endo, R., Akoshima, M., Tanei, H., Okada, H., & Susa, M. (2019). Thermal Conductivity of Oxide Scale Thermally Grown on Iron Substrate Corrected by Temperature-dependent Interfacial Thermal Resistance in Laser Flash Measurement. *ISIJ international, 59*(3), 398-403.

Li, Y., Onodera, E., Matsumoto, H., & Chiba, A. (2009). Correcting the stress-strain curve in hot compression process to high strain level. *Metallurgical and Materials Transactions A, 40*(4), 982-990.

Li, Z. F., Cao, G. M., He, Y. Q., Liu, Z. Y., & Wang, G. D. (2016). Effect of chromium and water vapor of low carbon steel on oxidation behavior at 1050° C. *steel research international, 87*(11), 1469-1477.

Liu, S., Tang, D., Wu, H., & Wang, L. (2013). Oxide scales characterization of micro-alloyed steel at high temperature. *Journal of Materials Processing Technology, 213*(7), 1068-1075.

Luong, L., & Heijkoop, T. (1981). The influence of scale on friction in hot metal working. *Wear, 71*(1), 93-102.

Madern, N., Monnier, J., Baddour-Hadjean, R., Steckmeyer, A., & Joubert, J.-M. (2018). Characterization of refractory steel oxidation at high temperature. *Corrosion Science, 132*, 223-233.

Matsumoto, R., Harada, S., & Utsunomiya, H. (2014). Friction in hot forging of chrome steel covered with oxide scale film generated at steam atmosphere. Dans *Key Engineering Materials* (Vol. 622, pp. 194-200). Trans Tech Publ.

Matsumoto, R., Osumi, Y., & Utsunomiya, H. (2014). Reduction of friction of steel covered with oxide scale in hot forging. *Journal of Materials Processing Technology, 214*(3), 651-659.

Mehrer, H. (2007). *Diffusion in solids: fundamentals, methods, materials, diffusion-controlled processes* (Vol. 155). Springer Science & Business Media.

Morgado, T., Coelho, P. J., & Talukdar, P. (2015). Assessment of uniform temperature assumption in zoning on the numerical simulation of a walking beam reheating furnace. *Applied Thermal Engineering, 76*, 496-508.

Mouayd, A. A., Koltsov, A., Sutter, E., & Tribollet, B. (2014). Effect of silicon content in steel and oxidation temperature on scale growth and morphology. *Materials Chemistry and Physics, 143*(3), 996-1004.

Mrowec, S., & Grzesik, Z. (2004). Oxidation of nickel and transport properties of nickel oxide. *Journal of Physics and Chemistry of Solids, 65*(10), 1651-1657.

Munther, P. A., & Lenard, J. G. (1999). The effect of scaling on interfacial friction in hot rolling of steels. *Journal of Materials Processing Technology, 88*(1-3), 105-113.

Nagl, M., & Evans, W. (1993). The mechanical failure of oxide scales under tensile or compressive load. *Journal of Materials Science, 28*(23), 6247-6260.

Nalwa, H. S. (2001). *Handbook of surfaces and interfaces of materials, five-volume set.* Elsevier.

Nam, H. O., Yoon, J. Y., Kim, J. H., Hwang, I. S., & Lee, K. H. (2011). Evaluation of the Oxygen Diffusion Coefficient in Nickel-Base Alloys. Dans *Proceedings of the 15th International Conference on Environmental Degradation of Materials in Nuclear Power Systems—Water Reactors* (pp. 1463-1475). Springer.

Nee, A. Y. (2015). *Handbook of manufacturing engineering and technology.* Springer.

Nowak, W. J. (2018). Effect of surface roughness on early stage oxidation behavior of ni-base superalloy IN 625. *Applied System Innovation, 1*(3), 32.

Nowak, W. J. (2020). Effect of Surface Roughness on Oxidation Resistance of Stainless Steel AISI 316Ti During Exposure at High Temperature. *Journal of Materials Engineering and Performance, 29*(12), 8060-8069.

Odabas, D. (2018). The influence of the temperature on dry friction of AISI 3315 steel sliding against AISI 3150 steel. Dans *IOP Conference Series: Materials Science and Engineering* (Vol. 295, pp. 012021). IOP Publishing.

Oliver, W. C., & Pharr, G. M. (1992). An improved technique for determining hardness and elastic modulus using load and displacement sensing indentation experiments. *Journal of Materials research, 7*(6), 1564-1583.

Oliver, W. C., & Pharr, G. M. (2004). Measurement of hardness and elastic modulus by instrumented indentation: Advances in understanding and refinements to methodology. *Journal of Materials research, 19*(1), 3-20.

Oyachi, Y., Utsunomiya, H., Sakai, T., Yoshikawa, T., & Tanaka, T. (2012). Effects of porous surface layer on lubrication evaluated by ring compression friction test. *ISIJ international, 52*(5), 858-862.

Pihtili, H. (2013). *Tribology in Engineering.* BoD–Books on Demand.

158

Pujilaksono, B., Jonsson, T., Halvarsson, M., Svensson, J.-E., & Johansson, L.-G. (2010). Oxidation of iron at 400–600 C in dry and wet O2. *Corrosion Science, 52*(5), 1560-1569.

Rahmel, A., Schütze, M., & Quadakkers, W. (1995). Fundamentals of TiAl oxidation–a critical review. *Materials and Corrosion, 46*(5), 271-285.

Rajesh, E., & SivaPrakash, M. (2013). Analysis of friction factor by employing the ring compression test under different lubricants. *International Journal of Scientific & Engineering Research, 4*(5), 1163-1170.

Saeki, I., Ohno, T., Sakai, O., Niya, T., & Sato, T. (2011). In situ measurement of Young's modulus of FeO scale formed on pure iron at 973–1273 K by acoustic resonance method. *Corrosion Science, 53*(1), 458-463.

Saunders, N., Guo, U., Li, X., Miodownik, A., & Schillé, J.-P. (2003). Using JMatPro to model materials properties and behavior. *Jom, 55*(12), 60-65.

Seo, M., & Chiba, M. (2001). Nano-mechano-electrochemistry of passive metal surfaces. *Electrochimica acta, 47*(1-2), 319-325.

Shahriari, D., Sadeghi, M., Ebrahimi, G., & Kim, K. (2011). Effects of lubricant and temperature on friction coefficient during hot forging of Nimonic 115 superalloy. *Kovove Mater, 49*(5), 375-383.

Sharpe, W. N. (2008). *Springer handbook of experimental solid mechanics*. Springer Science & Business Media.

Slater, J. C. (1964). Atomic radii in crystals. *The Journal of Chemical Physics, 41*(10), 3199-3204.

Sofuoglu, H., Gedikli, H., & Rasty, J. (2001). Determination of friction coefficient by employing the ring compression test. *J. Eng. Mater. Technol., 123*(3), 338-348.

Spuzic, S., Strafford, K., Subramanian, C., & Savage, G. (1994). Wear of hot rolling mill rolls: an overview. *Wear, 176*(2), 261-272.

Suarez, L., Houbaert, Y., Eynde, X. V., & Colás, R. (2009). High temperature deformation of oxide scale. *Corrosion science, 51*(2), 309-315.

Suárez, L., Houbaert, Y., Eynde, X. V., & Colás, R. (2008). Development of an experimental device to study high temperature oxidation. *Oxidation of metals, 70*(1-2), 1-13.

Suárez, L., Rodríguez-Calvillo, P., Houbaert, Y., & Colás, R. (2010). Oxidation of ultra low carbon and silicon bearing steels. *Corrosion science, 52*(6), 2044-2049.

Takada, J., & Adachi, M. (1986). Determination of diffusion coefficient of oxygen in α-iron from internal oxidation measurements in Fe-Si alloys. *Journal of Materials Science, 21*(6), 2133-2137.

Takeda, M., Kushida, H., Onishi, T., Toyama, M., Koizumi, F., & Fujimoto, S. (2010). Influence of oxidation temperature and Cr content on the adhesion and microstructure of scale on low Cr steels. *Oxidation of metals, 73*(1-2), 1-13.

Takeda, M., Onishi, T., Nakakubo, S., & Fujimoto, S. (2009). Physical properties of iron-oxide scales on Si-containing steels at high temperature. *Materials transactions, 50*(9), 2242-2246.

Talbot, D. E., & Talbot, J. D. (2018). *Corrosion science and technology*. CRC press.

Tawancy, H. (1996). High-temperature oxidation behavior of a wrought Ni-Cr-W-Mn-Si-La alloy. *Oxidation of metals, 45*(3-4), 323-348.

Torres, M. n., & Colás, R. (2000). A model for heat conduction through the oxide layer of steel during hot rolling. *Journal of Materials Processing Technology, 105*(3), 258-263.

Totten, G. E. (2006). *Steel Heat Treatment Handbook-2 Volume Set*. CRC press.

Tsao, T.-K., Yeh, A.-C., Kuo, C.-M., & Murakami, H. (2016). High temperature oxidation and corrosion properties of high entropy superalloys. *Entropy, 18*(2), 62.

Utsunomiya, H., Doi, S., Hara, K.-i., Sakai, T., & Yanagi, S. (2009). Deformation of oxide scale on steel surface during hot rolling. *CIRP annals, 58*(1), 271-274.

Vedaei-Sabegh, A., Morin, J.-B., & Jahazi, M. (2020). Influence of Nickel on High-Temperature Oxidation and Characteristics of Oxide Layers in Two High-Strength Steels. *steel research international, 91*(4), 1900536.

Vergne, C., Boher, C., Gras, R., & Levaillant, C. (2006). Influence of oxides on friction in hot rolling: Experimental investigations and tribological modelling. *Wear, 260*(9-10), 957-975.

Vijh, A. (1974). Relationship between activation energies for the thermal oxidation of metals and the semiconductivity of the oxides. *Journal of Materials Science, 9*(6), 985-988.

Von Fraunhofer, J., & Pickup, G. (1970). The oxidation behaviour of low alloy steels—Part1. *Anti-Corrosion Methods and Materials, 17*(4), 10-19.

Wakasa, K., & Yamaki, M. (1988). High-temperature oxidation behaviour of base metal elements in nickel-base alloys. *Journal of Materials Science, 23*(4), 1459-1463.

Wang, C., & Duh, J. (1988). The effect of carbon on the high temperature oxidation of Fe-31 Mn-9Al-0.87 C alloy. *Journal of Materials Science, 23*(10), 3447-3454.

Wang, X., Wang, C., & Li, J. (2018). Simulation analysis of temperature field of dynamic slabs oxidized in walking-beam reheating furnaces. Dans *2018 Chinese Automation Congress (CAC)* (pp. 2050-2053). IEEE.

Webler, B., Yin, L., & Sridhar, S. (2008). Effects of small additions of copper and copper+ nickel on the oxidation behavior of iron. *Metallurgical and Materials Transactions B, 39*(5), 725.

Webler, B. A., & Sridhar, S. (2007). The effect of silicon on the high temperature oxidation behavior of low-carbon steels containing the residual elements copper and nickel. *ISIJ international, 47*(9), 1245-1254.

Yin, H., Chan, S., Yuen, W., & Young, D. (2012). Temperature Effects on the Oxidation of Low Carbon Steel in N 2–H 2–H 2 O at 800–1200° C. *Oxidation of metals, 77*(5-6), 305-323.

Yin, L., Balaji, S., & Sridhar, S. (2010). Effects of Nickel on the Oxide/Metal Interface Morphology and Oxidation Rate During High-Temperature Oxidation of Fe–Cu–Ni Alloys. *Metallurgical and Materials Transactions B, 41*(3), 598-611.

Young, D. J. (2008). *High temperature oxidation and corrosion of metals* (Vol. 1). Elsevier.

Yu, X., Jiang, Z., Zhao, J., Wei, D., Zhou, J., Zhou, C., & Huang, Q. (2015). Local strain analysis of the tertiary oxide scale formed on a hot-rolled steel strip via EBSD. *Surface and Coatings Technology, 277*, 151-159.

Yuan, J., Wang, W., Zhu, S., & Wang, F. (2013). Comparison between the oxidation of iron in oxygen and in steam at 650–750 C. *Corrosion Science, 75*, 309-317.

Yuan, J., Wu, X., Wang, W., Zhu, S., & Wang, F. (2013). The effect of surface finish on the scaling behavior of stainless steel in steam and supercritical water. *Oxidation of metals, 79*(5-6), 541-551.

Yun, J. Y., Ha, S. A., Kang, C. Y., & Wang, J. P. (2013). Oxidation behavior of low carbon steel at elevated temperature in oxygen and water vapor. *steel research international, 84*(12), 1252-1257.

Zambrano, O., Coronado, J., & Rodríguez, S. (2015). Mechanical properties and phases determination of low carbon steel oxide scales formed at 1200 C in air. *Surface and Coatings Technology, 282*, 155-162.

Zamri, W., Kosasih, P., Tieu, A., Zhu, Q., & Zhu, H. (2012). Variations in the microstructure and mechanical properties of the oxide layer on high speed steel hot rolling work rolls. *Journal of Materials Processing Technology, 212*(12), 2597-2608.

Zareh-Desari, B., & Davoodi, B. (2016). Assessing the lubrication performance of vegetable oil-based nano-lubricants for environmentally conscious metal forming processes. *Journal of Cleaner Production, 135*, 1198-1209.

Zhu, Y., Zeng, W., Ma, X., Tai, Q., Li, Z., & Li, X. (2011). Determination of the friction factor of Ti-6Al-4V titanium alloy in hot forging by means of ring-compression test using FEM. *Tribology International, 44*(12), 2074-2080.